UNIVERSITY OF
KWAZULU-NATAL

INYUVESI
YAKWAZULU-NATALI

GENERATION AND DETECTION OF BESSEL BEAMS

Thandeka Mhlanga

A dissertation submitted in fulfilment of the academic requirements for the degree of Master of Science in the School of Physics, University of KwaZulu-Natal, Durban.

Supervisor:

Prof. Andrew Forbes

and

Co-Supervisor:

Prof. Thomas Konrad

March 1, 2015

To my mother

Abstract

In this dissertation we study the properties of Bessel-Gauss beams. Bessel-Gauss beams are created by the interference of plane waves lying on a cone, and have unique properties: they propagate without spreading and recover their phase and amplitude upon encountering an obstruction. These modes have found application in the manipulation of micro-particles, atomic dipole traps, and atomic guiding. As high-order Bessel-Gauss beams carry orbital angular momentum, they have been used as a basis for information encoding in both the classical and quantum regimes. We show how to generate these modes using axicons, and spiral ring-slits, which we implement digitally on a spatial light modulator. Using an all digital experimental setup we extract the information encoded in these modes in two dimensions, where we simultaneously detect the radial and azimuthal components of these beams. This detection tool is shown to be useful in studying Bessel-Gauss modes that have propagated through optical turbulence and that have been obstructed. Vector Bessel-Gauss beams are then generated and detected using a q-plate and polarized grating, respectively. We then apply the reconstruction property of the Bessel-Gauss modes in a quantum experimental setup, where we show that we can recover quantum entanglement after encountering an obstruction. We show that the digital spiral ring-slit can be used at the single photon level as a single pixel detector, to recover the phase and amplitude on an object in a ghost imaging setup.

Declarations 1

The work described by this thesis was carried out at Council for Scientific and Industrial Research, National Laser Centre, while registered with the School of Physics, University of KwaZulu-Natal, Durban, Westville, from **April 2013** until **April 2015**, under the supervision of **Prof. Andrew Forbes** and co-supervisor **Prof. Thomas Konrad**.

This thesis is entirely, unless specifically contradicted in the text, the work of the candidate, **Thandeka Mhlanga**, and has not been previously submitted, in whole or in part, to any other tertiary institution. Where use has been made of the work of others, it is duly acknowledged in the text.

Signed: _____ Name: _____

Date: _____

As the candidate's supervisor I have/have not approved this thesis/dissertation for submission.

Signed: _____ Name: _____

Date: _____

Declaration 2 - Plagiarism

I, _____ declare that

1. The research reported in this thesis, except where otherwise indicated, is my original research.
2. This thesis has not been submitted for any degree or examination at any other university.
3. This thesis does not contain other persons' data, pictures, graphs or other information, unless specifically acknowledged as being sourced from other persons.
4. This thesis does not contain other persons' writing, unless specifically acknowledged as being sourced from other researchers. Where other written sources have been quoted, then:
    a. Their words have been rewritten but the general information attributed to them has been referenced.
    b. Where their exact words have been used, then their writing has been placed in italics and inside quotation marks, and referenced.
5. This thesis does not contain, text, graphics or tables copied and pasted from the Internet, unless specifically acknowledged, and the source being detailed in the thesis and in the References sections.

Signed: _____

Declaration 3 - Publications

Peer-Reviewed Journal Papers:

1. Dudley, A., **Mhlanga, T.**, Lavery, M., McDonald, A., Roux, F. S., Padgett, M., and Forbes, A.,"Efficient sorting of Bessel beams," Optics Express, **21**(1), 165-171 (2013).

2. Dudley, A., Li, Y., **Mhlanga, T.**, Escuti, M., and Forbes, A.,"Generating and measuring non-diffracting vector Bessel beams," Optics Letters, **38**(17), 3429-3432 (2013)

3. Trichili, A., **Mhlanga, T.**, Ismail, Y., Roux, F., McLaren, M., Zghal, M., and Forbes, A., "Detection of Bessel beams with digital axicons," Optics Express, **22**(14), 17553-17560 (2014).

4. McLaren, M., **Mhlanga, T.**, Padgett, M. J., Roux, F. S., and Forbes, A., "Self-healing of quantum entanglement after an obstruction," Nature Communications, **5**(3248), (2014).

   International Conference Papers:

5. **Mhlanga, T.**, McLaren, M., Abrahim, A., Konrad, T., and Forbes, A., "Digital bi-photon spiral imaging," Proc. SPIE, 91940A (2014).

6. **Mhlanga, T.**, Trichilli, A., Dudley, A., Naidoo, D., Zghal, M., and Forbes, A., "Digital holograms for laser mode multiplexing," Proc. SPIE, 91941B (2014).

Signed: _____

Contents

List of Figures

Acknowledgements

I would like to express my appreciation to all the people that have supported me throughout my MSc study, but mostly I would like to thank the following people:
My supervisor Prof. Andrew Forbes, for granting me the opportunity to do my MSc research under his supervision, for all the national and international trips I have enjoyed as part of my MSc package. For all the harsh criticism of my work that has taught me to reason, always do my best and to toughen up.
To the 'members' Angela (aka Nomsa), Mel (aka Naledi) and Darryl (aka Jabulani) thanks for patiently helping me in the laboratory, it has been amazing to have found senior members to help me through my studies. Miss B, thanks for all the 'special meetings' we had in your office, you have been a great listener.
To Thuli and Fman thanks for the lunches we had together and the great stories we have shared with each other. To the CSIR NLC thank you for the financial support and for providing me with the research facilities. To my Tunisian collaborator Trich, thanks for all the fun times at the lab. To my family and friends, thank you for the love and support that you have always shown me. For being patient with me and understanding at all times. To my grand mother, you the best. To Leonard, thank you for your encouragement, and for being a positive influence in my life, you are appreciated.

Chapter 1

Modes in free-space

1.1 Helmholtz scalar equation

The Helmholtz equation [1] is a time-independent partial differential equation that describes the propagation of waves in free-space, and it is derived from Maxwell's wave equation [2] in a vacuum through the method of separation of variables. Maxwell expressed the divergence and the curl of the electromagnetic wave in a vacuum as follows:

$$\vec{\nabla}.\vec{E} = 0, \tag{1.1}$$

$$\vec{\nabla}.\vec{B} = 0, \tag{1.2}$$

$$\vec{\nabla} \times \vec{E} = -\frac{\partial \vec{B}}{\partial t}, \tag{1.3}$$

$$\vec{\nabla} \times \vec{B} = \varepsilon_0 \mu_0 \frac{\partial \vec{E}}{\partial t}, \tag{1.4}$$

where ε_0 and μ_0 are the permittivity and permeability of free-space, $\vec{E}$ and $\vec{B}$ are the electric and magnetic fields, t is time. The speed of light is related to these parameters by

$$c = \frac{1}{\sqrt{\varepsilon_0 \mu_0}}. \tag{1.5}$$

To obtain the wave equation in free-space, we expand the curl of the electric field in Eq. 1.3, using the vector identity $\vec{\nabla} \times (\vec{\nabla} \times \vec{E}) = \vec{\nabla}(\vec{\nabla}.\vec{E} - \nabla^2\vec{E})$, resulting in:

$$\begin{aligned}
\vec{\nabla} \times \vec{E} &= \frac{\partial(\vec{\nabla} \times \vec{B})}{\partial t} \\
\Rightarrow \vec{\nabla}(\vec{\nabla}.\vec{E}) - \nabla^2\vec{E} &= -\frac{\partial(\vec{\nabla} \times \vec{B})}{\partial t} \\
\Rightarrow 0 - \nabla^2\vec{E} &= -\frac{\partial}{\partial t}(\varepsilon_0\mu_0\frac{\partial\vec{E}}{\partial t}) \\
\Rightarrow \nabla^2\vec{E} &= -\mu_0\varepsilon_0\frac{\partial^2\vec{E}}{\partial t^2} \\
\Rightarrow \nabla^2\vec{E} &= \frac{1}{c^2}\frac{\partial^2\vec{E}}{\partial t^2}.
\end{aligned} \tag{1.6}$$

Equation 1.6 is Maxwell's wave equation, where ∇^2 is the Laplacian operator. To obtain the Helmholtz time-independent wave equation, we separate the electric field $\vec{E}$ in Eq. 1.6 into its spatial and time domains:

$$\vec{E}(\vec{r}, t) = u(\vec{r})T(t). \tag{1.7}$$

Substituting Eq. 1.7 into Eq. 1.6 results in

$$\begin{aligned}
\nabla^2(u(\vec{r})T(t)) - \frac{1}{c^2}\frac{\partial^2(u(\vec{r})T(t))}{\partial t^2} &= T(t)\nabla^2u(\vec{r}) - \frac{u(\vec{r})}{c^2}\frac{\partial^2T(t)}{\partial t^2} = 0 \\
\Rightarrow T(t)\nabla^2u(\vec{r}) &= \frac{u(\vec{r})}{c^2}\frac{\partial^2T(t)}{\partial t^2} \\
\Rightarrow \frac{\nabla^2u(\vec{r})}{u(\vec{r})} &= \frac{1}{c^2T(t)}\frac{\partial^2T(t)}{\partial t^2} \\
\Rightarrow \frac{\nabla^2u(\vec{r})}{u(\vec{r})} &= \frac{1}{c^2T(t)}\frac{\partial^2T(t)}{\partial t^2}
\end{aligned} \tag{1.8}$$

Since the left hand side of Eq. 1.8 is only dependent on $\vec{r}$ and the right hand side is only dependent on t, then this equation is valid in the general case if and only if both sides are equal to a constant. Let

$$\frac{\nabla^2u(\vec{r})}{u(\vec{r})} = -k^2 \tag{1.9}$$

and

$$\frac{1}{c^2T(t)}\frac{\partial^2T(t)}{\partial t^2} = -k^2, \tag{1.10}$$

where k is the wave number, Eq. 1.9 is the time-independent Helmholtz equation.

1.2 The Gaussian mode

In this section we show how the Gaussian mode forms part of the solution to the Helmholtz scalar equation, Eq. 1.9. For this calculation, we consider a plane wave modulated by a complex amplitude envelope $A(\vec{r})$, propagating in the z-direction. The complex time-independent wave function of this plane wave is given by:

$$u(\vec{r}) = A(\vec{r}) \exp(-ikz), \tag{1.11}$$

with $k = 2\pi/\lambda$, where λ is the wavelength and z is the longitudinal coordinate. In order for the function $u(\vec{r})$ given by Eq. 1.11 to obey the Helmholtz equation, Eq. 1.9, the complex amplitude must satisfy the paraxial Helmholtz equation:

$$\nabla_T^2 A - i2k\frac{\partial A}{\partial z} = 0, \tag{1.12}$$

where $\nabla_T^2 = \partial^2/\partial x^2 + \partial^2/\partial y^2$ is the transverse Laplacian operator, $\partial^2 A/\partial z^2$ is ignored since it is significantly smaller than $\partial A/\partial z$ that varies slowly within the distance λ. Equation 1.12 yields one of the solutions as a paraboloidal wave, centred around $z = \xi$, and if $q(z) = z - \xi$ then

$$A(\vec{r}) = \frac{A_1}{q(z)} \exp\left(-i\frac{kr^2}{2q(z)}\right), \tag{1.13}$$

with a constant, A_1 and square radius $r^2 = x^2 + y^2$, and ξ is also a constant. This paraboloidal leads to a Gaussian envelope when ξ is purely imaginary: $\xi = iz_R$, where z_R is a real parameter known as the Rayleigh range given by $z_R = \frac{\pi\omega_0^2}{\lambda}$ and $q(z) = z - iz_R$ can be separated into real and imaginary parts:

$$\frac{1}{q(z)} = \frac{1}{R(z)} - i\frac{\lambda}{\pi\omega^2(z)}, \tag{1.14}$$

where $R(z)$ and $\omega(z)$ are the radius of curvature and width of the beam respectively. By substituting Eq. 1.14 in Eq. 1.13 results into the complex amplitude of a Gaussian beam [1]:

$$u(\vec{r}) = u_0\frac{\omega_0}{\omega(z)} \exp\left[-\left(\frac{r^2}{\omega^2(z)}\right)\right] \exp\left[-i\left(kz - \phi(z) + \frac{kr^2}{2R(z)}\right)\right], \tag{1.15}$$

where $u_0 = A_1/iz_R$ is the peak amplitude, ω_0 is the width of the beam at the beam waist.

The Guoy phase shift $\phi(z)$ is given by,

$$\phi(z) = \arctan\left(\frac{z_R}{z}\right). \tag{1.16}$$

The radius of curvature is defined as

$$R(z) = z\left(1 + \frac{z_R^2}{z^2}\right), \tag{1.17}$$

and beam width as

$$\omega(z) = \sqrt{\omega_0^2\left(1 + \frac{z^2}{z_R^2}\right)}. \tag{1.18}$$

The intensity of any field is given by the square of its amplitude $I(\vec{r}) = |u(\vec{r})|^2$, hence the

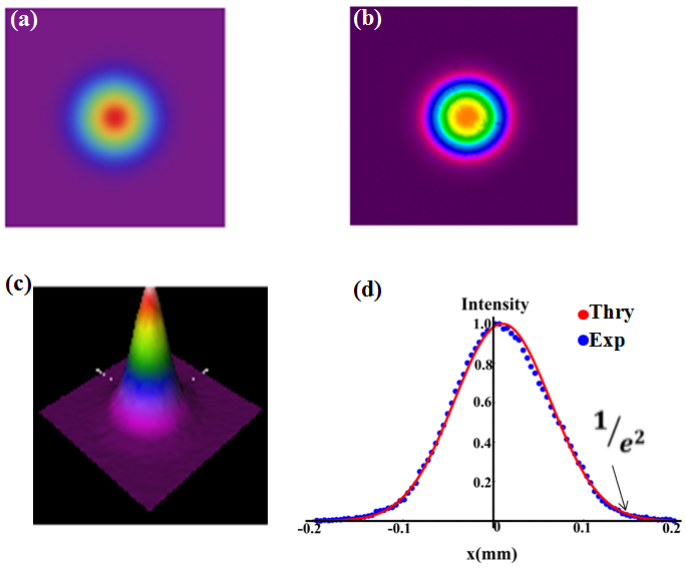

Figure 1.1: (a) The theoretical, (b) experimental CCD images of the Gaussian beam intensity distribution and (c) a 3D profile view of the experimental Gaussian beam indicating the colour coding of the beam. (d) Intensity cross-sectional profile of the Gaussian beam of the theoretical image in red and CCD image in blue, the beam width is measured where the intensity drops by a factor of $1/e^2$.

intensity of a Gaussian beam is given by

$$I(r,z) = |u(r,z)|^2 = I_0 \exp\left[-2\left(\frac{r^2}{\omega^2(z)}\right)\right], \tag{1.19}$$

and

$$I_0 = \frac{2P_0}{\pi\omega^2(z)}, \tag{1.20}$$

where P_0 is the total power of the laser, the intensity distribution of a Gaussian beam is shown in Fig.1.1 (a) and (b) indicating theoretical and experimental images respectively. The colour codes are indicated in the 3D profile image in Fig. 1.1 (c), where the red colour indicates the highest intensity value,while the pink colour indicates the lowest intensity value. The Gaussian beam width is dependent on the propagation distance z, given by Eq.1.18, when the radial distance $r = \omega(z)$, the beam intensity drops by a factor of $1/e^2$ as indicated in Fig. 1.1 (d). The beam width increases gradually with the propagation distance, such that when $z = 0$, $\omega(0) = \omega_0$ which is the waist radius; and when $z = z_0$, $\omega(z_0) = \sqrt{2}\omega_0$. These Gaussian properties are illustrated in Fig. 1.2, where θ_0 is the cone half angle defining angular divergence of the beam, when

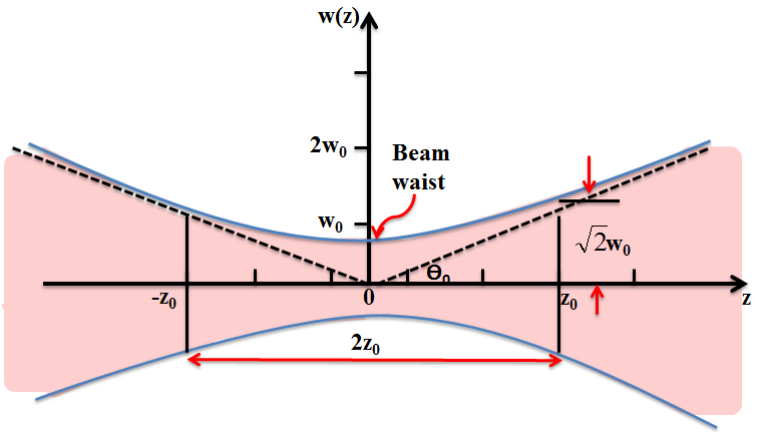

Figure 1.2: The Gaussian propagation parameters, showing the dependence of the beam width on the propagation coordinate (z). $\omega(z)$ is minimum when $z = 0$ and increases linearly with increasing z.

$$z >> z_0, \omega(z) \approx \frac{\omega_0}{z_0} z = \theta_0 z, \tag{1.21}$$

$\Rightarrow$

$$\theta_0 = \frac{\lambda}{\pi\omega_0}. \tag{1.22}$$

The Gaussian phase from Eq. 1.15 is given by

$$\theta(r, z) = kz - \phi(z) + \frac{kr^2}{2R(z)}, \tag{1.23}$$

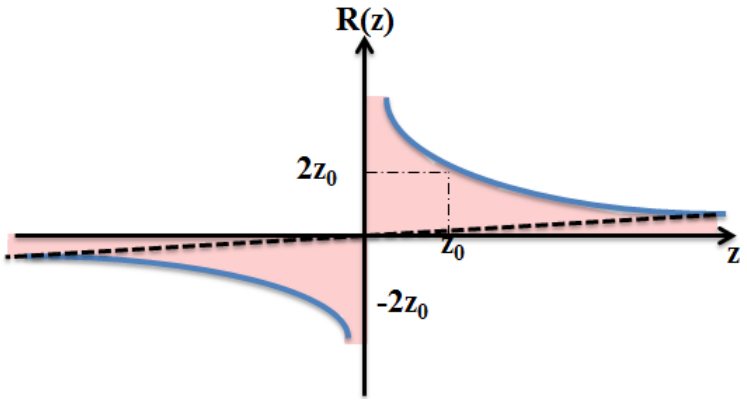

Figure 1.3: The radius of curvature of a Gaussian beam wave front, with the dashed line showing the radius of curvature of the spherical wave.

when $r = 0$, $\theta(0, z) = kz - \phi(z)$. $\phi(z) = \arctan(z/z_0)$ represents a phase retardation as the wave travels from $z = -\infty$ to $z = \infty$, the phase retardation is π referred to as the Guoy effect. The third term in Eq. 1.15 represents the bending of the wave front at $z = 0$, resulting in $R(z) = [1 + (\frac{z}{z_0})] = \infty$ which corresponds to a planar wave front.
The wave front curvature increases with z, until $R(z) = z$ at $z >> z_0$, as shown in Fig. 1.3.

1.3 Laguerre-Gauss beams

The Gaussian mode in the previous section specified in terms of its intensity profile is not the only solution to the time-independent Helmholtz scalar equation. In cylindrical coordinates the Helmholtz scalar equation results in a field distribution that is specified by an azimuthal phase. This solution forms a complete basis set known as the Laguerre-Gauss (LG) beams. The amplitude distribution of the LG modes is given by [1, 3, 4]

$$\begin{aligned} u_{\ell,p}(r, \theta, z) &= \frac{1}{\omega(z)} \sqrt{\frac{2p!}{\pi(|\ell| + p)!}} \left(\frac{\sqrt{2}r}{\omega(z)} \right)^{|\ell|} \exp\left(\frac{-r^2}{\omega(z)} \right) L_p^{|\ell|} \left(\frac{2r^2}{\omega^2(z)} \right) \\ &\times \exp\left(i \frac{kr^2}{2R(z)} \right) \exp(i\ell\theta) \exp[i\Phi(p, \ell, z)], \end{aligned} \tag{1.24}$$

where $\Phi(p, \ell, z)$ is the Gouy phase for the LG mode and is given by

$$\Phi(p, \ell, z) = (2p + \ell + 1) \arctan\left(\frac{z}{z_R} \right). \tag{1.25}$$

The other parameters, such as $R(z)$ and $\omega(z)$, are defined as for the Gaussian beam, in Eqs. 1.17 and 1.18, respectively. The LG modes are characterized by two indices ℓ and p corresponding to the azimuthal and radial indices respectively. When ℓ=p=0, the amplitude distribution in Eq. 1.24 simplifies to a Gaussian amplitude distribution shown in Fig. 1.4 (a). The azimuthal index ℓ of these modes arises from the number of times the helical wave front spirals around the beam axis as the beam propagates. The number of times that this wave front spirals around the propagation axis in π phase change determines the value of ℓ, and hence the amount of orbital angular momentum (OAM) carried by the modes. This is shown in Fig. 1.4 (b) that as the phase varies from 0 to π once a LG mode of $\ell = 1$ is created, and in Fig. 1.4 (c) the phase varies from 0 to π twice creating a LG mode of $\ell = 2$; as well as in Fig. 1.4 (d) the phase varies three times creating a LG beam of $\ell = 3$. This is also true for larger ℓ values, and opposite handedness, for instance $\ell = -10$. As the wave front spirals around the beam axis it creates a phase singularity or an optical vortex, which is illustrated by the null intensity at the center of the LG modes in Fig. 1.4 (b-d). An optical vortex can be found in a randomly scattered beam from a rough surface [3], since there is no intensity at the vortex there is no momentum nor energy, the OAM carried by the modes arises from the surrounding light [3].

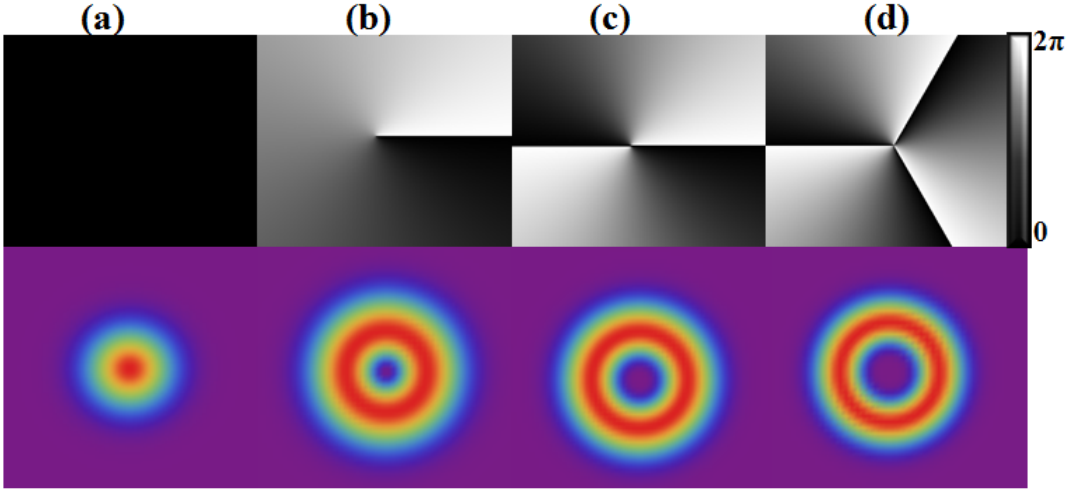

Figure 1.4: The digital holograms showing phase variations of theoretical intensity distribution images of (a) the Gaussian mode, and the LG mode of (b) ℓ=1, (c) ℓ=2, (d) ℓ=3.

It had not been given attention that light beams that have a helical wave front could be created in the laboratory, until Allen *et. al* [5] demonstrated that LG modes carry a well-defined OAM, and that they could be generated using cylindrical lenses to transform

high order Hermite-Gauss mode to a LG mode [6]. Diffraction gratings with a fork dislocation on the beam axis as shown in the first row of Fig. 1.4, were introduced as a simple way of generating these modes [8], implemented digitally to date. The OAM carried by these modes is quantized to $\ell\hbar$ per photon and it was shown by Padgett and Allen [7] that this quantized OAM results from the skew angle of the wave vector for a helical phase wave, given by ℓ/kr. Hence the linear momentum flow of these modes has an azimuthal component of $\ell\hbar/r$. The OAM has an unlimited number of possible states, corresponding to the integer values of ℓ; unlike the spin angular momentum (SAM) that has only two independent states. Prior to Allen's discovery during the 1980s, OAM was said to be carried by emitted photons during atomic transitions [3]. The OAM carried by the LG modes is not only useful in manipulation of micro-particles in optical tweezers [4, 8], but also as a potential solution for encoding information optical communication experiments [9–13] in both free-space and fibre communication. At the single photon level the LG modes were used to illustrate the first quantum entanglement experiment in the OAM basis [14]. Recently the mode division multiplexing (MDM) technique, aimed at improving the bandwidth capacity for optical fibre communication is based on multiplexing LG modes [13, 15, 16] as independent information carries. Tools that focus on the azimuthal detection of these modes such as the azimuthal decomposition technique [17–20] , phase transformation elements [21, 22], interferometry dove prisms [23, 24] have been introduced to extract the information carried by these modes. The LG modes are not the only Helmholtz solution with an azimuthal phase dependence, Elliptical beams [25, 26], and Bessel-Gauss (BG) [27] also form part of the helical family. In the next chapter we will look into the properties of the BG modes.

1.4 Summary

In this chapter we have shown how the Maxwell's wave equation results in the Helmholtz scalar equation through the separation of variables of the electric field. We went further to show how the Gaussian mode forms part of the solution to the Helmholtz scalar equation for a plane wave modulated by a complex amplitude. We have also indicated that the cylindrical solution to the equation results in the LG function that has an azimuthal dependence.

Chapter 2

Bessel-Gauss beams

2.1 Introduction

As classical waves propagate they spread out as a result of diffraction. These classical waves include the Gaussian and Laguerre-Gauss modes that have been discussed in the previous chapter. The diffraction-free solution of the Helmholtz scalar equation was first pointed out by J. Durnin [28] using a Bessel function. Ideally Bessel beams are non-diffracting over an infinite region and carry infinite power. Experimentally, these beams are realised and remain

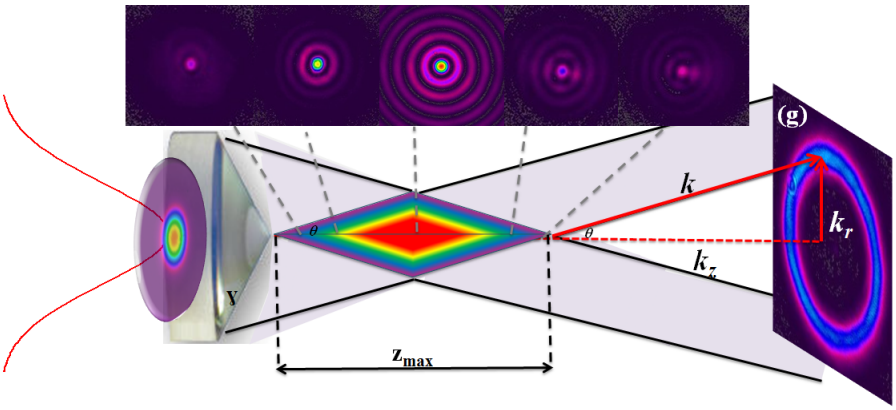

Figure 2.1: Propagation of a BG beam of $\ell = 0$ and $k_r = 0.31$ rad/pixel, with $z_{max} = 0.34$ m as calculated using Eq. 2.18.

diffraction free within a finite distance, while maintaining the propagation properties of an ideal Bessel beam. In Fig. 2.1 a Gaussian beam is refracted by an axicon to formulate a zeroth order Bessel beam within a finite region in the coloured zone denoted as z_{max}. At half-z_{max} the refracted waves interfere completely resulting in a full zeroth order Bessel structure with a maximum number of bright concentric rings of light and a central maximum

as opposed to the edges of the diamond region where the Bessel structure has a minimum number of bright rings of light. These bright rings of light are a result of the constructive interference of the plane waves. As the refracted waves move away from each other, the Bessel structure disappears and an annular ring of radius k_r is formed, where k_r is the radial wave vector related to the longitudinal wave vector k_z by the angle θ. The formation of the Bessel structure by the diffraction of a Gaussian beam [29, 30] led to them being known as the Bessel-Gauss (BG) beams to date, the details on how these beams are generated experimentally will follow in the next subsection. To illustrate that the Bessel function forms part of the solution to the Helmholtz scalar equation, we rewrite the Eq. 1.9 in cylindrical coordinates:

$$\frac{1}{r}\frac{\partial}{\partial r}\left(r\frac{\partial}{\partial r}\right)+\frac{1}{r^2}\frac{\partial^2 u}{\partial \theta^2}=-k^2u(r,\theta), \tag{2.1}$$

using the separation of variables:

$$u(r,\theta)=R(r)\Theta(\theta). \tag{2.2}$$

Substituting Eq. 2.2 into Eq. 2.1:

$$\frac{1}{r}\frac{\partial}{\partial r}\left(r\frac{\partial R(r)\Theta(\theta)}{\partial r}\right)+\frac{1}{r^2}R(r)\frac{\partial^2\Theta(\theta)}{\partial \theta^2}=-k^2R(r)\Theta(\theta), \tag{2.3}$$

dividing by $\Theta(\theta)$, and since the partial derivatives are a function of one variable the equation becomes,

$$\frac{1}{r}\frac{d}{dr}\left(r\frac{dR(r)}{dr}\right)+\frac{R(r)}{r^2}\frac{1}{\Theta(\theta)}\frac{d^2\Theta(\theta)}{d\theta^2}=-k^2R(r), \tag{2.4}$$

grouping the like terms in Eq. 2.4 together:

$$\frac{r^2}{R(r)}\left[\frac{1}{r}\frac{d}{dr}\left(r\frac{dR(r)}{dr}\right)+k^2R(r)\right]=-\frac{1}{\Theta(\theta)}\frac{d^2\Theta(\theta)}{d\theta^2}. \tag{2.5}$$

Since the left hand side of Eq. 2.5 is only dependent on r and the right hand side is only dependent of θ, then this equation is valid in the general case if and only if both sides are

equal to a constant.

$$-\frac{1}{\Theta(\theta)}\frac{d^2\Theta}{d\theta^2} = v^2, \tag{2.6}$$

also

$$\frac{r^2}{R(r)}\left[\frac{d}{dr}\left(r\frac{dR}{r}\right) + k^2R(r)\right] = v^2. \tag{2.7}$$

Applying the product rule on the first term of the Eq. 2.7 RHS:

$$r^2\frac{d^2R}{dr^2} + r\frac{dR}{dR} - (v^2 - kr^2)R = 0, \tag{2.8}$$

where k is a constant value. Eq. 2.8 is the Bessel differential equation, the solution to the equation defines a Bessel function which can be written in the form:

$$R(r) \propto J_v(kr) + H_v(kr), \tag{2.9}$$

where J_v and H_v are the Bessel functions of order v. For the purpose of this dissertation the Bessel beam will be written as:

$$u(r, \phi, z = 0) = J_\ell(k_r r)\exp(i\ell\phi), \tag{2.10}$$

where J_ℓ is the Bessel function of order ℓ, k_z and k_r are the longitudinal and radial wave vectors, and r, ϕ and z are the radial, azimuthal and longitudinal components respectively. The Gaussian envelope in Fig. 2.2 (a) changes the cross-section of the BG beams during propagation, this envelop tends to overlap less for an increasing propagation distance (z) [30]. As the BG beam propagates beyond the allocated region where it has the properties of the ideal Bessel beam, the overlap between the Gaussian and the BG profiles is determined by the ratio between the conical angle θ derived from Fig. 2.1,

$$\begin{aligned} \sin\theta &= \frac{kr}{k}, \\ \theta &\approx \frac{kr}{k}, \end{aligned} \tag{2.11}$$

and the divergence angle of a single Gaussian beam from Eq. 1.22,

$$\theta_0 = \frac{\lambda}{\pi\omega_0}. \tag{2.12}$$

The ratio becomes,

$$\theta/\theta_0 = \frac{\omega_0 k_r}{2}. \tag{2.13}$$

When $\theta/\theta_0 > 1$, the component of the Gaussian beam gives rise to an annular ring of a radius $k_r = \sqrt{k_x^2 + k_y^2}$, with its one dimensional cross-sectional profile shown in Fig. 2.2 (b) of radius $x = k_x \lambda f$, and f is the focal length of a Fourier lens.

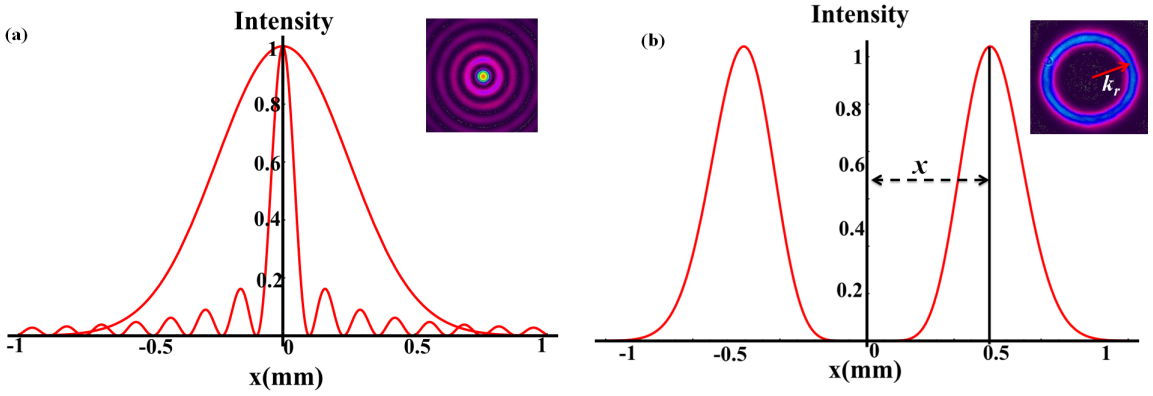

Figure 2.2: (a) Bessel profile enveloped by a Gaussian profile and (b) the far-field BG profile resulting in an annular ring.

The zeroth-order BG beams have a central maximum with a smoothly varying intensity along the propagation distance, which peaks at $\frac{1}{2}z_{max}$. The diffraction-free central maximum offers a focal line of light which is the most useful BG feature in the process of optical manipulation of micro-particles [27, 31, 32]. During this process an optical gradient force traps and confines a microscopic particle at the focus of a laser beam. Another striking property of the BG beam which is remarkable for the optical trapping of particles is the fact that the plane waves that interfere to form a Bessel beam are able to move past an obstruction giving rise to the self-healing property of the BG beam. The minimum distance that the beam propagates after encountering an obstruction before the phase and amplitude reconstruction occurs, depends on the size of the obstacle.To obtain this minimum self-healing distance let us look into the propagation of the conical waves after encountering an obstruction [33] for an obstruction placed in the propagation path of the BG beam as shown in Fig. 2.3. Consider a cross-section of a surface of the obstruction perpendicular to the z-axis as shown in Fig. 2.4, this

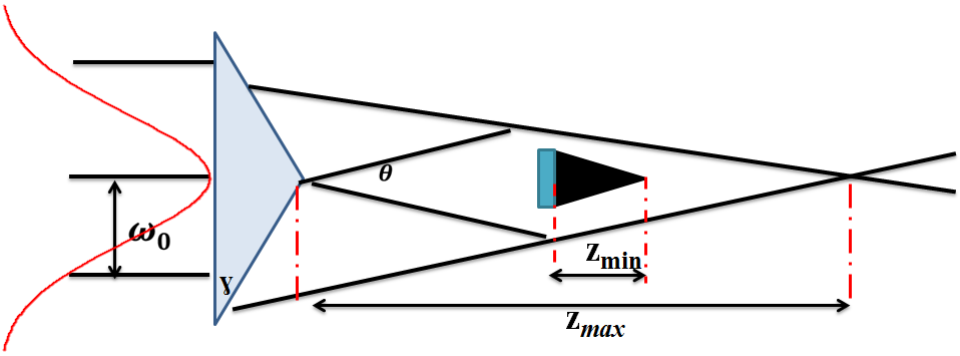

Figure 2.3: The obstruction placed within the z_{max} region, with its shadow region covering z_{min} distance.

cross-section is between points a and b on the boundary of the obstacle, and as a result only two conical waves (CW_1 and CW_2) contribute to the BG beam at any given point. The projection of the two conical waves give rise to three different regions, (1) the region in which one conical wave contributes i.e $a_2 < \rho < a_1$ and $b_2 < \rho < b_1$, where CW_1 and CW_2 contribute respectively. (2) The region in which non of the conical waves contribute "the shadow region" confined within $a_1 < \rho < b_2$, (3) the region in which the conical waves interfere to form a BG beam. These numbers are indicated on the Fig. 2.4, for an obstruction of width $D = b - a$ placed at some distance ρ from the central axis of the BG beam. At some distance z after the obstruction, the contributions of the conical waves CW_1 and CW_2 at the points a and b are:

$$\begin{aligned} a_1 &= a + z\tan\theta, \\ a_2 &= a - z\tan\theta, \\ b_1 &= b + z\tan\theta, \\ b_2 &= b - z\tan\theta. \end{aligned} \tag{2.14}$$

For reconstruction to take place, it is required that at $z = z_{min}$, where $b_2 \leqslant a_1$ the shadow region vanishes and the BG beam be reconstructed. This implies that we must solve the

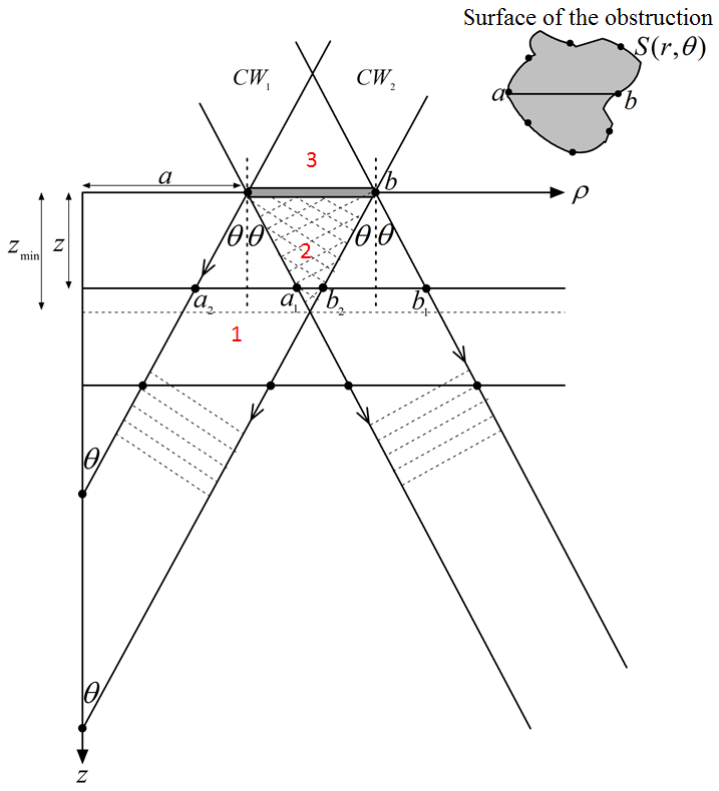

Figure 2.4: Cross-section of an obstacle placed between two conical waves CW_1 and CW_2 forming a z_{min} shadow region. Sample figure adapted from [33].

equality $b_2 = a_1$, from Eq. 2.14:

$$\begin{aligned} b - z\tan\theta &= a + z\tan\theta \\ \Rightarrow 2z\tan\theta &= b - a \\ \Rightarrow 2z_{min}\tan\theta &= D \\ \therefore z_{min} &= \frac{D}{2\tan\theta}. \end{aligned} \tag{2.15}$$

We conducted an experiment to verify the self-healing property of the BG beams based on the theory above. An obstacle of size $D = 0.03$ cm was placed along the propagation path of BG beam of ℓ=1 and $k_r = 0.25$ rad/pixel. Using Eq. 2.11 and Eq. 2.15 the minimum distance after which the BG beam reconstructed was given by $z_{min} = 9.5$ cm. During the experiment an obstacle was moved around the z_{max} region, while our detector was fixed at the z_{max} position. In Fig. 2.5 (a) the obstacle was placed at 3/4 z_{max} such that the shadow region could fall on the detector. The obstacle was them moved 6 cm away from the detector where a partially reconstructed BG beam fell on the detector as shown in Fig. 2.5 (b). Later in Fig.

2.5 (c) the obstacle was moved 11 cm away from the detector such that a fully reconstructed BG beam fell on the detector. Using one of our detection tools, which is outlined in detail in chapter (4), we were able to study the effects of the obstruction on the radial and azimuthal components of the BG beam.

The results in Fig. 2.6 shows (a) the radial and (b) azimuthal spectrums, where there is a minimal azimuthal distortion, whilst there is a broader radial spectrum due to the obstruction respectively, but as the beam propagates beyond the self-healing distance the radial spectrum becomes narrower. This self-healing property of BG beams allows for a simultaneous trapping

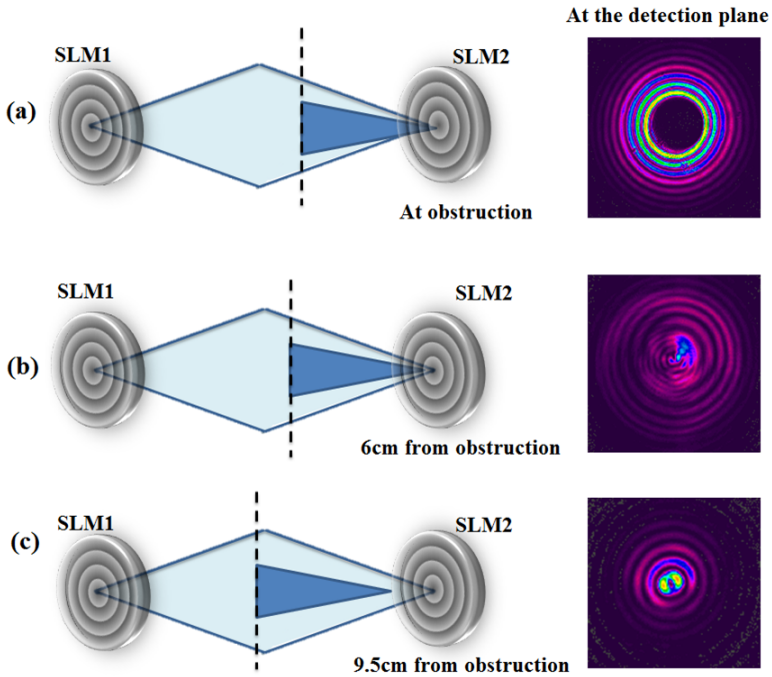

Figure 2.5: The position of the shadow region is dependent on the position of the obstruction in relation to the detection plane, (a) is the case when the obstruction is at $3/4z_{max}$, (b) 6 cm from the detector, and (d) 9.5 cm from the detector.

of multiple micro-particles [34], placed at different chambers a few cm apart such that are simultaneously trapped because as the beam traps particles in one chamber it propagates beyond the self-healing distance and traps particles in the next chamber. Other applications of the zeroth-order BG beams include atomic dipole traps of very large aspect ratio [27]. Electron Bessel beams have been generated and shown to have the same properties as in the BG light beams, and have also shown to improve the performance of an electron microscope [35]. High-order BG beams (i.e $\ell > 0$) in Eq. 2.10 are characterized by the azimuthal index ℓ and have a central minimum. Similar to the LG beams they also carry OAM of $\ell\hbar$ per photon. These OAM carrying beams can transfer momentum to

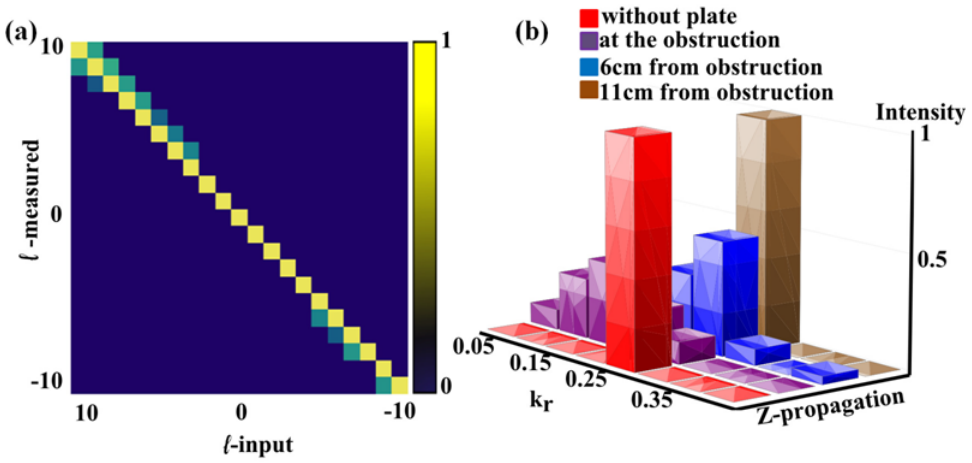

Figure 2.6: (a) ℓ spectrum of the BG beam of $k_r = 0.25$ rad/pixel at the shadow region, and (b) $k_r = 0.25$ rad/pixel spectrum at different planes in relation to the obstruction.

micro-particles and the first simultaneous transfer of SAM and OAM to a particle was first observed using high-order BG beams [36, 37]. The non-diffractive nature of the central minimum of the BG can be used as an atomic guide, where atoms can be transported to an extended distance without transverse spreading as oppose to other hollow beams [27].
The OAM carried by the helical beams [4, 20] can be used as a basis for information encoding in optical communication [13, 16, 38], even at the single photon level [96], the self-healing [27, 33, 39] property of the beams has shown to be useful in recovering entanglement between pairs of photons [40]. Although information can be encoded in these modes, we need efficient techniques to be able to extract the encoded information not only in one dimension [17, 41], but also in two dimensions [42, 43, 57]. In this thesis we outline methods for generating and extracting the information encoded in BG beams using diffractive optical elements.

2.2 Generation of Bessel-Gauss beams

The zeroth order BG beam was first demonstrated by J. Durnin [29], using a circular ring-slit of a diameter d and width Δ placed at the focal plane of a lens. Each point source along the slit was transformed into plane waves lying on the surface of a cone creating a zeroth order BG beam. This is not the only method implemented in the generation of the BG beams, other diffractive optical elements (DOEs) such as axicons [27, 44–47] and appropriate diffraction holograms [48–51] can be utilised to generate the BG modes. Unlike an ordinary lens which

creates a point focus, an axicon refracts all incoming rays at approximately the same angle, producing narrow focal lines extended along the optical axis [52]. It has a conical shape, made of glass with refractive index n, and an opening angle γ, this opening angle determines the cone angle which defines the finite Bessel region. Figure 2.7 (a) shows incoming parallel rays being refracted by such an axicon of an apex angle β. The rays are refracted at approximately the same angle, hence the rays interfering to form the BG region are parallel. The interference angle (the cone angle) θ, is derived from the zoomed in Fig. 2.7 (b):

$$\begin{aligned}
\widehat{a} &= 90^\circ - \gamma \\
\theta_1 + \widehat{a} + 90^\circ &= 180^\circ \\
\Rightarrow \theta_1 &= \gamma \\
\widehat{b} &= 180^\circ - 2\theta - \widehat{c} \\
\Rightarrow \widehat{b} &= 90^\circ - \theta - (90^\circ + \gamma - \theta) \\
\Rightarrow \widehat{b} &= 90^\circ - \theta - \gamma \\
\theta_2 &= 180^\circ - \widehat{b} - 90^\circ \\
\Rightarrow \theta_2 &= \theta + \gamma
\end{aligned} \tag{2.16}$$

Snell's law of refraction

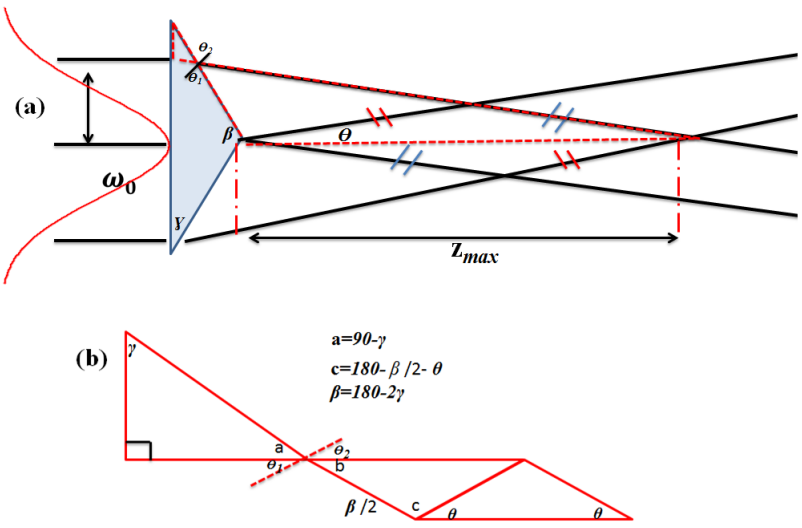

Figure 2.7: (a) The rays refracted by an axicon, interfering to form the Bessel region. (b) The Bessel region zoomed in to determine the cone angle θ.

$$
\begin{aligned}
n_1 \sin\theta_1 &= n_2 \sin\theta_2 \\
n_2 &= 1 \\
n_1 &= n \\
\Rightarrow n\theta_1 &= \theta_2 \\
n\gamma &= \theta + \gamma \\
\Rightarrow \theta &= \gamma(n-1)
\end{aligned} \tag{2.17}
$$

The finite region within which the BG beam remains diffraction free is given by

$$
\begin{aligned}
z_{max} &= \frac{\omega_0}{\theta} \\
&= \frac{\omega_0}{\gamma(n-1)}.
\end{aligned} \tag{2.18}
$$

The axicon angle γ determines the spacing between the concentric rings of light of the BG

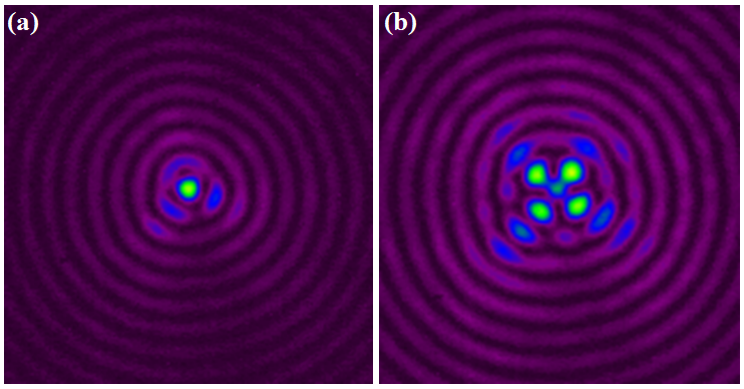

Figure 2.8: The zeroth-order BG beam (a) generated by an axicon, (b) as a result of mis-aligned axicon.

beam. In order to generate Bessel modes of differing ring spacing one would require axicons of differing opening angles γ, but this would be expensive to produce. Another disadvantage is that the axicon is very sensitive to alignment as seen in Fig. 2.8 (b), hence using an axicon as a tool to generate BG beams is inefficient. As a result we will investigate the generation of the BG modes digitally using a spatial light modulator (SLM) encoded with either a digital ring-slit or a digital axicon.

2.3 Digital generation of BG beams

2.3.1 Spatial light modulator

A SLM in Fig. 2.9 (a) is an electronic device that has a liquid crystal display (LCD) shown in Fig. 2.9 (b). The liquid crystal molecules are aligned between electrodes as seen in Fig. 2.9 (c) with a voltage dependent orientation. A gray scaled digital hologram that mimics an arbitrary DOE is used to apply a voltage across the electrodes. The molecules tilt in the direction of the applied electric field as shown in Fig. 2.10, as a result the phase of the horizontal component of a linearly polarized incident beam will be modulated and diffracted to the first diffraction order, to give the desired spatial mode. The SLM that was in use for

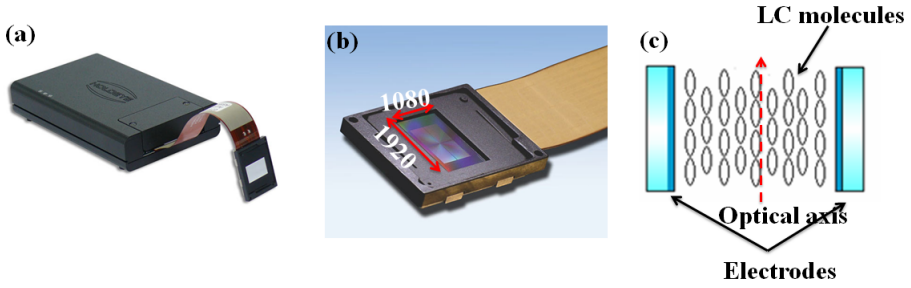

Figure 2.9: (a) Holoeye SLM, (b) LCD screen with its pixel dimensions, and (c) liquid crystal molecules aligned in between two electrodes.

this work is a Holoeye PLUTO VIS SLM, with a screen dimension of 1080×1920 pixels. The gray scale level is scaled in such a way that the black color corresponds to no voltage applied, implying that there is no phase modulation. As the gray-scale increases from 0 to some number, the applied electric field causes the molecules to tilt from their original position to the direction of the applied electric field. This implies that the index of refraction of the display changes accordingly, resulting in the phase of the beam changing. The equation below verifies this relationship:

$$\delta = \frac{2\pi}{\lambda} n, \tag{2.19}$$

where δ is the phase shift, λ is the wavelength, and n is the index of refraction. Since the SLM is a digitally controlled birefringent device, it can produce any desired diffraction pattern, but with limited efficiency. This limited efficiency is due to the 2D structure of the array of pixels, representing a 2D grating which results in light being diffracted into many

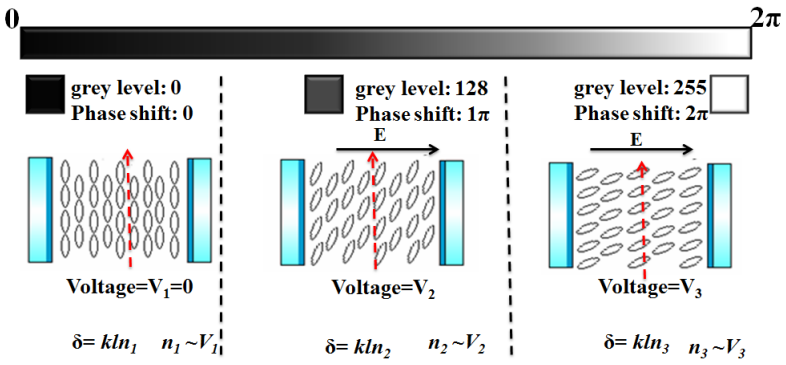

Figure 2.10: The relationship between the different gray-levels and the applied voltage across the electrodes, causing a tilt in the molecules of the liquid crystal.

orders. This causes loss in light intensity. Some parts of the SLM are not covered by pixels, hence some of the incident field is absorbed by the non-pixel area. The quality of the first diffracted order is affected by its overlap with the non-diffracted zero-order, this can be improved by adding a grating onto the phase hologram to separate the diffracted and the non-diffracted order. This is shown in Fig. 2.11, where a Gaussian beam passes through a fork hologram of $\ell = 1$ with a particular grating size added to it, as a result the modes are separated into zeroth and first order which is the order of interest with most of the Gaussian intensity directed to it.

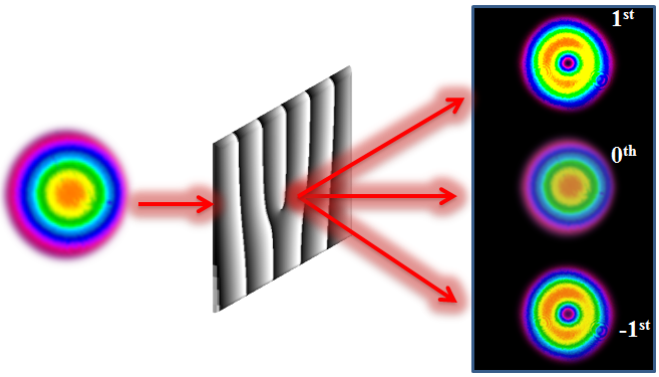

Figure 2.11: The Gaussian beam passing the fork hologram to generate a vortex beam on the first diffracted order.

2.3.2 Digital Axicon

To generate BG beams digitally we encode a hologram with a transformation function defining the phase of the BG modes from the Bessel function in Eq. 2.10. Looking at Eq. 2.11 and the Eq. 2.17, we can clearly see that the cone angle θ is directly proportional to the

radial wave vector k_r. Hence the transmission function of an axicon in Fig. 2.12 (a) that is

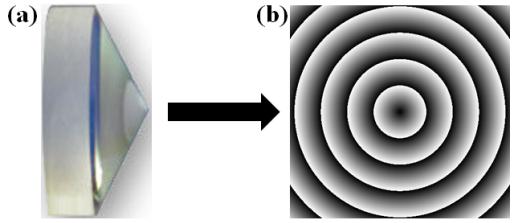

Figure 2.12: Diffractive optical elements that can be used to generate the zeroth-order BG beam, (a) conical lens and its digital form (b) an axicon hologram.

used to create a digital axicon in Fig. 2.12 (b), with the control over k_r (spacing between the rings of light) and ℓ (azimuthal variation of the BG modes) is given by:

$$\begin{aligned} t(\delta) &= \exp(i\delta) \\ &= \exp(ik_r r + i\ell\phi), \end{aligned} \tag{2.20}$$

to generate the high-order BG beams using the transmission function, the azimuthal index ℓ

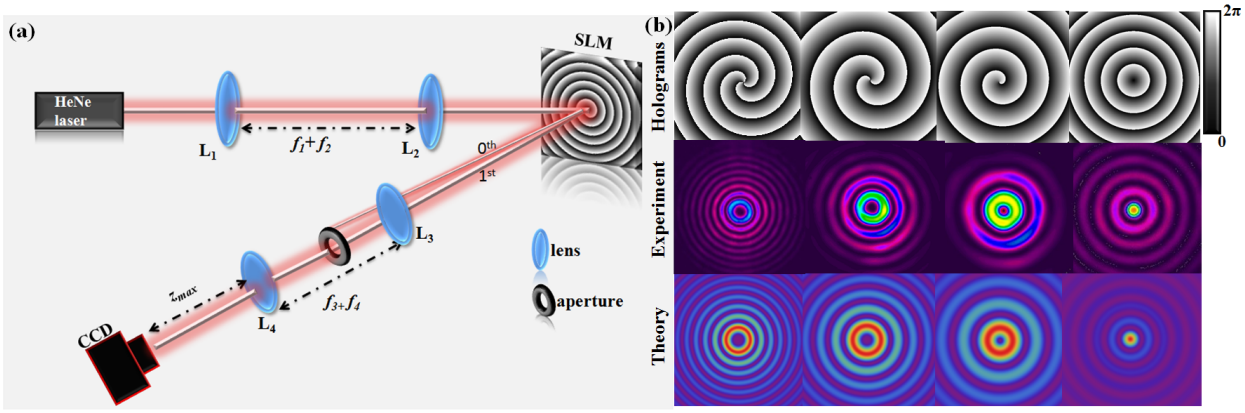

Figure 2.13: (a) The experimental setup used to generate BG beams.(b) The BG beams of different k_r and ℓ, generated by a digital axicons. Holograms are presented in the first row and corresponding experimentally recorded and theoretical calculated intensity profiles in the second and third rows, respectively.

must not equal zero. The code used to generate the holograms is shown in the appendix(A). The experimental setup as shown in Fig. 2.13 (a) was used to generate the BG beams using a digital axicon, where a Helium-Neon (HeNe) laser was expanded using a lens telescope of $L1$ ($f_1 = 100$ mm) and $L2$ ($f_2 = 300$ mm), with a beam magnification $M = f_2/f_1 = 3$. This $3\times$ magnified beam was directed onto the SLM encoded with the axicon hologram, the reflected beam was imaged using a $4f$ imaging system to the CCD camera where the propagation

properties of the BG beams were studied along the z_{max} region. The unwanted diffracted orders were filtered using an aperture. We can obtain a variety of holograms with differing values for k_r and ℓ to generate corresponding BG beams as shown in Fig. 2.13 (b).

2.3.3 Digital spiral ring-slit

Durnin's ring-slit [29] can be programmed digitally [53] with control over the phase of the output beam, generating not only the zeroth-order BG, but also high-order BG beams. With Durnin's ring-slit, light is only transmitted through the ring and blocked everywhere else. To incorporate this digitally, one needs to be able to control both the phase and amplitude of the incident beam. This is possible by generating a hologram with a checker-board pattern surrounding the phase modulating ring-slit. This checker-board pattern is simply an array of

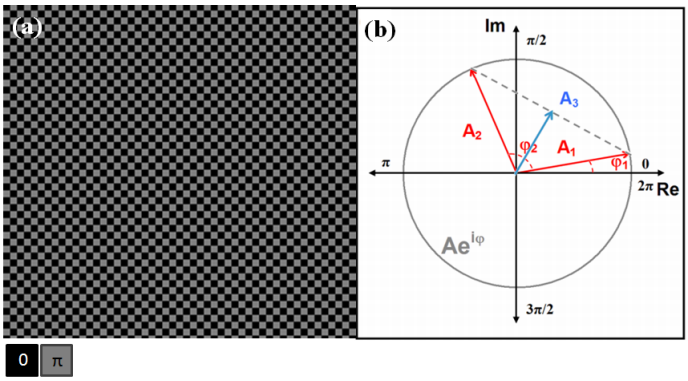

Figure 2.14: (a) Checker board pattern of arrays of pixels varying from 0 to π, (b) complex plane representing the phase values in (a) in form of vectors. Sample image adapted from [54].

alternating sets of pixels that are out of phase by π, and can be used to mimic an amplitude mask, modulating the amplitude of the incident beam. The phase values of the checker-board pattern in Fig. 2.14 (a) have uniform weighting of 0 and π, this is represented in the complex plane in Fig. 2.14 (b). In the complex plane the uniform phase values are represented in form of vectors A_1 and A_2 having the same amplitude, in opposite directions along the x-axis [54]. As a result the resultant A_3 positioned at the origin of the complex plane, has no amplitude. This implies that the average amplitude of the field at the image plane of the checker-board hologram is zero. When the field is observed at the Fourier plane, there is a zero intensity along the propagation axis, and due to the spatial frequency of the checker-board the light is shifted away from the origin. When there is a phase varying ring-slit added on the checker-board in Fig.2.15 (a) the phase of the field is modulated and observed at the origin at

the Fourier plane [53], as illustrated in Fig.2.15 (b). This is not the only method that can be implemented to modulate the amplitude of the field using a phase only SLM, the Arrizon technique [55], that we have successfully implemented in the phase and amplitude modulation of LG modes [56] is another method of modulating the amplitude of the field.
The transmission function of the ring-slit aperture is:

$$t(r,\phi) = \left\{ \begin{array}{ll} \exp(i\ell\phi) & \text{if } R - \frac{\triangle}{2} \leq r \leq R + \frac{\triangle}{2} \\ 0 & \text{elsewhere} \end{array} \right\},$$

where the azimuthal component ℓ is restricted to the radial coordinate R, which is the radius of the ring-slit and Δ is the width of the ring-slit as shown in Fig. 2.15, the hologram was produced using the matlab code shown in Appendix (A). The output field is given by:

$$u(r,\phi,z_0) = \exp(i\ell\phi)\exp(ik_z z_0), \tag{2.21}$$

where $k_z = k\cos(\theta)$ is the longitudinal wave vector. The main difference between generating

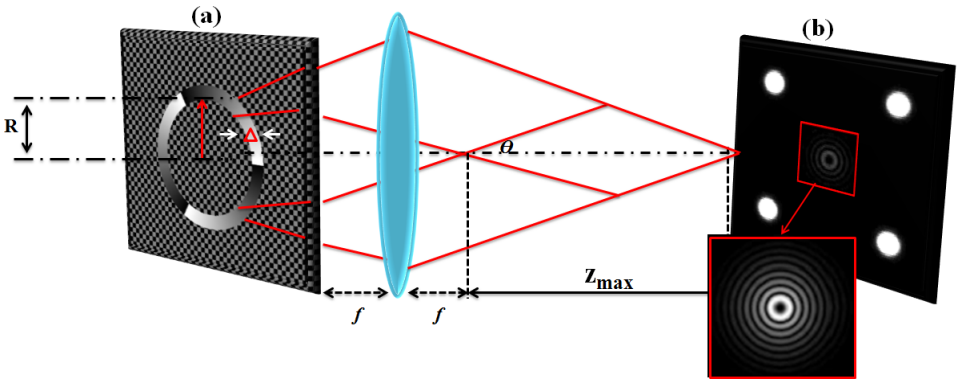

Figure 2.15: The generation of a BG beam using (a) the spiral ring-slit, observed at (b) the Fourier plane of a lens of focal length f.

the BG beam with an axicon and the spiral ring-slit is that the output field is observed at the near and far-field, respectively.

2.4 Summary

In this chapter we have introduced a diffraction free solution to the Helmholtz equation, known as the BG beam, and we outlined the propagation properties such as their

diffraction-free and self-healing properties. We also investigated the tools that can be used to generate the BG beams such as conical lens, which is very sensitive to alignment and limited to only being suitable to generate a zeroth order BG of a particular ring spacing. Using a SLM we have shown that we can create digital axicons, by defining the transmission functions of the diffractive optic we wish to replace, so as to generate any desired BG and vortex modes. This is achieved by simply reflecting the Gaussian beam off the SLM encoded with an appropriate transmission function, and observing the generated output field at the point of observation.

Chapter 3

Detection of BG beams

3.1 Introduction

As we have shown that we can generate OAM carrying BG modes, we will also show a technique we have developed to extract the information carried by these beams in two dimensions. It has been previously shown that an interferometer composed of dove prisms in each arm [23], with the relative angle between prisms given by $\Delta\alpha = \frac{\pi}{2}$, can separate the odd and even ℓ values, in separate output ports for the azimuthal detection of LG modes in single photons. Another one dimensional detection tool that has been used to extract the amount of OAM carried by helical modes, is based on the fact that the process of generating LG modes digitally with fork holograms illuminated by a Gaussian mode is reversible. This means that by illuminating a fork hologram grating of $-\ell$ with the beam carrying OAM of ℓ results in a Gaussian beam as shown in Fig. 3.1. This process is known as azimuthal

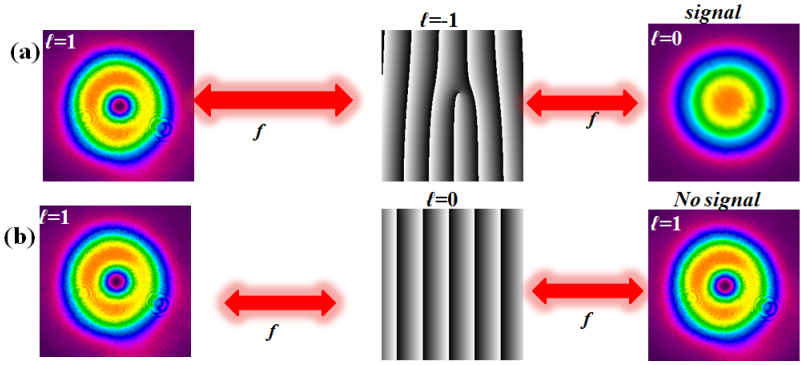

Figure 3.1: Azimuthal decomposition resulting in (a) a signal for matching ℓ, and (b) no signal for non-matching ℓ.

decomposition [17, 18] of light, which can be used to detect any arbitrary azimuthally varying field of localized azimuthal components. This azimuthal detection technique is achieved by expanding any arbitrary field into the angular harmonics basis $\exp(i\ell\phi)$ in Eq. 3.1, with ℓ dependent modal weight co-efficients $c_\ell(r)$, that are obtained by taking the inner product of the field with the azimuthal filter: the field function

$$u(r,\phi) = \sum c_\ell(r)\exp(i\ell\phi), \tag{3.1}$$

with its modal weight co-efficients given by

$$\begin{aligned} c_\ell(r) &= |\langle u(r,\phi)|\exp(-i\ell\phi)\rangle| \\ &= \frac{1}{2\pi}\int_0^{2\pi} u(r,\phi)\exp(-i\ell\phi)d\phi. \end{aligned} \tag{3.2}$$

This inner product will give a value for $c_\ell(r)$ when the field $u(r,\phi)$ has a complex conjugate of the azimuthal filter in its azimuthal component i.e $u(r,\phi) \propto \exp(+i\ell\phi)$, otherwise the weighting will be zero (no on axis intensity) as in Fig. 3.1 (b).

3.1.1 Efficient sorter of BG beams

A two dimensional detection of BG beams has been introduced, where refractive optical elements have been used to transform an azimuthally varying field to a linear phase varying field through the conformal mapping technique. This linear phase varying field was focused into cylindrical lenses to simultaneously separate the azimuthal (ℓ) and radial (k_r) components of the BG modes, such that a signal was detected at ℓ and k_r dependent transverse positions [22, 57, 58]. The concept behind this technique was based on a fact that a lens can focus a plane wave to a spot of light in its focal plane. The transverse position of the spot at the focal plane of the lens depends on the transverse phase gradient of the plane wave, which allows for multiple plane waves to be distinguishable from each other at the point of observation. Since the BG modes are azimuthally varying fields, we needed a way to transform these modes to a linear phase gradient. An optical geometric approach known as the conformal mapping technique was used to perform this transformation [22, 41]. This technique can be used to map one coordinate system to another, while preserving the angles,

this was implemented using diffractive optical elements (with a transformation efficiency of about 85%) to map a position at an input (x, y) coordinate system to a position at an output (u, v) coordinate system in the Cartesian plane. The coordinate functions from (x, y) to (u, v) were given by [58]:

$$v = \frac{d}{2\pi}, \tag{3.3}$$

and

$$u = -\frac{d}{2\pi} \ln \frac{\sqrt{x^2 + y^2}}{b}, \tag{3.4}$$

where b is the scaling factor of the radial component, d is the aperture size of one of the diffractive optics. Figure 3.2 (a) is the phase transformation element with its height (H_1)

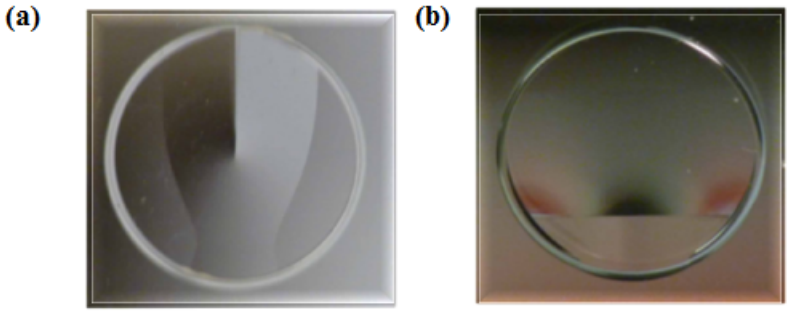

Figure 3.2: (a) Phase transforming element, and (b) phase correcting element. Sample image adapted from [41]

derived from the phase function in [22], and is given by

$$H_1(x, y) = \frac{a}{f(n-1)} \left[y \arctan(y/x) - x \ln \left(\frac{\sqrt{x^2 + y^2}}{b} \right) + x - \frac{1}{a} \left(\frac{1}{2}(x^2 + y^2) \right) \right], \tag{3.5}$$

where f is the focal length of the integrated lens given by the last term of Eq. 3.5. The parameter $a = d/2\pi$ determines the position of the resulting horizontal line, ensuring the mapping of the azimuthal angle range to the full width d of the second element.

When an azimuthally varying beam of wavelength λ passes through this element of height H_1, with a refractive index n, the effective optical path length of this beam changes, and the change in the optical length changes the phase of the beam by $\Delta\Phi = \frac{2\pi(n-1)H_1}{\lambda}$ and its phase gradient by $2\pi\ell$; such that the transverse position of the focused spot is ℓ dependent.

The change in the phase of the beam during the transformation introduces phase distortions to the transformed beam. This phase distortion is corrected by the second optical element in

Fig. 3.2 (b) of height,

$$H_2 = -\frac{ab}{f(n-1)}\left[\exp\left(\frac{-u}{a}\right)\cos\left(\frac{v}{a}\right) - \frac{1}{ab}\left(\frac{1}{2}(u^2+v^2)\right)\right]. \tag{3.6}$$

This phase element was placed at f away from the first element, and the manufacturing process of these elements is outline in [41]. Using cylindrical lenses the resulting horizontal

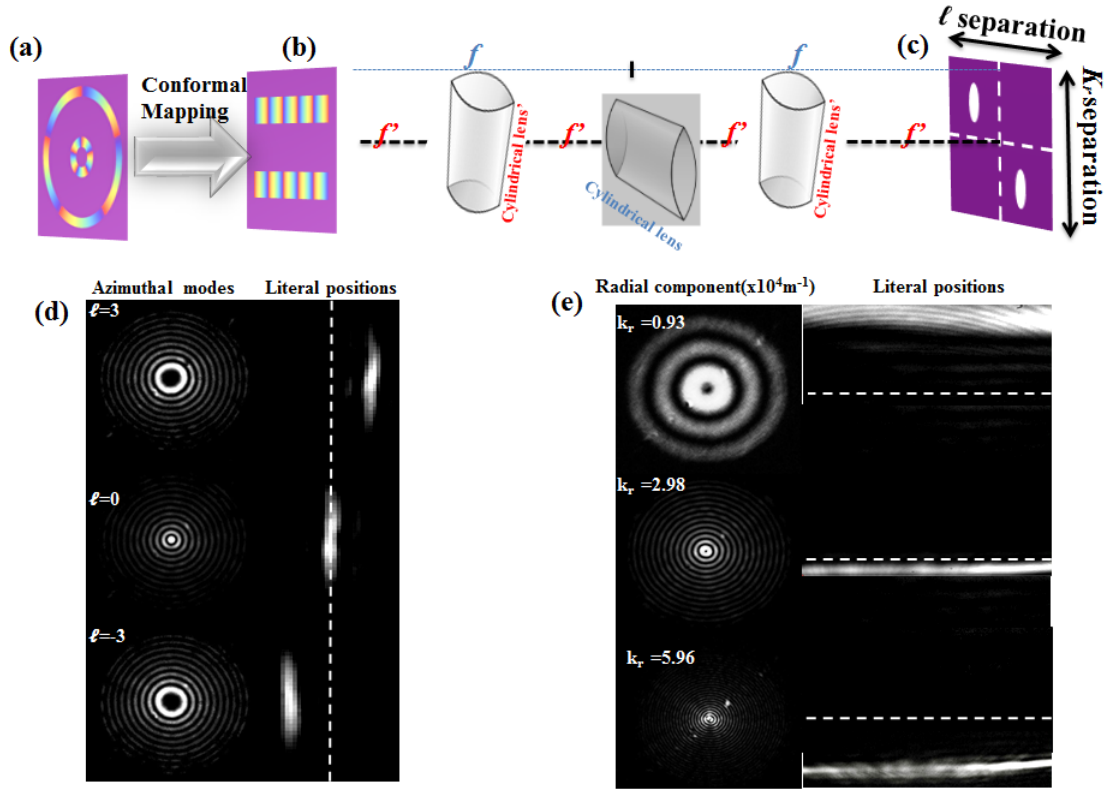

Figure 3.3: (a) Superposition of BG modes unravelled through the conformal mapping technique to (b) a set of parallel horizontal lines passing through cylindrical lenses to be detected in (c) where the radial and azimuthal components are separated. The results of (d) azimuthal detection, and (e) radial detection.

line was imaged to a point of observation to give a vertical spread of the radial component:

$$\Delta_V = \frac{d}{2\pi}\ln\left(\frac{k_r f}{kb}\right). \tag{3.7}$$

One of the cylindrical lenses was used to take the Fourier transform of the horizontal line to produce spots in ℓ-dependent horizontal position given by:

$$\Delta_H = \frac{\lambda}{f}\ell d. \tag{3.8}$$

The simultaneous detection of the radial and azimuthal components was achieved through the optical system outlined in Fig.3.3, where Fig.3.3 (a) the superposition of two azimuthal phase varying annular rings of two BG beams are mapped to linear phase varying modes in (b). Cylindrical lenses (CL) were arranged in a 4-f system to map the transverse momentum modes to different x- and y-coordinates in (c). The corresponding results show the displacement of 3.3 (d) the spot in the ℓ-dependent position, and 3.3 (e) the vertical spread in k_r. In the next section, we introduce another two dimensional detection tool of BG beams using digital axicons.

3.2 Detection of BG modes using a digital axicon

Similarly to the azimuthal decomposition technique outlined in the previous subsection we can use the digital axicon that consists of a spiral phase $\exp(i\ell\phi)$ and a radial component k_r, as a 2-dimensional detection tool of the BG beams. In this process we considered a ray based analysis of the formulation of BG beams as generated by an axicon, where an approximate plane wave is refracted by an axicon of opening angle γ, forming a diamond shaped region (z_{max}), these rays propagate to pass through an identical axicon placed in the reverse direction at the z_{max} position. The second axicon collimates the refracted rays to form parallel plane waves forming a Gaussian beam at the far-field, as shown in Fig. 3.4.

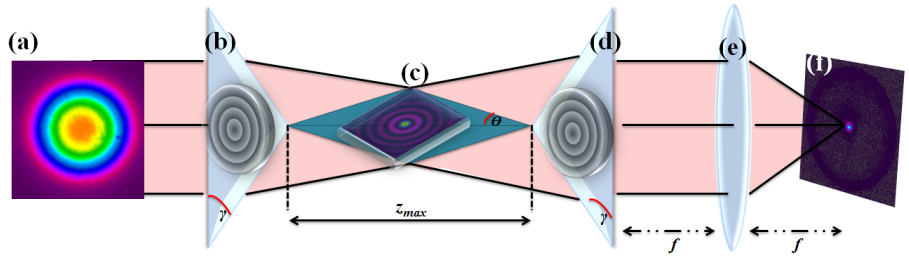

Figure 3.4: (a) A Gaussian beam illuminating (b) an axicon mask of $\ell = 0$, generating (c) a zeroth-order BG beam within the z_{max} region. This BG is incident on (d) an identical axicon hologram, such that at the Fourier plane of (e) a Gaussian on axis intensity is observed in (f).

This detection tool is k_r and ℓ specific, since if either k_r or ℓ are not matching, a pure Gaussian mode will not be formed at the Fourier plane. The transmission function defined for the detection hologram is that of a digital axicon in Eq. 2.20, with the change of sign:

$$t = \exp(ik_r r - i\ell\phi), \tag{3.9}$$

where the first exponential term represents the detection of the radial wave vector k_r, the second term represents an azimuthal filter. The detected signals are measured optically through the convolution process measurement observed at the Fourier plane of the lens:

$$g_{out} = F(E_{\ell}^{BG}) \otimes F(t), \tag{3.10}$$

where g_{out} is the output signal resulting from the convolution between the Fourier transform of the BG with the transformation function in Eq. 3.9. The Fourier transform of the transmission function results in an annular ring, and the angular spectrum of the BG mode also has the annular-ring shape, given that their radii are equal; their convolution will produce a bright spot with a Gaussian profile at the centre of the output plane as in Fig.3.5 (a). On the other hand if the ℓ or the k_r values of the BG mode are different from that of the transmission function in Eq. 3.9 of the SLM, there will be no on axis intensity as shown in Fig.3.5 (b) and (c) respectively.

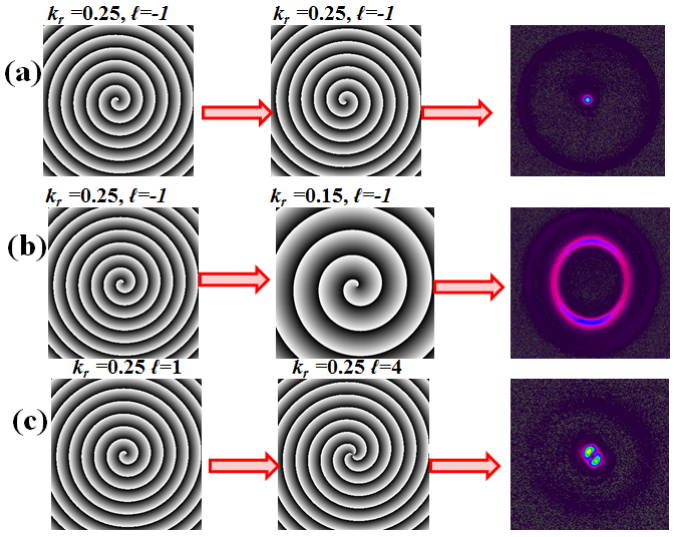

Figure 3.5: Detected signal images of (a) matching $k_r = 0.25$ rad/pixel and $\ell = 1$, (b) same $\ell = 1$ different k_r, and (c) digital axicons of same $k_r = 0.25$ rad/pixel and different ℓ.

3.2.1 Experimental methodology and results

An all digital experimental setup was used to extract the azimuthal and the radial components of the BG beams as shown in Fig. 3.6. In this setup a Gaussian beam was expanded using the telescope consisting of lenses L_1 (f_1=300 mm) and L_2 (f_2= 100 mm) to obtain a Gaussian size of ω_0=1 mm. The BG beams were generated using the first SLM (SLM 1) encoded with the digital axicon holograms. The resulting diffracted orders were filtered using the $4f$ imaging system selecting the order of interest. The second SLM (SLM 2) was fixed at the z_{max} position, while changing the position of the optical medium such as an obstruction and the turbulence plate within the z_{max} region. SLM 2 was used to scan through the radial and azimuthal components by changing its transmission function for various ℓ and k_r values, such that the effects of the perturbations on the BG beams propagating in free-space or through an optical medium could be studied. The resulting signals were Fourier transformed using lens L_5 to the CCD camera.

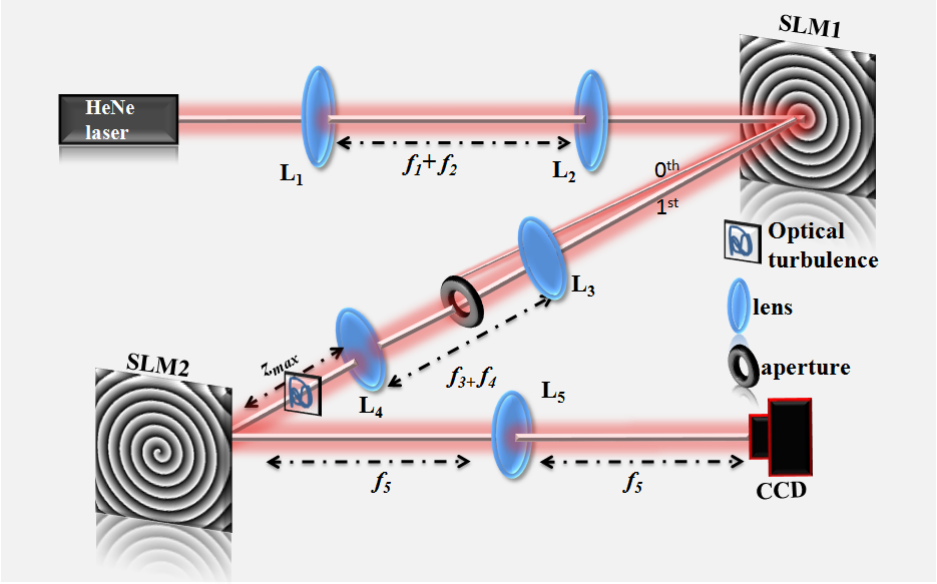

Figure 3.6: Schematic of the experimental setup for two-dimensional detection of BG beams using digital axicons.

As the BG is limited to z_{max}, the optimal position in which the second axicon is placed to obtain the optimal 2-dimensional detection was verified by placing the second axicon at different propagation distances within the z_{max} region. It was obtained to be at the z_{max} position as expected. This is seen in Fig.3.7 showing an accurate radial component detection of $k_r = 0.25$ rad/pixel at its corresponding $z_{max} = 84$ cm position. Since z_{max} is a function of

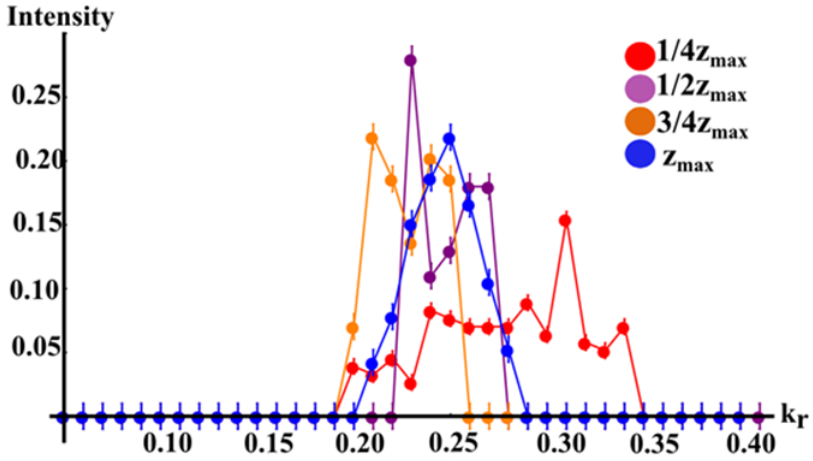

Figure 3.7: This graph shows that the optimal position to detect the BG beams using a digital axicon is at the z_{max} position.

k_r as shown in Eq. 2.18, this implies that there are different z_{max} positions for various k_r values, as a result we had to physically move the detection axicon to corresponding z_{max} position to obtain the k_r spectrum in Fig. 3.8 (a). We then chose a $k_r = 0.25$ rad/pixel to detect the azimuthal component as shown in Fig. 3.8 (b) at the $z_{max} = 84$ cm.

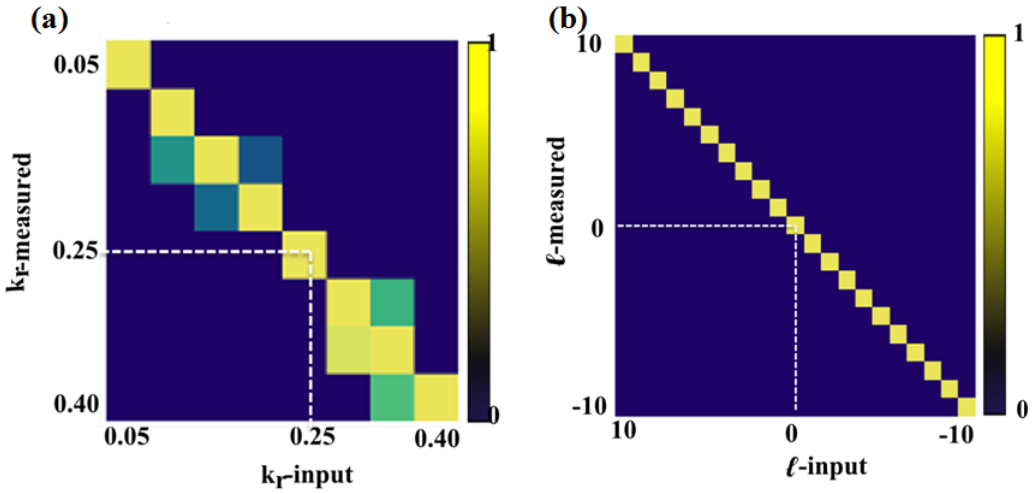

Figure 3.8: (a) Radial (k_r) decomposition of the BG modes at respective z_{max} positions for $\ell = 1$. (b) Azimuthal (ℓ) decomposition for $k_r = 0.25$ rad/pixel at $z_{max} = 84$ cm.

Optical turbulence

Optical turbulence arises from differences in refractive indices between points in the atmosphere, as a result when a laser beam propagates through the optical atmospheric turbulence it accumulates fluctuations in its phase and amplitude. We tested the efficiency of

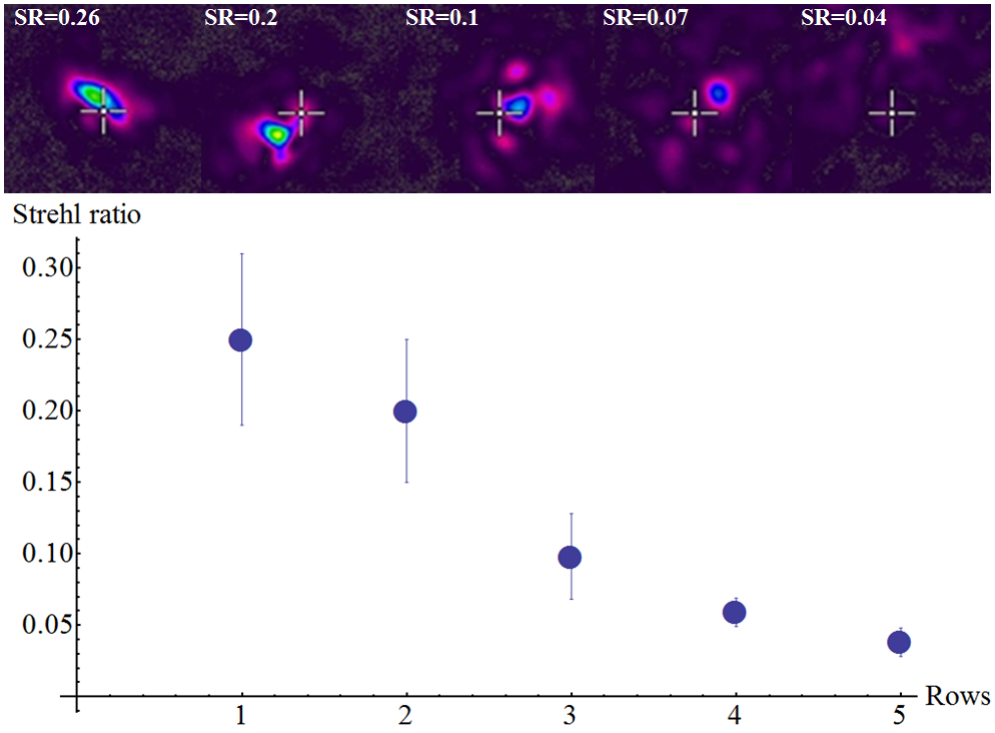

Figure 3.9: The graph of the Strehl ratio values on the different turbulence strengths of the plate, with the images showing the effect of turbulence on the Gaussian beam.

our detection tool, by detecting BG modes that have propagated through a turbulent medium defined by Kolmogorov turbulence [59]. The strength of the optical turbulence was characterized with the Strehl ratio (SR) [60], by taking the ratio between the an on axis intensity of an unperturbed beam with the intensity of the perturbed beam. The turbulence strength increases with decreasing SR as shown in Fig. 3.9. The turbulence plate was placed at $1/2z_{max}$ and the detector was placed at $z = z_{max}$. Two turbulence strengths were used corresponding to Strehl ratios of SR = 0.2 and SR = 0.03, and the turbulence introduced the tip and tilt effect on the modes, resulting in distorted phase and amplitude of the beams as shown in Fig. 3.10 (a). The spatial modes are strongly affected by turbulence, since their phase structure is given by $\exp(i\ell\phi)$, hence the distortion in the phase structure of the beam result in azimuthal coupling as shown by the results in Fig. 3.10 (b, c) for the different Strehl ratios, similarly the distortion in amplitude results in radial coupling 3.10 (d) [61]. These

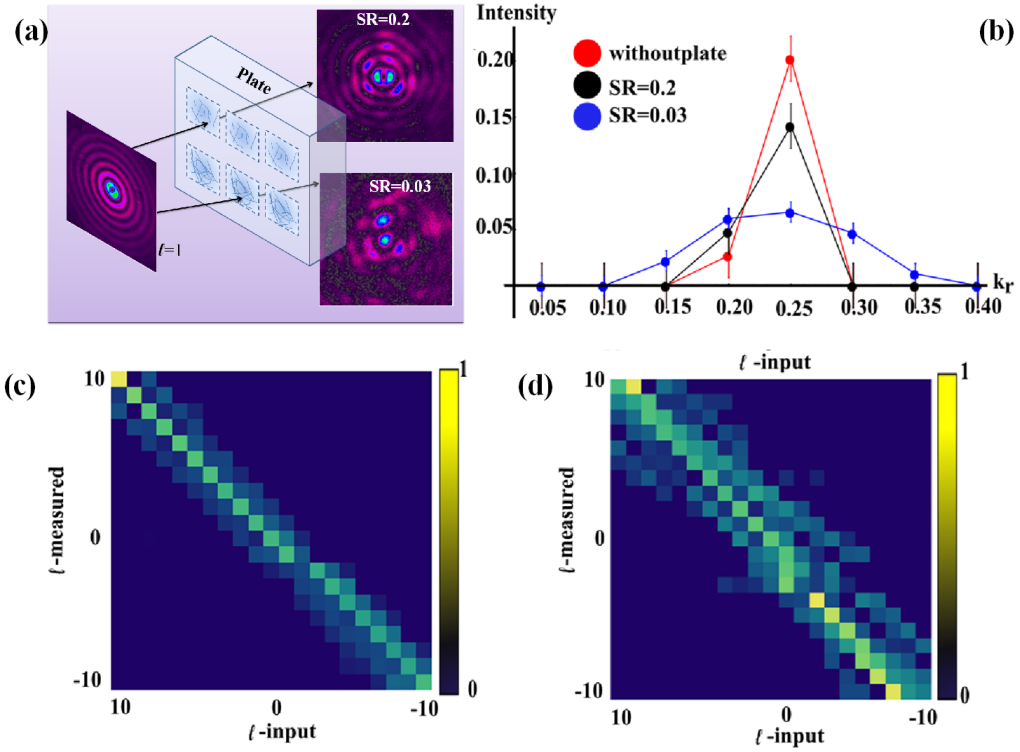

Figure 3.10: The BG beam of $\ell = 1$, $k_r = 0.25$ rad/pixel passing through (a) optical turbulence resulting in (b) the spread in k_r at different Strehl ratios, and a spread in the ℓ spectrum (c) at SR=0.2, and (d) at SR=0.03.

results serves to illustrate the versatility of our detection tool.

3.3 Summary

We have presented a versatile technique to experimentally realize the detection of Bessel beams using digital axicons programmed on a spatial light modulator. We have shown the ability to distinguish both the radial and azimuthal indices of such beams, a core requirement for optical communication protocols. In addition we have considered two applications of the tool and observed the modal changes to an incoming Bessel beam due to both amplitude and phase perturbations resulting from an opaque obstacle and a turbulence plate, respectively. The ability to modally resolve such fields will find uses in both quantum and classical studies.

Chapter 4

Generation and detection of vector Bessel-Gauss beams

4.1 Introduction

The beams that have been looked at in the previous chapters have homogeneous polarization, thus they are scalar fields. Beams of spatially varying polarisation are known as the vector beams. An example of such beams is the cylindrical vector (CV) beams that are cylindrically symmetric in polarization, such as the radially and azimuthally polarized light. These vector beams are a solution to the full wave equation Eq.1.6, and their peculiar feature under high numerical-aperture focusing has given interest to applications such as spectroscopy, microscopy, optical trapping, particle acceleration, and interferometry [62–64]. The spatially varying polarisation of the beam spans the entire Poincare sphere, this implies that any polarisation state can be represented by a linear combination of orthogonally polarized waves with different phases. For instance a vector vortex beam is a result of two orthogonal circular polarized helical beams, with their phase variations superimposed together. Mathametically this can be illustrated using the Jones vectors [65] for circularly polarized light:

$$\exp(i\ell\phi)\begin{pmatrix}1\\ i\end{pmatrix} + \exp(-i\ell\phi)\begin{pmatrix}1\\ -i\end{pmatrix} = \begin{pmatrix}\cos(\ell\phi)\\ \sin(\ell\phi)\end{pmatrix} \tag{4.1}$$

Equation 4.1 is the description of the radially polarized vector vortex beam. Previous methods of generating CV beams include the use of sub-wavelength gratings [66], polarization grating axicons [67], and interferometric techniques [68, 69]. We have used a geometrical phase element that introduces a phase shift known as the Pancharatnam-Berry (PB) phase on the incoming wave to generate CV beams. This geometric phase element is an azimuthally birefringent plate, which couples spin angular momentum (SAM) and OAM of light, with a PB phase geometry given by $\alpha = q\phi + \alpha_0$, where ϕ is the azimuthal angle in the xy-plane, q is an integer, and α_0 is a constant. This azimuthally birefringent element is known as the q-plate, it has birefringence retardation similar to that of half-wave plate, that converts a left-right (right-left) circular polarization, while introducing a phase shift (PB) of $\Delta\Phi = \pm 2q\phi$ [70], with the topological defect on the beam axis. This optical element is polarization controllable in that it shapes the phase of the input light depending on the input polarization. The Jones matrix formalism can be used to mathametically illustrate the effect of the q-plate for a linearly polarized input, for a half wave plate the Jones matrix [71] is given by

$$M' = \begin{pmatrix} 1 & 0 \\ 0 & -1 \end{pmatrix}. \tag{4.2}$$

The rotation of the Jones matrix M' by an angle α along the transverse plane will be given by matrix M:

$$\begin{aligned} M &= R(-\alpha)M'R(\alpha) \\ &= \begin{pmatrix} \cos\alpha & \sin\alpha \\ -\sin\alpha & \cos\alpha \end{pmatrix} \begin{pmatrix} 1 & 0 \\ 0 & -1 \end{pmatrix} \begin{pmatrix} \cos\alpha & -\sin\alpha \\ \sin\alpha & \cos\alpha \end{pmatrix} \\ &= \begin{pmatrix} \cos 2\alpha & \sin 2\alpha \\ \sin 2\alpha & -\cos 2\alpha \end{pmatrix}, \end{aligned} \tag{4.3}$$

where $R(\alpha)$ is a two-dimensional rotational matrix, and $\alpha = Q\phi = 2q\phi$, and Q is the azimuthal charge introduced by the q-plate:

$$M = \begin{pmatrix} \cos(Q\phi) & \sin(Q\phi) \\ \sin(Q\phi) & -\cos(Q\phi) \end{pmatrix}. \tag{4.4}$$

When a superposition of scalar non-diffractive BG beams, mathametically described as [72]

$$u(r, \phi, z = 0) = \sum_{\ell} J_{\ell}(k_r r) \exp(i\ell\phi) \begin{pmatrix} 1 \\ 1 \end{pmatrix} \tag{4.5}$$

passes through the q-plate Eq. 4.4:

$$\begin{pmatrix} cos(Q\phi) & sin(Q\phi) \\ sin(Q\phi) & -cos(Q\phi) \end{pmatrix} \begin{pmatrix} 1 \\ 1 \end{pmatrix} \exp(i\ell\phi) \;\; \rightarrow$$
$$\exp(i(\ell + Q)\phi) \begin{pmatrix} 1 \\ -i \end{pmatrix}$$
$$\exp(i(\ell - Q)\phi) \begin{pmatrix} 1 \\ -i \end{pmatrix}. \tag{4.6}$$

In bra-ket notation Eq. 4.6 becomes:

$$|\ell, L\rangle \rightarrow |\ell + Q, R\rangle\,, \tag{4.7}$$

and

$$|\ell, R\rangle \rightarrow |\ell - Q, L\rangle\,. \tag{4.8}$$

The left circular component is converted to a right-circular component, while increasing the azimuthal component by unit charge of OAM depending on the charge of the q-plate as shown in Eq. 4.6 and Eq. 4.7. The reverse is also true, the right-circular component is converted to left-circular polarization, decreasing the azimuthal component as shown in Eq. 4.6 and Eq. 4.8, for incoming OAM carrying mode with high efficiency. As a result, the

non-diffractive vector BG beams [74, 75] were generated, this was achieved through the experimental setup outlined in the next subsection.

4.2 Experimental methodology and results

The experimental realization of the generation of non-diffracting vector BG beams is shown below, where a HeNe laser beam of $\lambda = 633$ nm was expanded using lenses (L_1 and L_2) and directed onto SLM1, where the BG modes and their superpositions were generated by the spiral ring-slit. The scalar fields were observed at the Fourier plane of the lens (L3), where

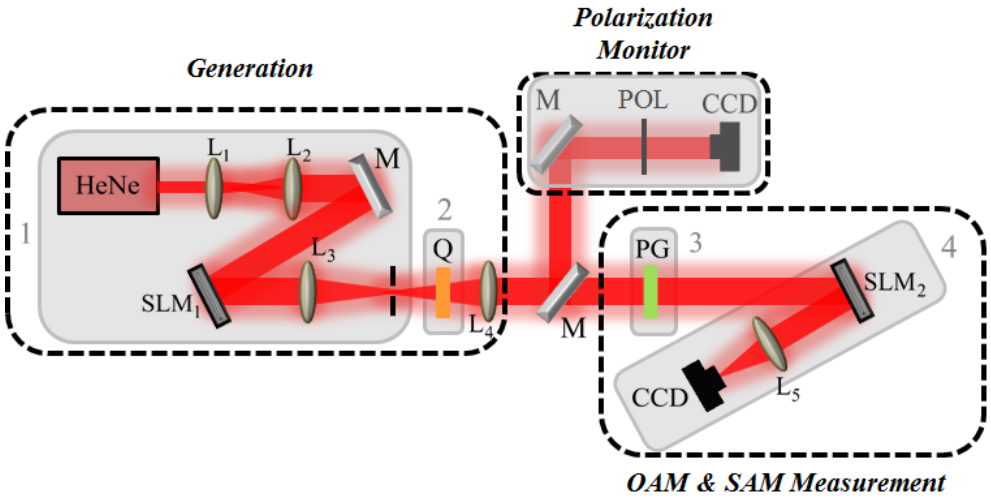

Figure 4.1: Schematic of the experimental setup divided into 4 divisions [division 1 and 2, scalar and vector generation respectively; division 3 and 4, vector and azimuthal decomposition respectively]. L, denotes the lens ($f_1 = 15$ mm, $f_2 = 150$ mm, f_3 and $f_4 = 500$ mm, $f_5 = 300$ mm); A, aperture; Q, q-plate; PG, polarization grating; CCD, camera.

they propagated to pass through the q-plate (Q) resulting in CV BG beams as indicated in the highlighted divisions 1 and 2. The highlighted divisions 3 and 4 represent the detection of these modes which will be explained in detail. The process of generating scalar BG beams and converting them to CV BG beams is shown in Fig. 4.2, where in Fig. 4.2 (a) a linearly polarized Gaussian beam with its polarization illustrated by the arrows pointing in the horizontal direction is incident on the SLM encoded by the spiral ring-slit of $\ell = 0$, resulting in a scalar zeroth order BG beam observed at the Fourier plane of the lens. The generated scalar field passed through the q-plate in highlighted division 2, which was placed some distance away from the Fourier plane of the SLM to form a radially polarized CV BG beam of $\ell \pm 1$ with its polarization illustrated by arrows pointing radially outward.

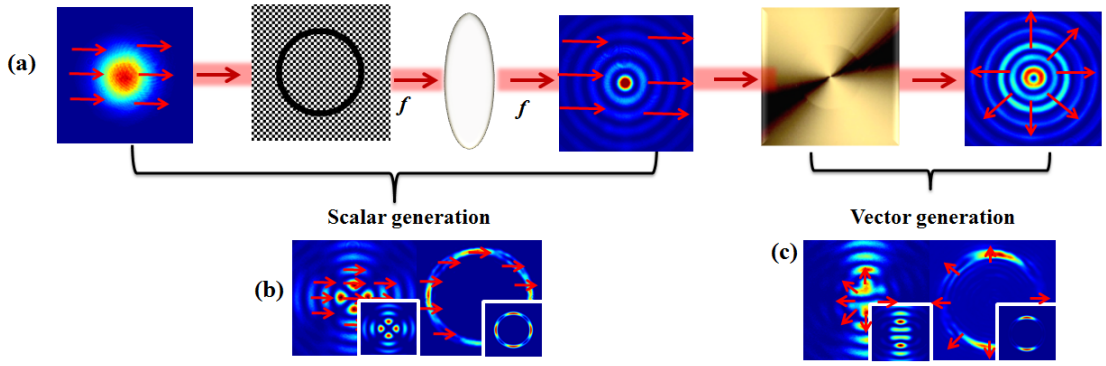

Figure 4.2: (a) The generation of scalar BG beams using a ring-slit hologram, converted in CV BG beams using a q-plate. The Superposition of (b) scalar BG, and (c) CV BG beams at the near and far-fields. With inserts showing their theory images.

4.2.1 Detection of vector BG beams

The vector BG beams consist of both SAM and OAM, hence there are different detection tools that need to be incorporated to detect these degrees of freedom. We employ a diffractive optical elements such as a polarization grating (PG) and digital holograms to perform an azimuthal (OAM detection) decomposition as explained in detail in the previous section . A

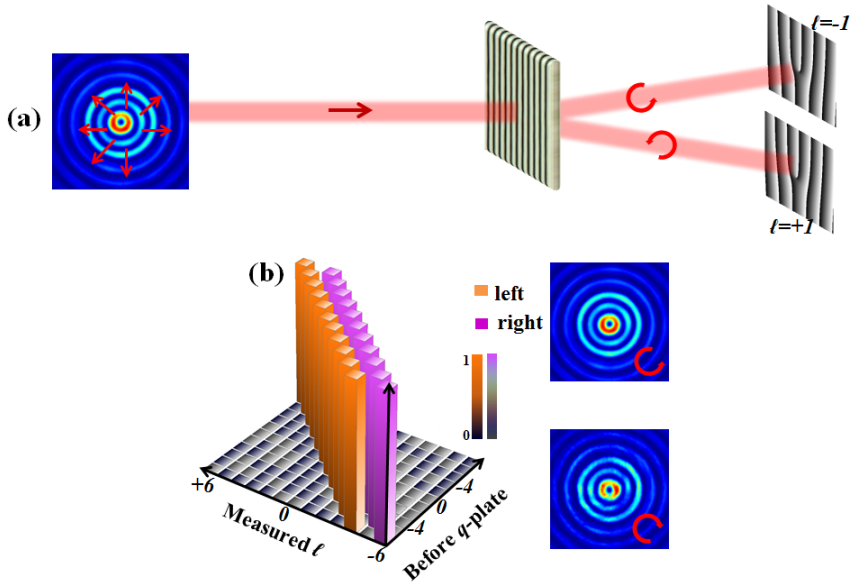

Figure 4.3: (a) Separation of the circularly polarized beam into right and left circular polarization states using a PG. Where the azimuthal detection is performed using the fork holograms resulting in (b) the azimuthal spectrum of the two polarization states.

PG of period 8.3 μm with its detailed manufacturing process outlined in [73], acts as a polarizing beam splitter for circularly polarized states. It was aligned approximately to separate the left- and right-circular polarization states such that the azimuthal detection of the modes was polarization dependent, where in Fig. 4.3 (a) a circular polarised vector BG

beam of $\ell = 1$ passed through a PG separating the left- and right-circular polarized beams, where the azimuthal filtering of these modes was done in the LG basis using forked holograms. As we have shown in Eq. 4.6 that the q-plate converts the left-circular polarized component of the scalar field into a vector beam of right-circular polarization, while increasing the azimuthal charge by $+Q$. Also the right-circular component of the scalar-field is converted to a left-circular vector field, with a decrease in the azimuthal charge by $-Q$. The detected results are shown in Fig. 4.3 (b) where the left-circular polarization states show a decrease in their OAM charge (pink), while the right-circular polarized states show an increase in their OAM charge (orange) as expected. In addition we illustrated that the

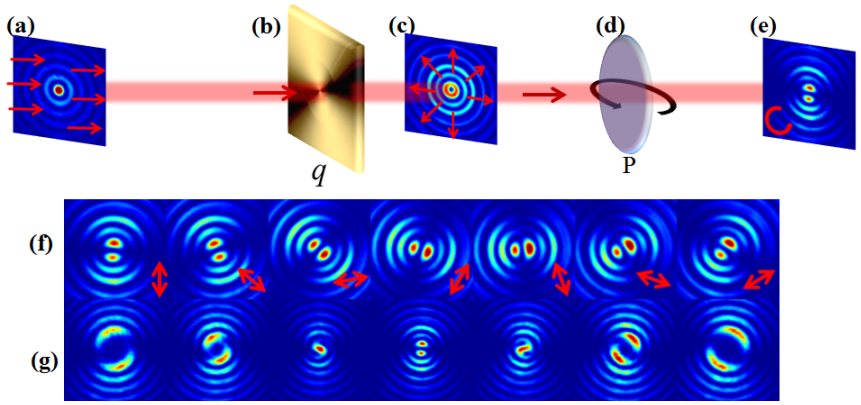

Figure 4.4: (a) The zeroth-order scalar BG beam of ℓ=0 was propagated through (b) the q-plate resulting in (c) a radially polarized CV BG beam of the superposition of $\ell = \pm 1$, passing through (d) a rotating polarizer, resulting in (e) a rotating vector BG beam. (f) Intensity profiles of vector BG of $\ell = 0$ recorded with a rotating polarizer. (g) Near-field intensity profiles of vector BG beams of $\ell = -5, -3, -1, 0, +1, +3$, and $\ell = +5$ recorded with a polarizer in front of the CCD camera.

intensity of the vector BG beam rotates, when placing a rotating polarizer after the q-plate as shown in Figs. 4.4 (a)-(e). The snap shots of the rotating vector BG mode of an initial scalar BG beam of ℓ=0 are shown in Fig. 4.4 (f).

4.3 Summary

Using the generation tools that we have outlined in the previous sections we have successfully transformed scalar BG beams into vector BG beams by adding a q-plate into our optical system. Using a polarization grating we were able to separate our modes into two polarization states and with azimuthal decomposition technique we were able to extract the amount of OAM carried by these vector BG beams.

Chapter 5

Entanglement of Bessel-Gauss beams

5.1 Introduction

The question whether quantum mechanics is a complete theory was stimulated by Einstein, Podolsky and Rosen's (EPR's) [76] thought experiment. In their thought experiment they focused on the spatially separated measurements of the physical properties of two particles (a and b) that had interacted in the past. Knowing the relative physical properties of these particles such as their position and the total momentum, they could measure the position or momentum (x_a, or p_a) of particle a, and instantaneously predict the position or the momentum (x_b, or p_b) of the second particle with certainty, without performing a measurement on it. However they could not simultaneously have the knowledge of both the position and momentum of one particle (x_a and p_a) with certainty, as stated by Heisenberg as the uncertainty principle [77]. They considered this a "spooky" action, but the ability to determine the position or the momentum state of particle b, by doing a measurement on particle a even though the two particles are spatially separated, implies that the two particles are entangled. This entanglement of quantum particles leads to the EPR paradox that quantum mechanics has either non-local interactions or that it was incomplete in that there are hidden variables that can describe the statistical physical quantum system. As a result, Bell and Clauser-Horne-Shimony-Holt (CHSH) described inequalities that gave a mathematical formulation of the local hidden variable theory. These inequalities are consistent with classical correlation and are violated for quantum correlations [78]. This gave a platform for the experimental realisation of quantum entanglement [79–82] which was first

demonstrated in the polarization states of entangled photons [79]. The high-dimensional entanglement of OAM states was demonstrated in 2001 by Mair. *et al* [14], and since then it has attracted attention to the OAM carrying beams to date [83–87]. The nature of quantum entanglement makes it attractive to certain applications such as quantum information computing [88–90], and quantum cryptography [91, 92].

5.2 Generating entangled photons

When a high frequency photon from a laser beam interacts with a non-linear crystal of χ^2, a non-linear process takes place. During this process the high frequency photon is converted into two lower frequency photons. This process is known as spontaneous parametric down conversion (SPDC) [93, 94], in this process the energy and momentum is conserved as shown in Fig. 5.1 such that the relationship between the three frequencies is given by:

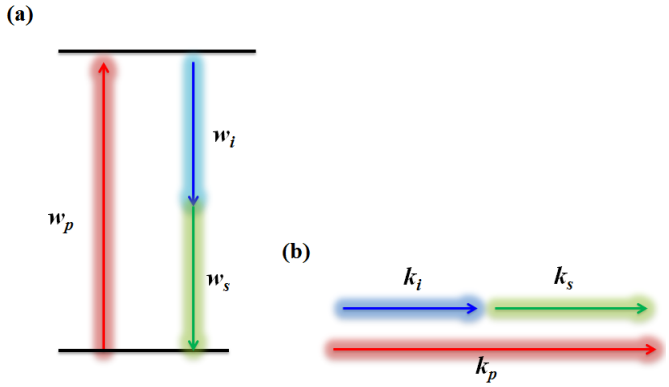

Figure 5.1: (a) SPDC process, with the energy conservation, and (b) linear momentum conservation.

$$\omega_p = \omega_i + \omega_s, \tag{5.1}$$

where ω_p, ω_i and ω_s are the pump, idler and signal frequencies respectively. The conservation of momentum is given by:

$$\vec{k_p} = \vec{k_i} + \vec{k_s}, \tag{5.2}$$

where k_p, k_i and k_s are the pump, idler and signal wave vectors. Similarly for helically phased beams the conservation of OAM during this process is stated as

$$\ell_p = \ell_i + \ell_s, \tag{5.3}$$

where ℓ_i and ℓ_s can take any integer values that sum up to give ℓ_p.
There are two types of SPDC type I and type II. In type I the down-converted photons are produced with the same polarisation, orthogonal to that of the pump. In type II one of the down-converted photons has the same polarization as the pump, while the other is in an orthogonal polarization state. Our experiment is based on type I, where the crystal was positioned to produce collinear, degenerate entangled photon pairs.

5.3 OAM entanglement

OAM entangled states can be ideally used to define an infinite dimensional discrete Hilbert space. The first OAM entanglement experimental realisation was demonstrated by Mair *et al.* [14], using helical beams in the LG basis. They showed that OAM is conserved during the SPDC process, and that the photon states can only be explained by quantum correlations, such that the OAM of the pair must sum to the OAM of the pump such that the two photon state for OAM can be written as

$$|\Psi\rangle = \sum_{\ell} a_{\ell,-\ell} |\ell\rangle| - \ell\rangle, \tag{5.4}$$

where $|a|^2$ is the probability of finding one photon in state $|\ell\rangle$, and the other in state $|-\ell\rangle$. Just like Heisenberg's uncertainty relation between the linear momentum and position, the conjugate variable of OAM is the angular position [**?**] which can be described by an aperture with angular width ϕ:

$$[\Delta(L)]^2[\Delta(\phi)]^2 \geq \frac{\hbar^2}{4}, \tag{5.5}$$

where $L = \ell\hbar$. This relationship can be used for further quantum entanglement test. The OAM entanglement can be measured in any angular harmonics basis with phase term $\exp(i\ell\phi)$ such as the LG basis [4, 14, 95], and BG basis [96, 97].

These sets of bases are similar in that they have helical wave front structure that gives rise to the OAM they carry; however they have different properties. For instance the BG beams have a unique property of being able to reconstruct themselves after encountering an obstruction. The entangled photon pairs tend to have weak interactions with each other, therefore their entanglement is fragile as they propagate through the transmission path such as a turbulent environment [98]. To some extent the properties associated with a particular measurement basis can offer an advantage in overcoming these transmission path limitations. A clear demonstration of this is shown in the next section, where the BG and LG beams were set to propagate through an optical obstruction of a particular size. Due to the properties associated with the BG basis, the OAM entanglement recovers while this was not observed in the LG basis.

5.4 Reconstruction of OAM entanglement

The decay of entanglement due to a perturbed transmission path has been demonstrated in different perturbation media such as the environmental noise [98–101], and the Kolmogorove turbulence [102–104]. Information processes based on ion-traps, nuclear magnetic resonance, and hyper-entanglement [105–107] have been used to eliminate de-coherence in quantum computers. The decay of OAM entanglement in spatial modes has been investigated and certain methods have been explored to limit the effects of turbulent environments. We show that by an appropriate choice of the entanglement measurement basis, such as the BG basis [97], OAM entanglement can be recovered after encountering an obstruction [40]. Using the self-reconstruction property of BG beams [27] to our advantage, we placed an obstacle of $D = 200\mu$m in the path of one of the down-converted photons and observed an obscured CHSH inequality in OAM entanglement due to the optical loss. We then measured the entanglement in both the BG and LG basis, the BG basis allowed the OAM entanglement to be recovered. The concurrence of the quantum state was dependent on the location of the shadow region in reference to the BBO crystal. As shown in the classical case as in chapter (2) where the azimuthal and radial spectra were recovered after a particular distance from the shadow region, the coincidence counts are recovered after the self-healing distance. On the other hand the LG basis could not recover the OAM entanglement. This test was done with

the experimental procedure outlined in the next section.

5.4.1 Experimental methodology and results

The experimental realisation of OAM entanglement can be separated into two parts as shown in Fig. 5.2. In highlighted section one, a mode locked ultraviolet (355 nm wavelength) laser of average power of 350 mW was used to pump a type I barium borate (BBO) crystal to produce 710 nm down-converted collinear entangled photon pairs through the SPDC process. To reflect the pump beam and transmit the down-converted light a bandpass filter was placed after the crystal, a circular obstruction of radius $D = 200$ μm was placed to obstruct photon pairs. The front plane of the crystal was imaged by L_1 and L_2 of focal lengths (f_1=200 mm, f=2 mm) respectively onto two separate SLMs. In highlighted section two, we set the photons to propagate at different paths separating them spatially. We then performed

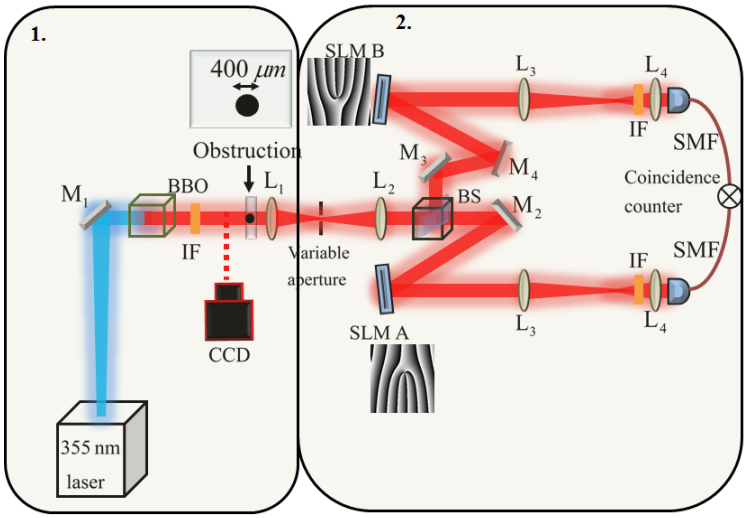

Figure 5.2: The schematic diagram of the experimental setup highlighted into two sections: 1. Generation of entangled photon pairs, and 2. measurement of the coincidence counts of the entangled pair of photons.

measurements on the photons, where the OAM filters (SLM with varying fork dislocations), were placed in the propagation paths of the entangled pairs and re-imaged by L_3 and L_4 of focal lengths (f_3=500 mm, f_4=2 mm) respectively. These SLMs were used to preform the modal decomposition technique, that resulted in a Gaussian signal indicating the detection of the OAM states of these photon pairs. This Gaussian signal was coupled into single mode fibres of mode-field diameter of $d = 4.6$ μm attached to avalanche photo diodes (APDs) that detect single photon pairs. The bandpass filters were also used to prevent any scattered pump

light from entering the fibres. Since these photon pairs propagate in different paths, they arrive at different times of limited interval known as the gating time. This implies that a coincidence count will only be recorded when photons arrive at the detectors within this time interval. This process takes place for a series of photon pairs resulting in a recorded coincidence count rate. The setup in Fig. 5.2 was first set in back-projection mode for alignment purposes, where the BBO crystal was replaced by a mirror, and a 710 nm diode laser was connected to the SMF in arm A, allowing light to propagate through the system in reverse. The SLMs were adjusted in such a way that their first diffracted order overlapped with the pump beam, such that the measured coincidences can be purely from the specified signal as the SLM reflects many diffracted orders. This optimisation process was done by using the OAM conservation to our advantage where, for a pump beam of $\ell_p = 0$, the coincidence counts are expected when $\ell_i + \ell_s = 0$. Hence, if a hologram of $\ell_i = 0$ is encoded on SLM A and $\ell_s = 1$ on SLM B, there will be no signal (coincidence counts). On the other hand, if $\ell_i = 3$ is encoded on SLM A and $\ell_s = -3$ is incident on SLM B there will be coincidence counts measured as shown in the plots in Fig. 5.3 (a). This was done by encoding each SLM with holograms ranging from $\ell = 20$ to $\ell = -20$ obtaining a spiral bandwidth. Not only do the SLMs efficiency play a role in the detected signals that show a decreasing trend from $\ell = 0$, but also the size of the helical modes increases with increasing azimuthal index ℓ, so this difference in the size of the modes contributes to how much power they can carry.

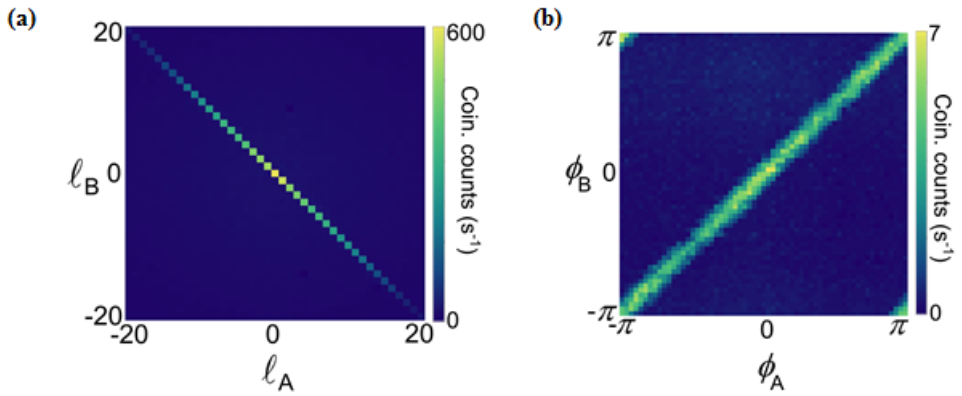

Figure 5.3: (a) Density plot of the measured coincidence counts, indicating the conservation of OAM in the diagonal entries. (b) Density plot of the coincidence counts per second using the angular holograms. Sample figure adapted from [86]

In a similar method, the angular spectrum in Fig. 5.3 (b) can be obtained, by encoding the SLMs with angular sector holograms with one of the holograms orientated at a particular

position, while rotating the other hologram. The process of back-projection allows the beam to be observed to check for the hologram alignment or for any diffractive element effects on the beam to be observed as in the case of the obstruction in Fig. 5.4, where the LG beam shows a distorted structure, while that of the BG beam is reconstructed after the self healing distance. As the obstruction is moved away from the crystal, the shadow region falls less onto

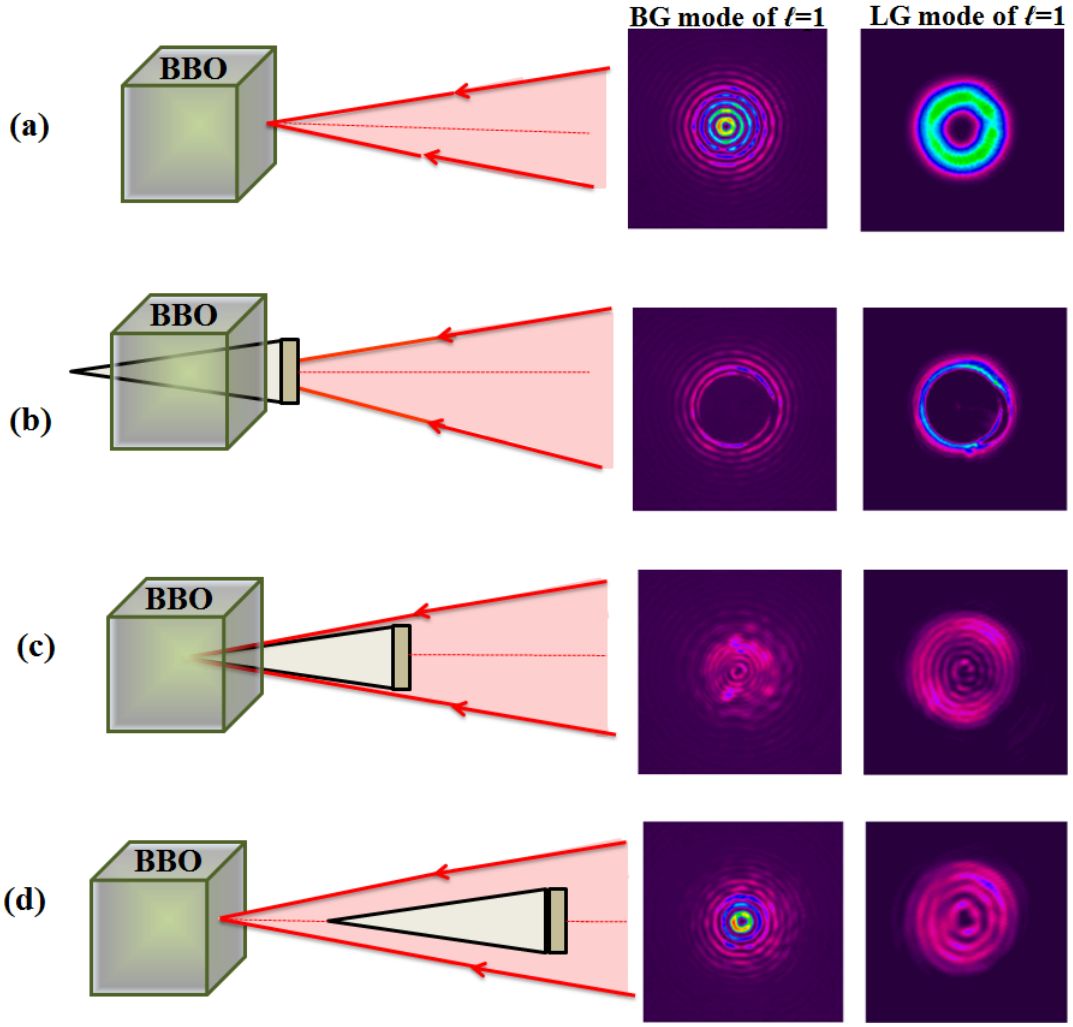

Figure 5.4: Back-projected obstructed BG and LG beams taken at different crystal planes, (a) without obstruction, with obstruction placed (b) at the plane of the crystal, (c) 20 mm away from crystal, (d) 50 mm away from the obstruction.

the crystal, until it no longer falls on the crystal as shown in Fig. 5.4 (d). The minimum self-healing distance of this BG beam is $z_{min} = 30$ mm for $R = 200$ μ m and it has fully reconstructed at the expected z_{min}. On the other hand the LG beam has no indication of restoration of its structure. The coincidence count rates of the BG and LG basis were measured for OAM state of $|\ell = \pm 2\rangle$. As the obstruction was moved away from the crystal in intervals of 5 mm the coincidence levels of the BG and LG basis were different in that when

the obstruction was at more than 25 mm distance from the crystal the BG showed an increase in the coincidence level, while the LG basis remained constant; this illustrates the unique self-healing property of the BG beams. The unobstructed coincidence count rate of the BG mode was $140/s$, and that of reconstructed BG mode was $80/s$, this may be due to the obstacle resulting in intensity loss. The effects of the obstacle on other quantum

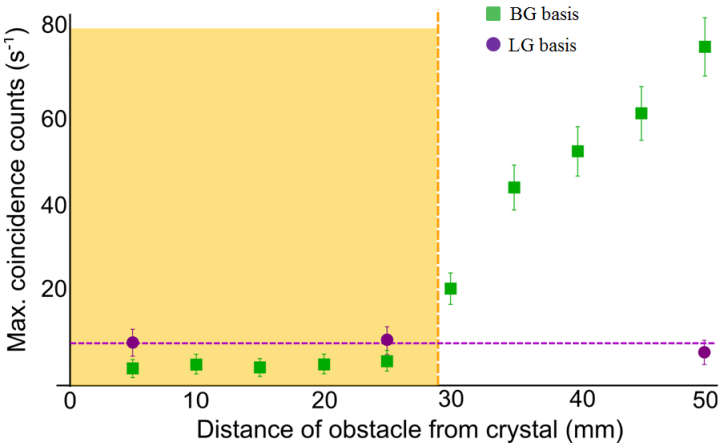

Figure 5.5: The effect of obstruction on the coincidence count rate of the BG and LG basis, indicating the reconstructed coincidence count rates in the BG mode.

measurements such as the degree of entanglement are not obtained from the recovery of coincidence count rate. To eliminate the possibility of hidden variables the violation of Bell's inequality was demonstrated by looking at the correlation of entangled photon pairs in superposition states, described as

$$|\Psi\rangle = \frac{1}{\sqrt{2}} \left(|\ell\rangle + \exp(i\theta) \, |-\ell\rangle \right), \tag{5.6}$$

where θ denotes the degree of rotation. For a particular ℓ value superposition holograms were generated for a range of angle θ, these holograms were both varied on SLM A and SLM B, where the hologram on SLM A was fixed at θ_A, and the one on SLM B was rotated at angle θ_B measuring the coincidence counts. A sinusoidal behaviour shown in Fig. 5.6 was observed, this can only be observed through quantum correlations in the OAM basis as shown in [95]. The Bell parameter S is given by:

$$S = E(\theta_A, \theta_B) - E(\theta_A, \theta'_B) + E(\theta'_A, \theta_B) + E(\theta'_A, \theta'_B), \tag{5.7}$$

where θ' is a different orientation from θ, and $E(\theta_A, \theta_B)$ is calculated from the measured

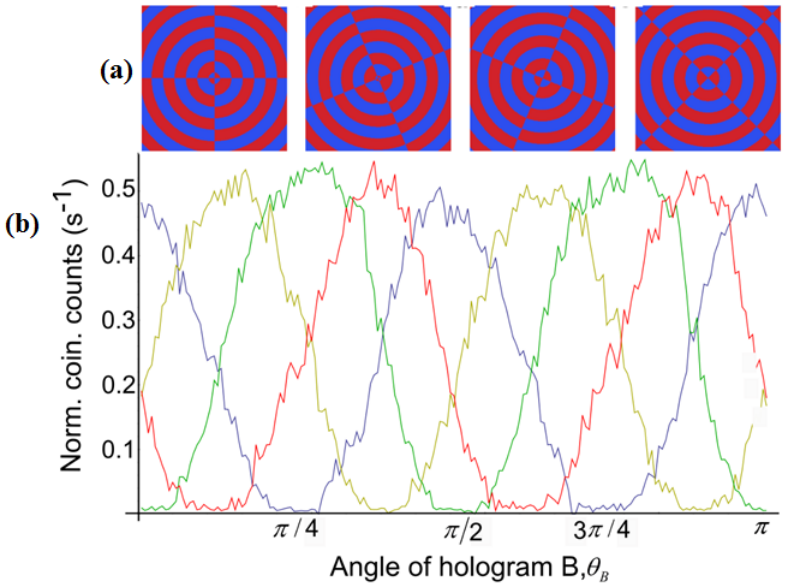

Figure 5.6: (a) The hologram on SLM A was oriented at four different angles: 0 rad (blue curve), $\pi/8$ rad (yellow curve), $\pi/4$ rad (green curve) and $3\pi/8$ rad (red curve). The typical sinusoidal Bell curve was measured with the obstruction placed in the propagation path at 45 mm from the crystal. Examples of the binary Bessel holograms ($|\pm 2\rangle$) used to perform a CHSH-inequality experiment are shown in the insets. (b) Normalized coincidence count rate as a function of the orientation of the hologram on SLM B.

coincidence counts at particular orientation. Bell's inequality is violated when $|S| > 2$. This bell-type inequality measurement was performed on the reconstructed state, where the obstruction was located at 45 mm from the crystal for quantum correlations. This was achieved by encoding the SLMs with superposition states of OAM and rotating them to record the coincidence count rates. These recorded coincidence counts were used to calculate the CHSH-Bell parameter $S = 2.78 \pm 0.04$, which is not far-off from the unobstructed value of $S = 2.79 \pm 0.03$; and shows a clear violation of the CHSH-Bell inequality as expected in quantum correlations. The statistical state of a quantum system such as the purity of the entangled state and the degree of entanglement, as well as the probability of finding the entangled pairs of photons in a particular quantum state; is described by the density matrix obtained by performing a state tomography on the system. This is achieved by determining the 2-dimensional density matrix:

$$\rho = \frac{1}{4}\sigma_0 \otimes \sigma_0 + \Sigma_{mn}\rho_{mn}\sigma_m \otimes \sigma_n, \tag{5.8}$$

where σ_k represents the Pauli matrices for $k = 0, 1, 2, 3, 4$. In matrix form , the qubit density matrix can be written as:

$$\rho = \begin{pmatrix} a_{11} & a_{12}e^{i\phi_{12}} & a_{13}e^{i\phi_{13}} & a_{14}e^{i\phi_{14}} \\ a_{12}e^{i\phi_{12}} & a_{22} & a_{23}e^{i\phi_{23}} & a_{24}e^{i\phi_{24}} \\ a_{13}e^{i\phi_{13}} & a_{22}e^{i\phi_{22}} & a_{33} & a_{34}e^{i\phi_{34}} \\ a_{14}e^{i\phi_{14}} & a_{24}e^{i\phi_{24}} & a_{34}e^{i\phi_{34}} & a_{44} \end{pmatrix}. \tag{5.9}$$

The phase and amplitude of the density matrix elements are denoted as ϕ_{ij} and a_{ij}

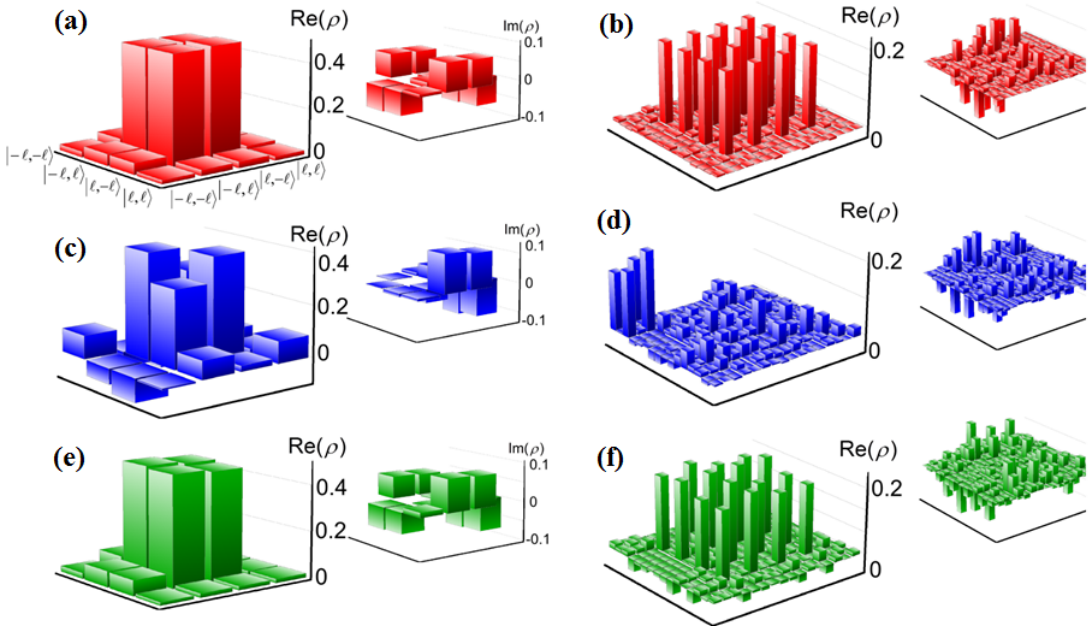

Figure 5.7: Reconstructed density matrices for dimensions $d = 2$, and $d = 4$ from full-state tomography measurements. Real and imaginary parts of the reconstructed density matrices for (a) and (b) no obstruction, (c) and (d) obstruction at 5 mm from the crystal, (e) and (f) obstruction at 45 mm from crystal.

respectively. The diagonal entries give the probability of detecting one photon in state $|\ell\rangle$ and the other in state $|-\ell\rangle$. The purity of these states is defined by linear entropy given by the trace of the density matrix $S_L = \frac{4}{3}(1 - Tr(\rho^2))$, when the trace is equal to zero then the system is a pure entangled state. The eigenvalues (λ) of the hermitian matrix $R \equiv \sqrt{\sqrt{\rho}\tilde{\rho}\sqrt{\rho}}$ can be used to evaluate the degree of entanglement denoted as concurrence $C(\rho) = \max(0, \lambda_1 - \lambda_2 - \lambda_3 - \lambda_4)$, for maximally entangled states the concurrence is one. In our case the density matrix from the reconstructed matrices of dimensions $d = 2$ for $|\ell = \pm 2\rangle$ in Fig. 5.7 (a,c,e), and $d = 4$ for $|\ell = -2, -1, 1, 2\rangle$ in Fig. 5.7 (b,d,f) were calculated.

There is a significant change in the density matrices when the obstruction is placed close to

the crystal, such that the shadow region fall onto it, soon after the minimum self-healing distance, the density matrix takes its unobstructed form as seen in the results.

5.5 OAM imaging

The illustration of quantum correlations between the OAM entangled photon pairs have been since achieved through ghost imaging, which was first observed more than 10 years ago by Pittman *et al.* [108]. In ghost imaging an object is placed at the signal beam, and the mobile detector at the idler beam. This mobile detector scans through the transverse plane of the idler beam to give coincidence counting rates, by combining information from two photon detectors; a single pixel (bucket) scanning detector with no spatial resolution, and a multi-pixel detector. An amplitude image of the object is observed [108, 109] as seen in Fig. 5.8. Holography has been recently used to enhance the contrast of the images within the a

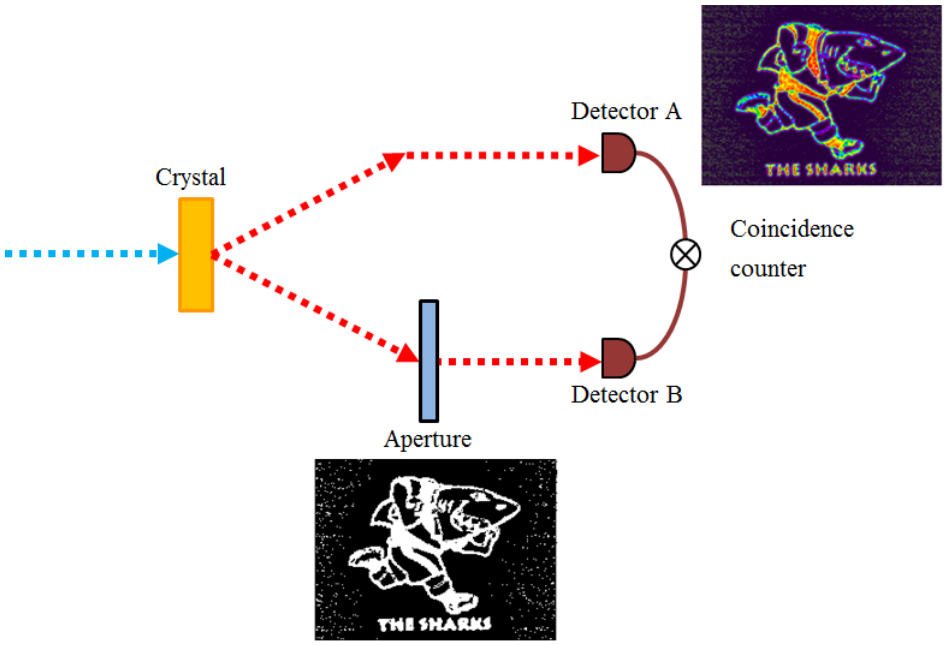

Figure 5.8: The ghost imaging setup using "The Sharks" aperture in the signal arm, and a scanning detector in the idler arm resulting in coincidence counts that give "The Sharks" image.

ghost imaging system [110], however there are uncertainties whether ghost imaging is solely a quantum phenomenon [111, 112], but this is not our interest of study. We show that we can, using digital holography, recover not only the phase, but also the amplitude of the object simultaneously. This is possible by using the spiral ring-slit hologram that varies radially and

azimuthally in the idler beam, provided that the object is symmetric and has an azimuthal component.

5.5.1 Concept

The task was to find a tool that can be used not only to give the amplitude of the object in arm A, but also to recover the phase of the object by correlating the detected signals from both arms. We know that for an arbitrary field $u(r, \theta)$ on a transverse plane that does not have global azimuthal modes, but localized points (vortices) in the field that possesses azimuthal components, we can extract these localized azimuthal components, by restricting the azimuthal mode to a set of radial coordinates as shown in Fig. 5.9 (a), with r-dependent coefficients. We can describe the full field distribution [17] as:

$$u(r, \theta) = \sum a_\ell(r) \exp(i\ell\theta), \tag{5.10}$$

where $a_\ell(r)$ is the r dependent coefficient, ℓ is the azimuthal index. We add an amplitude mask in Fig. 5.9 (b) which is simply an array of pixels that varies from 0 to pi, to this azimuthal ring, so that not only can we resolve the phase but also the amplitude of the generated field. The azimuthal ring in Fig. 5.9 (c) of thickness $\triangle$ selects the OAM state of light acting as a phase filter and the checker board as an amplitude filter.

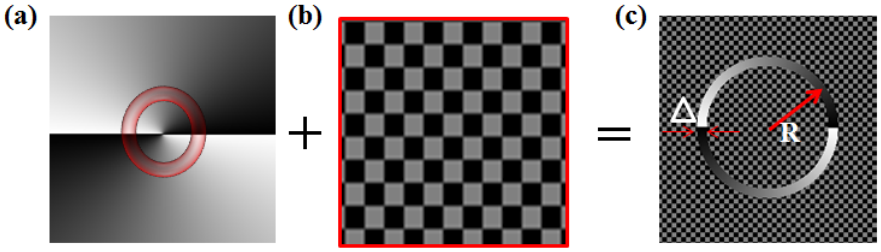

Figure 5.9: (a) Azimuthal ring restricting the azimuthal mode to a radial coordinate, (b) amplitude mask added to the restricted azimuthal mode, to yield (c) the spiral ring-slit of a particular thickness.

5.5.2 Experimental methodology and results

The same setup as in Fig.5.2 was used to conduct this experiment, but with no obstruction, and the same alignment procedure using back projection method was implemented. The following results were obtained in both the projected and down-converted mode. SLM A was encoded with the object hologram and SLM B was encoded with the spiral ring-slit of thickness D=0.08 mm scanning through the photons in the radial and azimuthal directions.

Back-projection results

The images of the generated object from SLM A, were recorded by placing a mirror before SLM B and a CCD camera at the plane of SLM B. During this back-projection mode SLM A was addressed with an azimuthal index of ℓ=-1 fork hologram generating an LG mode shown as an insert in Fig. 5.10(a) with its corresponding cross-sectional intensity profile. On SLM B we encoded a spiral ring-slit of ℓ=+1 and varied it radially and recorded the single count rates at detector B as a function of the radial position. Fig. 5.10 (b) shows this recorded

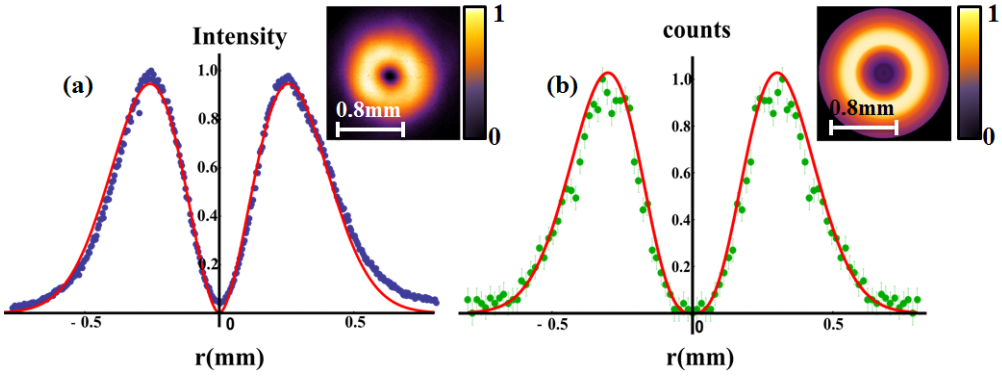

Figure 5.10: LG of ℓ=1 (a) intensity profile generated in SLM A, obtained from the cross-section of CCD image on insert, the corresponding (b) back-projected coincidence counts profile, with its image reconstructed from the counts.

count rate and it is clear that we recover the profile of an LG mode with its reconstructed field distribution shown in the insert. We then performed a similar experiment, but this time changed the object hologram on SLM A, by encoding a hologram with four different azimuthal indices each at different radii as in Fig. 5.11 (a). That is, the ℓ=0 in Fig. 5.11 (b) mode was encoded with an inner radius of 0 mm and an outer radius of 0.08 mm, while ℓ=5 Fig. 5.11 (c) was encoded with an inner radius of 0.08 mm and outer radius of 0.16 mm. Similarly ℓ=3 Fig. 5.11 (d) mode existed between r_{in}=0.16 mm to r_{out}=0.24 mm, and ℓ=1

Fig. 5.11 (e) existed between r_{in}=0.24 mm to r_{out}=0.32 mm. On SLM B we varied the azimuthal and radial components of the spiral ring-slit, that resulted in coincidence counts of recovered phase and amplitude of the azimuthal rings of light in Fig. 5.11(f).

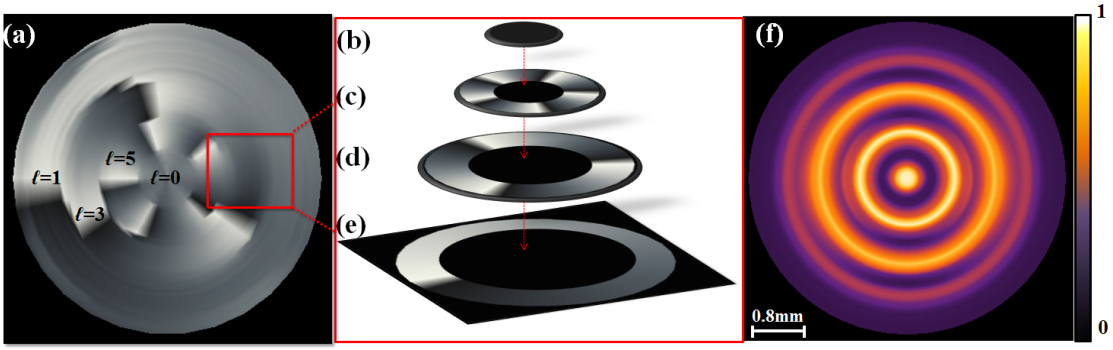

Figure 5.11: (a) The reconstructed digital holograms, from back projected counts of (b) ℓ=0, (c) ℓ=5, (d) ℓ=3, and (e) ℓ=1. (f) The reconstructed field of the rings of light.

Down-converted results

The setup in Fig. 5.2, was set to down converted mode generating entangled photon pairs that were projected into first the LG basis and then the BG basis, by encoding SLM A with appropriate holograms, the fork hologram and binary axicon [97], respectively. The measured

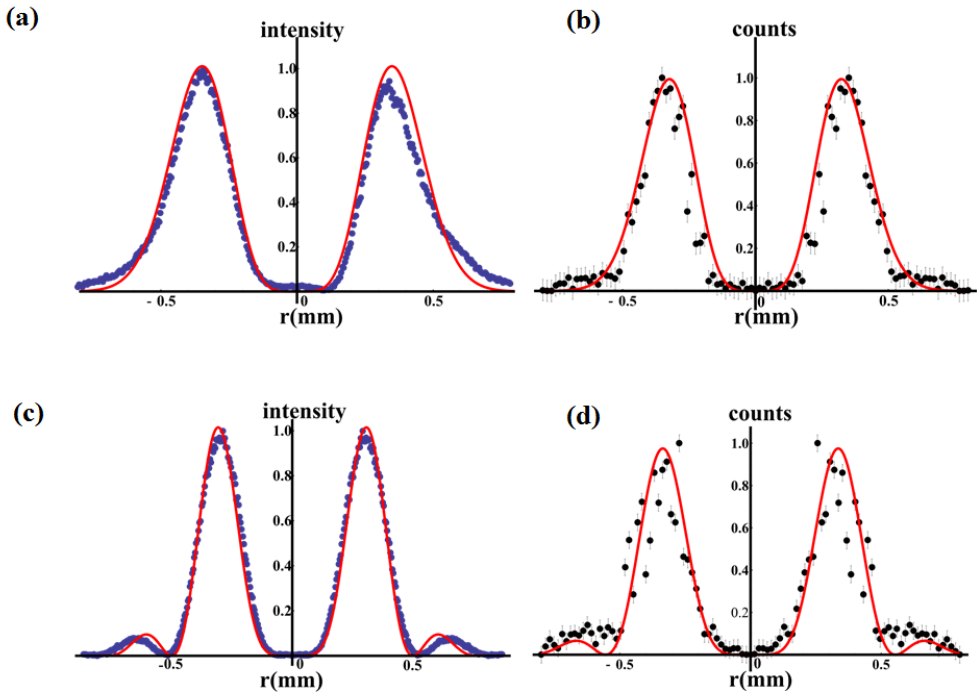

Figure 5.12: (a) Radial profile of LG of ℓ=3, from the CCD image, (b) its down-converted counts radial profile. (c) BG mode of ℓ=3 radial profile from CCD image,(d) its down-converted counts radial profile.

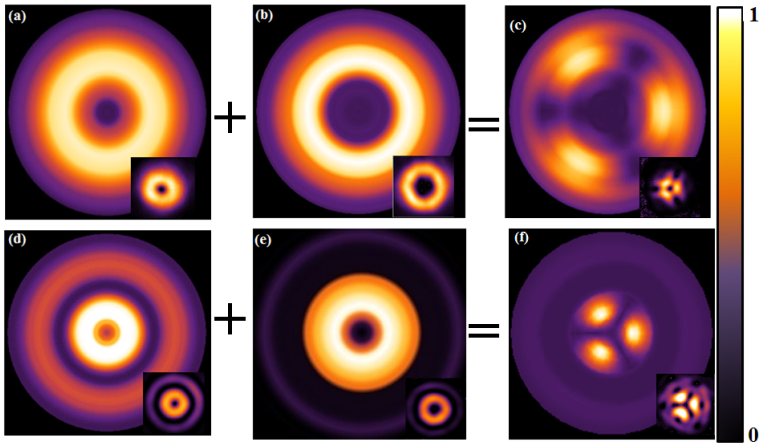

Figure 5.13: The superposition of LG of (a) ℓ=2 and (b) ℓ = -1 reconstructed down-converted counts images, similarly those of BG of (d) ℓ = -1 and (e) ℓ =2, resulting into a petal structures (c) and (f) respectively. The CCD images of these modes are shown in the inserts.

coincidence counts were plotted as a function of the radial position of the hologram on SLM B, and we successfully recovered the phase and amplitude of these angular harmonics as illustrated in Fig. 5.12.

Since these modes form a complete basis set we can generate their superposition by simply summing their transmission functions together, which can be implemented through digital holography [53]. We generated superposition of these modes in SLM A, and by varying the spiral ring-slit we detected the down-converted counts simultaneously recovering the phase and amplitude of these fields. The recovered fields were correlated with the CCD images in the insert of Fig. 5.13, to yield a correlation value of ≈ 0.9.

5.6 Summary

We have further explored the properties of BG modes in OAM quantum entanglement, where we have shown that the BG modes not only produce a wider spectrum in entanglement as reported previously; but they can also reconstruct entanglement after encountering an obstruction. Using one of our BG generation hologram, the spiral ring-slit, and the modal decomposition technique, we have successfully shown that we can simultaneously recover the phase and amplitude of any arbitrary field that forms a complete basis set, in a ghost imaging setup using a digital spiral ring-slit. This is a unique technique as it differs from the traditional ghost imaging that requires a scanning detector to only recover the amplitude of the field.

Chapter 6

Future Work

6.1 Conclusion

In chapter1 we have shown how the Maxwell's wave equation results in the Helmholtz scalar equation through the separation of variables of the electric field. We showed how the Gaussian mode forms part of the solution to the Helmholtz scalar equation for a plane wave modulated by a complex amplitude, were we also studied the propagation properties of the Gaussian field. This Gaussian function describes the intensity distribution of the output laser beam of commercial lasers. We have also indicated that the cylindrical solution to the equation results in the LG function that has an azimuthal dependence that gives rise to the OAM the LG beams carry, this OAM has opened room for various applications, such as in optical communication.

We then introduced a diffraction free solution to the Helmholtz equation in Chapter 2, known as the BG beams, and we outlined their propagation properties such as their diffraction-free and self-healing properties. We also investigated the tools that can be used to generate these BG beams such as conical lens, which is very sensitive to alignment and only suitable to generate a zeroth order BG beam of a particular ring spacing. Using a SLM we have shown that we can create digital axicons, by defining the transmission functions of the diffractive optic we wish to replace, to generate any desired BG and vortex modes. This was achieved by simply reflecting the Gaussian beam off the SLM encoded with an appropriate transmission function hologram, and observing the generated output field at screen.

Not only did we successfully illustrated the generation of the BG modes, we have presented a

versatile technique to experimentally realize the detection of Bessel beams using digital axicons programmed on a SLM in Chapter 3. We have shown the ability to distinguish both the radial and azimuthal indices of such beams, a core requirement for optical communication protocols. In addition we have considered two possible applications for our detection tool and where it was used to observe the modal changes to an incoming Bessel beam due to both amplitude and phase perturbations resulting from an opaque obstacle and Kolmogorov turbulence, respectively. The ability to modally resolve such fields will find uses in both quantum and classical studies.

We then added another degree of freedom to these BG beams by generating CV BG beams in Chapter 4, where the generation tools that we have outlined in the previous chapters were used and as a result, we successfully transformed scalar BG beams into vector BG beams by adding a q-plate into our optical system. Using a polarization grating we were able to separate our modes into two polarization states and with azimuthal decomposition technique we were able to extract the amount of OAM carried by these vector BG beams.

The self-healing property of the BG beams is not only useful in a classical system, where it is important for the simultaneous manipulation of micro-particles. In chapter 5 we have shown that this property of BG beams is important for the recovery of OAM entanglement after encountering an obstruction. We compared it with the LG modes and as it turns out the BG modes not only provide a broad spectrum for quantum experiments, but also recovers OAM entanglement. The spiral ring-slit that is used to generate the BG beams at the far-field has shown to be useful in single pixel imaging at the single photon level. This shows that our tools of creating these modes are versatile and they can be incorporated for a different applications.

6.2 Future work

Optical networks form a foundation of modern communications networks since the replacement of copper wires with optical fibres in the 1980s. This fibre technology has been based on single mode fibres (SMF), and due to the increasing demand in data transmission by a factor of approximately 10 every four years [38] as a result of the digital world we live in, the available capacity of the SMF will be limited in the near future. This limit in capacity is based on the Shannon capacity for non-linear fibre channels [38], where the SMF cannot carry

more than 100 Tbits s^{-1} of data. Optical transmission through SMF has been achieved through other optical properties of light, the dimension that has not yet been explored to transmit data is space.

Spatial modes such as the Laguerre-Gauss (LG) modes [20], have been studied as potential solutions to increase the bandwidth for optical communication through the process of mode division multiplexing (MDM) [13, 15, 16], which is based on using the LG modes as independent information carriers through SMFs, as they carry orbital angular momentum (OAM) [4] which is an unbounded degree of freedom. As we have shown that the generation tools of the helical modes that we have introduced can be used to detect any complete and orthogonal basis, for instance we can use fork diffraction grating for the azimuthal detection of the vector BG beams and that we can use the spiral ring-slit that we have used to generate the BG beams for single pixel imaging of LG basis and the azimuthally varying rings. For future studies we would like to characterize optical fibres for SDM, so that we can couple these LG modes into the fibre and implement our detection methods to extract the information carried by these modes. Our investigation is based on whether we efficiently multiplex and couple these modes into a fibre, and also demultiplex them using the methods that we have implemented and presented in our free-space optical communication experiments.

Bibliography

[1] Teich, M. C., and Saleh, B. E. A. "Fundamentals of photonics". Canada, Wiley Interscience, **3**, (1991).

[2] Griffiths, D. J., and Reed College."Introduction to electrodynamics" Upper Saddle River, NJ: Prentice hall. **3**, (1999).

[3] Andrews, David L.,"Structured light and its applications: An introduction to phase-structured beams and nanoscale optical forces," Academic Press, (2011).

[4] Yao, A. M., and Padgett, M. J., "Orbital angular momentum: origins, behavior and applications," Advances in Optics and Photonics, **3**(2), 161-204 (2011).

[5] Allen, L., Beijersbergen, M. W., Spreeuw, R. J. C., and Woerdman, J. P., "Orbital angular momentum of light and the transformation of Laguerre-Gaussian laser modes," Physical Review A, **45**(11), 8185 (1992).

[6] Beijersbergen, M. W., Allen, L., Van der Veen, H. E. L. O., and Woerdman, J. P., "Astigmatic laser mode converters and transfer of orbital angular momentum," Optics Communications, **96**(1), 123-132 (1993).

[7] Padgett, M. J., and Allen, L., "The Poynting vector in Laguerre-Gaussian laser modes," Optics Communications, **121**(1), 36-40 (1995).

[8] Padgett, M., and Bowman, R., "Tweezers with a twist," Nature Photonics, **5**(6), 343-348 (2011).

[9] Djordjevic, I. B., "Deep-space and near-Earth optical communications by coded orbital angular momentum (OAM) modulation," Optics Express, **19**(15), 14277-14289 (2011).

[10] Djordjevic, I. B., and Arabaci, M., "LDPC-coded orbital angular momentum (OAM) modulation for free-space optical communication," Optics Express, **18**(24), 24722-24728 (2010).

[11] Su, T., Scott, R. P., Djordjevic, S. S., Fontaine, N. K., Geisler, D. J., Cai, X., and Yoo, S. J., "Demonstration of free space coherent optical communication using integrated silicon photonic orbital angular momentum devices," Optics Express, **20**(9), 9396-9402 (2012).

[12] Krenn, M., Fickler, R., Fink, M., Handsteiner, J., Malik, M., Scheidl, T., and Zeilinger, A., "Communication with spatially modulated light through turbulent air across Vienna," New Journal of Physics, **16**(11), 113028 (2014).

[13] Gibson, G., Courtial, J., Padgett, M., Vasnetsov, M., Pas' ko, V., Barnett, S., and Franke-Arnold, S., "Free-space information transfer using light beams carrying orbital angular momentum," Optics Express, **12**(22), 5448-5456 (2004).

[14] Mair, A., Vaziri, A., Weihs, G., and Zeilinger, A., "Entanglement of the orbital angular momentum states of photons," Nature, **412**(6844), 313-316 (2001).

[15] Bouchal, Z., and Celechovský, R., "Mixed vortex states of light as information carriers," New Journal of Physics, **6**(1), 131 (2004).

[16] Bozinovic, N., Yue, Y., Ren, Y., Tur, M., Kristensen, P., Huang, H., and Ramachandran, S., "Terabit-scale orbital angular momentum mode division multiplexing in fibers," Science, **340**(6140), 1545-1548 (2013).

[17] Litvin, I. A., Dudley, A., Roux, F. S., and Forbes, A., "Azimuthal decomposition with digital holograms," Optics Express, **20**(10), 10996-11004 (2012).

[18] Schulze, C., Ngcobo, S., Duparré, M., and Forbes, A., "Modal decomposition without a priori scale information," Optics Express, **20**(25), 27866-27873 (2012).

[19] Schulze, C., Dudley, A., Flamm, D., Duparré, M., and Forbes, A., "Measurement of the orbital angular momentum density of light by modal decomposition," New Journal of Physics, **15**(7), 073025 (2013).

[20] Padgett, M., and Allen, L., "Light with a twist in its tail," Contemporary Physics, **41**(5), 275-285 (2000).

[21] Lavery, M. P., Berkhout, G. C., Courtial, J., and Padgett, M. J., "Measurement of the light orbital angular momentum spectrum using an optical geometric transformation," Journal of Optics, **13**(6), 064006 (2011).

[22] Berkhout, G. C., Lavery, M. P., Courtial, J., Beijersbergen, M. W., and Padgett, M. J., "Efficient sorting of orbital angular momentum states of light," Physical Review Letters, **105**(15), 153601 (2010).

[23] Leach, J., Padgett, M. J., Barnett, S. M., Franke-Arnold, S., and Courtial, J., "Measuring the orbital angular momentum of a single photon," Physical Review Letters, **88**(25), 257901 (2002).

[24] Leach, J., Courtial, J., Skeldon, K., Barnett, S. M., Franke-Arnold, S., and Padgett, M. J., "Interferometric methods to measure orbital and spin, or the total angular momentum of a single photon," Physical Review Letters, **92**(1), 013601 (2004).

[25] Bandres, M. A., and Gutiérrez-Vega, J., "Ince gaussian beams," Optics Letters, **29**(2), 144-146 (2004).

[26] Bandres, M. A., and Gutiérrez-Vega, J. C., "Elliptical beams," Optics Express, **16**(25), 21087-21092 (2008).

[27] McGloin, D., and Dholakia, K., "Bessel beams: diffraction in a new light," Contemporary Physics, **46**(1), 15-28 (2005).

[28] Durnin, J., "Exact solutions for nondiffracting beams. I. The scalar theory," JOSA A, **4**(4), 651-654 (1987).

[29] Durnin, J., Miceli Jr, J. J., and Eberly, J. H., "Diffraction-free beams," Physical Review Letters, **58**(15), 1499 (1987).

[30] Gori, F., Guattari, G., and Padovani, C., "Bessel-Gauss beams," Optics Communications, **64**(6), 491-495 (1987).

[31] Khonina, S. N., Kotlyar, V. V., Skidanov, R. V., Soifer, V. A., Jefimovs, K., Simonen, J., and Turunen, J., "Rotation of microparticles with Bessel beams generated by diffractive elements," Journal of Modern Optics, **51**(14), 2167-2184 (2004).

[32] Arlt, J., Garces-Chavez, V., Sibbett, W., and Dholakia, K., "Optical micromanipulation using a Bessel light beam," Optics Communications, **197**(4), 239-245 (2001).

[33] Litvin, I. A., McLaren, M. G., and Forbes, A., "A conical wave approach to calculating Bessel–Gauss beam reconstruction after complex obstacles," Optics Communications, **282**(6), 1078-1082 (2009).

[34] Garces-Chavez, V., McGloin, D., Melville, H., Sibbett, W., and Dholakia, K., "Simultaneous micromanipulation in multiple planes using a self-reconstructing light beam," Nature, **419**(6903), 145-147(2002).

[35] Grillo, V., Karimi, E., Gazzadi, G. C., Frabboni, S., Dennis, M. R., and Boyd, R. W., "Generation of Nondiffracting Electron Bessel Beams," Physical Review X, **4**(1), 011013 (2014).

[36] Volke-Sepulveda, K., Garcés-Chávez, V., Chávez-Cerda, S., Arlt, J., and Dholakia, K., "Orbital angular momentum of a high-order Bessel light beam," Journal of Optics B: Quantum and Semiclassical Optics, **4**(2), S82 (2002).

[37] Garces-Chavez, V., McGloin, D., Padgett, M. J., Dultz, W., Schmitzer, H., and Dholakia, K., "Observation of the transfer of the local angular momentum density of a multiringed light beam to an optically trapped particle," Physical Review Letters, **91**(9), 093602 (2003).

[38] Richardson, D. J., Fini, J. M., and Nelson, L. E., "Space-division multiplexing in optical fibres," Nature Photonics, **7**(5), 354-362 (2013).

[39] Bouchal, Z., Wagner, J., and Chlup, M., "Self-reconstruction of a distorted nondiffracting beam," Optics Communications, **151**(4), 207-211 (1998).

[40] McLaren, M., Mhlanga, T., Padgett, M. J., Roux, F. S., and Forbes, A., "Self-healing of quantum entanglement after an obstruction," Nature communications, **5**(3248) (2014).

[41] Lavery, M. P., Robertson, D. J., Berkhout, G. C., Love, G. D., Padgett, M. J., and Courtial, J., "Refractive elements for the measurement of the orbital angular momentum of a single photon," Optics Express, **20**(3), 2110-2115 (2012).

[42] Mourka, A., Mazilu, M., Wright, E. M., and Dholakia, K., "Modal Characterization using Principal Component Analysis: application to Bessel, higher-order Gaussian beams and their superposition," Scientific Reports, **3**(1422), (2013).

[43] Mazilu, M., Mourka, A., Vettenburg, T., Wright, E. M., and Dholakia, K., "Simultaneous determination of the constituent azimuthal and radial mode indices for light fields possessing orbital angular momentum," Applied Physics Letters, **100**(23), 231115 (2012).

[44] Arlt, J., and Dholakia, K., "Generation of high-order Bessel beams by use of an axicon," Optics Communications, **177**(1), 297-301 (2000).

[45] Brzobohatý, O., Cižmár, T., and Zemánek, P., "High quality quasi-Bessel beam generated by round-tip axicon," Optics Express, **16**(17), 12688-12700 (2008).

[46] Monk, S., Arlt, J., Robertson, D. A., Courtial, J., and Padgett, M. J., "The generation of Bessel beams at millimetre-wave frequencies by use of an axicon," Optics Communications, **170**(4), 213-215 (1999).

[47] Scott, G., and McArdle, N., "Efficient generation of nearly diffraction-free beams using an axicon," Optical Engineering, **31**(12), 2640-2643 (1992).

[48] Leach, J., Gibson, G. M., Padgett, M. J., Esposito, E., McConnell, G., Wright, A. J., and Girkin, J. M., "Generation of achromatic Bessel beams using a compensated spatial light modulator," Optics Express, **14**(12), 5581-5587 (2006).

[49] Chattrapiban, N., Rogers, E. A., Cofield, D., Hill III, W. T., and Roy, R., "Generation of nondiffracting Bessel beams by use of a spatial light modulator," Optics Letters, **28**(22), 2183-2185 (2003).

[50] Vasara, A., Turunen, J., and Friberg, A. T., "Realization of general nondiffracting beams with computer-generated holograms," JOSA A, **6**(11), 1748-1754 (1989).

[51] Turunen, J., Vasara, A., and Friberg, A. T., "Holographic generation of diffraction-free beams," Applied Optics, **27**(19), 3959-3962 (1988).

[52] McLeod, J. H., "The axicon: a new type of optical element," JOSA, **44**(8), 592-597 (1954).

[53] Vasilyeu, R., Dudley, A., Khilo, N., and Forbes, A., "Generating superpositions of higher–order Bessel beams," Optics Express, **17**(26), 23389-23395 (2009).

[54] Dudley, A., "Superpositions of light fields carrying orbital angular momentum," Doctoral dissertation, (2012).

[55] Arrizón, V., Ruiz, U., Carrada, R., and González, L. A., "Pixelated phase computer holograms for the accurate encoding of scalar complex fields," JOSA A, **24**(11), 3500-3507 (2007).

[56] Mhlanga, T., Trichilli, A., Dudley, A., Naidoo, D., Zghal, M., and Forbes, A., "Digital holograms for laser mode multiplexing," Proc. of SPIE, 91941B (2014).

[57] Dudley, A., Lavery, M., Padgett, M., and Forbes, A., "Unraveling Bessel beams," Optics and Photonics News, **24**(6), 22-29 (2013).

[58] Dudley, A., Mhlanga, T., Lavery, M., McDonald, A., Roux, F. S., Padgett, M., and Forbes, A., "Efficient sorting of Bessel beams," Optics Express, **21**(1), 165-171 (2013).

[59] Nelson, W., Palastro, J. P., Davis, C. C., and Sprangle, P., "Propagation of Bessel and Airy beams through atmospheric turbulence," JOSA A, **31**(3), 603-609 (2014).

[60] Janssen, A. J., van Haver, S., Dirksen, P., and Braat, J. J., "Zernike representation and Strehl ratio of optical systems with variable numerical aperture," Journal of Modern Optics, **55**(7), 1127-1157 (2008).

[61] Trichili, A., Mhlanga, T., Ismail, Y., Roux, F., McLaren, M., Zghal, M., and Forbes, A. "Detection of Bessel beams with digital axicons," Optics Express, **22**(14), 17533-17560 (2014).

[62] Youngworth, K., and Brown, T., "Focusing of high numerical aperture cylindrical-vector beams," Optics Express, **7**(2), 77-87 (2000).

[63] Kozawa, Y., and Sato, S., "Optical trapping of micrometer-sized dielectric particles by cylindrical vector beams," Optics Express, **18**(10), 10828-10833 (2010).

[64] Roxworthy, B. J., and Toussaint Jr, K. C., "Optical trapping with π-phase cylindrical vector beams," New Journal of Physics, **12**(7), 073012 (2010).

[65] Li, Y., Dudley, A., Mhlanga, T., Escuti, M. J., and Forbes, A., "Generating and analyzing non-diffracting vector vortex beams," Proc. of SPIE, 884305 (2013).

[66] Bomzon, Z. E., Biener, G., Kleiner, V., and Hasman, E., "Radially and azimuthally polarized beams generated by space-variant dielectric subwavelength gratings," Optics Letters, **27**(5), 285-287 (2002).

[67] Tervo, J., and Turunen, J., "Generation of vectorial propagation-invariant fields by polarization-grating axicons," Optics Communications, **192**(1), 13-18 (2001).

[68] Milione, G., Evans, S., Nolan, D. A., and Alfano, R. R., "Higher order Pancharatnam-Berry phase and the angular momentum of light," Physical Review Letters, **108**(19), 190401 (2012).

[69] Flores-Pérez, A., Hernández-Hernández, J., Jáuregui, R., and Volke-Sepúlveda, K., "Experimental generation and analysis of first-order TE and TM Bessel modes in free space," Optics Letters, **31**(11), 1732-1734 (2006).

[70] Marrucci, L., Manzo, C., and Paparo, D., "Pancharatnam-Berry phase optical elements for wave front shaping in the visible domain: switchable helical mode generation," Applied Physics Letters, **88**(22), 221102 (2006).

[71] Hodgson, N., and Weber, H., "Optical Resonators: Fundamentals, Advanced Concepts, Applications," Springer, **108**, (2005).

[72] Dudley, A., Li, Y., Mhlanga, T., Escuti, M., and Forbes, A., "Generating and measuring nondiffracting vector Bessel beams," Optics Letters, **38**(17), 3429-3432 (2013).

[73] Li, Y., Kim, J., and Escuti, M. J., "Orbital angular momentum generation and mode transformation with high efficiency using forked polarization gratings," Applied Optics, **51**(34), 8236-8245 (2012).

[74] Bouchal, Z., and Olivík, M., "Non-diffractive vector Bessel beams," Journal of Modern Optics, **42**(8), 1555-1566 (1995).

[75] Greene, P. L., and Hall, D. G., "Properties and diffraction of vector Bessel–Gauss beams," JOSA A, **15**(12), 3020-3027 (1998).

[76] Einstein, A., Podolsky, B., and Rosen, N., "Can quantum-mechanical description of physical reality be considered complete?," Physical Review, **47**(10), 777 (1935).

[77] Griffiths, D. J., and Harris, E. G., "Introduction to quantum mechanics," New Jersey: Prentice Hall, **2**, (1995).

[78] Bell, J. S., "On the einstein-podolsky-rosen paradox," Physics, **1**(3), 195-200 (1964).

[79] Aspect, A., Grangier, P., and Roger, G., "Experimental realization of Einstein-Podolsky-Rosen-Bohm Gedanken experiment: a new violation of Bell's inequalities," Physical Review Letters, **49**(2), 91 (1982).

[80] Weihs, G., Jennewein, T., Simon, C., Weinfurter, H., and Zeilinger, A., "Violation of Bell's inequality under strict Einstein locality conditions," Physical Review Letters, **81**(23), 5039 (1998).

[81] Rarity, J. G., and Tapster, P. R., "Experimental violation of Bell's inequality based on phase and momentum," Physical Review Letters, **64**(21), 2495 (1990).

[82] Vaziri, A., Weihs, G., and Zeilinger, A., "Experimental two-photon, three-dimensional entanglement for quantum communication," Physical Review Letters, **89**(24), 240401 (2002).

[83] Romero, J., Giovannini, D., Franke-Arnold, S., Barnett, S. M., and Padgett, M. J., "Increasing the dimension in high-dimensional two-photon orbital angular momentum entanglement," Physical Review A, **86**(1), 012334 (2012).

[84] Mafu, M., Dudley, A., Goyal, S., Giovannini, D., McLaren, M., Padgett, M. J., ...and Forbes, A., "Higher-dimensional orbital-angular-momentum-based quantum key distribution with mutually unbiased bases," Physical Review A, **88**(3), 032305 (2013).

[85] Vaziri, A., Pan, J. W., Jennewein, T., Weihs, G., and Zeilinger, A., "Concentration of higher dimensional entanglement: qutrits of photon orbital angular momentum," Physical Review Letters, **91**(22), 227902 (2003).

[86] McLaren, M., Filippus S. R., and Forbes, A., "Realising high-dimensional quantum entanglement with orbital angular momentum." arXiv preprint arXiv:1305.7102 (2013).

[87] Jack, B., Yao, A. M., Leach, J., Romero, J., Franke-Arnold, S., Ireland, D. G., and Padgett, M. J., "Entanglement of arbitrary superpositions of modes within two-dimensional orbital angular momentum state spaces," Physical Review A, **81**(4), 043844 (2010).

[88] Nagali, E., Sciarrino, F., De Martini, F., Marrucci, L., Piccirillo, B., Karimi, E., and Santamato, E., "Quantum information transfer from spin to orbital angular momentum of photons," Physical Review Letters, **103**(1), 013601 (2009).

[89] Torres, J. P., Deyanova, Y., Torner, L., and Molina-Terriza, G., "Preparation of engineered two-photon entangled states for multidimensional quantum information," Physical Review A, **67**(5), 052313 (2003).

[90] Zhang, P., Ren, X. F., Zou, X. B., Liu, B. H., Huang, Y. F., and Guo, G. C., "Demonstration of one-dimensional quantum random walks using orbital angular momentum of photons," Physical Review A, **75**(5), 052310 (2007).

[91] Groblacher, S., Jennewein, T., Vaziri, A., Weihs, G., and Zeilinger, A., "Experimental quantum cryptography with qutrits," New Journal of Physics, **8**(5), 75 (2006).

[92] Mirhosseini, M., Magaña-Loaiza, O. S., O'Sullivan, M. N., Rodenburg, B., Malik, M., Gauthier, D. J., and Boyd, R. W., "High-dimensional quantum cryptography with twisted light," arXiv preprint arXiv:1402.7113, (2014).

[93] Howell, J. C., Bennink, R. S., Bentley, S. J., and Boyd, R. W., "Realization of the Einstein-Podolsky-Rosen paradox using momentum-and position-entangled photons from spontaneous parametric down conversion,". Physical Review Letters, **92**(21), 210403 (2004).

[94] Franke-Arnold, S., Barnett, S. M., Padgett, M. J., and Allen, L., "Two-photon entanglement of orbital angular momentum states," Physical Review A, **65**(3), 033823 (2002)

[95] Leach, J., Jack, B., Romero, J., Ritsch-Marte, M., Boyd, R. W., Jha, A. K., and Padgett, M. J., "Violation of a Bell inequality in two-dimensional orbital angular momentum state-spaces," Optics Express, **17**(10), 8287-8293 (2009).

[96] McLaren, M., Agnew, M., Leach, J., Roux, F. S., Padgett, M. J., Boyd, R. W., and Forbes, A., "Entangled bessel-gaussian beams," Optics Express, **20**(21), 23589-23597 (2012).

[97] McLaren, M., Romero, J., Padgett, M. J., Roux, F. S., and Forbes, A., "Two-photon optics of Bessel-Gaussian modes," Physical Review A, **88**(3), 033818 (2013).

[98] Yu, T., and Eberly, J. H., "Sudden death of entanglement," Science, **323**(5914), 598-601 (2009).

[99] Almeida, M. P., de Melo, F., Hor-Meyll, M., Salles, A., Walborn, S. P., Ribeiro, P. S., and Davidovich, L. , "Environment-induced sudden death of entanglement," Science, **316**(5824), 579-582 (2007).

[100] Yu, T., and Eberly, J. H., "Sudden death of entanglement: classical noise effects," Optics Communications, **264**(2), 393-397 (2006).

[101] Al-Qasimi, A., and James, D. F., "Sudden death of entanglement at finite temperature," Physical Review A, **77**(1), 012117 (2008).

[102] Roux, F. S., "Infinitesimal-propagation equation for decoherence of an orbital-angular-momentum-entangled biphoton state in atmospheric turbulence," Physical Review A, **83**(5), 053822 (2011).

[103] Boyd, R. W., Rodenburg, B., Mirhosseini, M., and Barnett, S. M., "Influence of atmospheric turbulence on the propagation of quantum states of light using plane-wave encoding," Optics Express, **19**(19), 18310-18317 (2011).

[104] Brünner, T., and Roux, F. S., "Robust entangled qutrit states in atmospheric turbulence," New Journal of Physics, **15**(6), 063005 (2013).

[105] Kielpinski, D., Meyer, V., Rowe, M. A., Sackett, C. A., Itano, W. M., Monroe, C., and Wineland, D. J., "A decoherence-free quantum memory using trapped ions," Science, **291**(5506), 1013-1015 (2001).

[106] Viola, L., Fortunato, E. M., Pravia, M. A., Knill, E., Laflamme, R., and Cory, D. G., "Experimental realization of noiseless subsystems for quantum information processing," Science, **293**(5537), 2059-2063 (2001).

[107] Giovannini, D., Nagali, E., Marrucci, L., and Sciarrino, F., "Resilience of orbital-angular-momentum photonic qubits and effects on hybrid entanglement," Physical Review A, **83**(4), 042338 (2011).

[108] Pittman, T. B., Shih, Y. H., Strekalov, D. V., and Sergienko, A. V., "Optical imaging by means of two-photon quantum entanglement," Physical Review A, **52**(5), R3429 (1995).

[109] Strekalov, D. V., Sergienko, A. V., Klyshko, D. N., and Shih, Y. H., "Observation of two-photon "ghost" interference and diffraction," Physical Review Letters, **74**(18), 3600 (1995).

[110] Jack, B., Leach, J., Romero, J., Franke-Arnold, S., Ritsch-Marte, M., Barnett, S. M., and Padgett, M. J., "Holographic ghost imaging and the violation of a Bell inequality," Physical Review Letters, **103**(8), 083602 (2009).

[111] Bennink, R. S., Bentley, S. J., and Boyd, R. W., "Two-photon coincidence imaging with a classical source," Physical Review Letters, **89**(11), 113601 (2002).

[112] Gatti, A., Brambilla, E., Bache, M., and Lugiato, L. A., "Ghost imaging with thermal light: comparing entanglement and classical correlation," Physical Review Letters, **93**(9), 093602 (2004).

Chapter 7

Appendices

7.1 Appendix A

7.1.1 matlab codes

Digital axicon

```
%function b = BesselJ(kr,l)
%clc;
%clear all;
%close all;
N=1080;
M=1920;

SLM_bin = zeros(N,M);
l=1;
%lamda = 532*10^-9;
kr= 0.25;
for n = 1 : N
    for m = 1 : M
        SLM_bin(n,m) = mod(kr*sqrt((n-N/2)^2+(m-M/2)^2) + l*(atan2((
            n-N/2),(m-M/2))),2*pi);
    end
```

```
16 end
17
18 imwrite(mod(SLM_bin,2*pi)./max(mod(SLM_bin(:),2*pi)),'C:\Users\
       tmhlanga\Desktop\longrange Bbeam\L__rho_.25.bmp', 'bmp');
19
20
21 %2*pi*
22 %b = mod(SLM_bin,2*pi)/(2*pi);
```

```
1  clc;
2  clear all;
3  close all;
4  N = 1080;
5  M = 960; %half width of SLM
6
7  check = zeros(N,M);
8  SLM_bin = zeros(N,M);
9  L1=4;
10
11 for n=1:N
12     for m=1:M
13         n1=floor(n/7);
14         m1=floor(m/7);
15         if mod(n1+m1,2)==0
16             check(n,m)=pi;
17         else
18             check(n,m)=0;
19         end
20     end
21 end
22
```

```
rmin = round(280);
rmax = round(300);
for n = 1 : N
    for m = 1 : M
        r(n,m) = sqrt((m-M/2)^2+(n-N/2)^2);
        if r(n,m)<= rmax & r(n,m)>= rmin;
            bin_check(n,m) = mod(L1*(atan2((n-N/2),(m-M/2))),2*pi);
           %bin_check (n,m)=2*pi; % When L1=0 use this command
               instead
        else
         bin_check(n,m) = check(n,m);
        end
    end
end

%imwrite(mod(bin_check,2*pi)./max(mod(bin_check(:),2*pi)),'4 radius
   200-220 pixels.bmp', 'bmp');

%image((abs(fftshift(IMG)))*10);
image( bin_check(n,m));
%imwrite (bin_check./max(bin_check (:)),'0 radius 300-320 pixels.bmp
   ', 'bmp'); % When L1=0 use this
command insteada
```

Spiral ring-slit

```
clc;
clear all;
close all;
N = 1080;
M = 960; %half width of SLM

```

```
7  check = zeros(N,M);
8  SLM_bin = zeros(N,M);
9  L1=4;
10
11 for n=1:N
12     for m=1:M
13         n1=floor(n/7);
14         m1=floor(m/7);
15         if mod(n1+m1,2)==0
16             check(n,m)=pi;
17         else
18             check(n,m)=0;
19         end
20     end
21 end
22
23 rmin = round(280);
24 rmax = round(300);
25 for n = 1 : N
26     for m = 1 : M
27         r(n,m) = sqrt((m-M/2)^2+(n-N/2)^2);
28         if r(n,m)<= rmax & r(n,m)>= rmin;
29             bin_check(n,m) = mod(L1*(atan2((n-N/2),(m-M/2))),2*pi);
30             %bin_check (n,m)=2*pi; % When L1=0 use this command
                   instead
31         else
32          bin_check(n,m) = check(n,m);
33         end
34     end
35 end
```

```
36
37 %imwrite(mod(bin_check,2*pi)./max(mod(bin_check(:),2*pi)),'4 radius
       200-220 pixels.bmp', 'bmp');
38
39 %image((abs(fftshift(IMG)))*10);
40 image( bin_check(n,m));
41 %imwrite (bin_check./max(bin_check (:)),'0 radius 300-320 pixels.bmp
       ', 'bmp'); % When L1=0 use this
42 command insteada
```

Detection of Bessel beams with digital axicons

Abderrahmen Trichili,[1] **Thandeka Mhlanga,**[2,3] **Yaseera Ismail,**[3] **Filippus S. Roux,**[2] **Melanie McLaren,**[2] **Mourad Zghal,**[1] **and Andrew Forbes,**[2,3]

[1]*University of Carthage, Engineering School of Communication of Tunis (Sup'Com), GreS'Com Laboratory, Ghazala Technopark, 2083, Ariana, Tunisia*
[2]*CSIR National Laser Centre, P.O. Box 395, Pretoria 0001, South Africa*
[3]*School of Physics, University of KwaZulu-Natal, Private Bag X54001, Durban 4000, South Africa*

aforbes1@csir.co.za

Abstract: We propose a simple method for the detection of Bessel beams with arbitrary radial and azimuthal indices, and then demonstrate it in an all-digital setup with a spatial light modulator. We confirm that the fidelity of the detection method is very high, with modal cross-talk below 5%, even for high orbital angular momentum carrying fields with long propagation ranges. To illustrate the versatility of the approach we use it to observe the modal spectrum changes during the self-reconstruction process of Bessel beams after encountering an obstruction, as well as to characterize modal distortions of Bessel beams propagating through atmospheric turbulence.

OCIS codes: (090.1995) Digital holography; (070.6120) Spatial light modulators; (0.50.4865) Optical vortices.

References and links

1. J. Durnin,"Exact solutions for nondiffracting beams. I. The scalar theory," J. Opt. Soc. Am. A **4**(4), 651-654 (1987).
2. J. Durnin, J. J. Miceli, and J. H. Eberly, "Diffraction-Free Beams," Phys. Rev. Lett. **58**(15), 1499-1501 (1987).
3. D. McGloin, and K. Dholakai, "Bessel beams: diffraction in new light," Contemp. Phys.**46**(1),15-28 (2005).
4. M. Mazilu, D. J. Stevenson, F. Gunn-Moore, and K. Dholakia "Light beats the spread: non-diffracting beams," Laser Photon. Rev. **4**(4), 529-47 (2010).
5. A.Dudley, M.Lavery, M. Padgett, A. Forbes, "Unraveling Bessel Beams," Opt. Photon. News, **24**(6), 22-29 (2013)
6. M. McLaren, T. Mhlanga, M. J. Padgett, F. S. Roux, and A. Forbes, "Self-healing of quantum entanglement after an obstruction," Nat. Commun. **5**:3248 (2014).
7. M. McLaren, M. Agnew, J. Leach, F. S. Roux, M. J. Padgett, R. W. Boyd, and A. Forbes, "Entangled Bessel-Gaussian beams, " Opt. Express **20**(21), 23589-23597 (2012).
8. H. C. Ramrez, R. R. Alarcón, F. J. Morelos, P. A. Q. Su, J. C. G. Vega, and A. B. U'Ren, "Observation of non-diffracting behavior at the single-photon level, " Opt. Express **20**(28), 29761-29768 (2012).
9. F. Gori and G. Guattari, "Bessel-Gauss beams," Opt. Commun. **64**(6), 491-495 (1987).
10. M. A. Mahmoud, M. Y. Shalaby, and D. Khalil, "Propagation of Bessel beams generated using finite-width Durnin ring," Appl. Opt. **52**(2), 256-263 (2013).
11. R. M. Herman and T. A. Wiggins, "Production and uses of diffractionless beams," J. Opt. Soc. Am. A **8**(6), 932-942 (1991).
12. J. Alrt and K. Dholakia, "Generation of high-order bessel beams by use of an axicon," Opt. Commun. **177**, 277-301 (2000).
13. A. Vasara, J. Turunen, and A. T. Friberg, "Realization of general nondiffracting beams with computer-generated holograms," J. Opt. Soc. Am. A **6**(11), 1748-1754 (1989).
14. C. Paterson, R. Smith, "Higher-order Bessel waves produced by axicon-type computer-generated holograms," Opt. Commun. **124**, 121-130 (1996).

15. R. Bowman, N. Muller, X. Zambrana-Puyalto, O. Jedrikiewicz, P. Di Tramapani, and M.J. Padgett, "Efficient generation of Bessel beam arrays by means of an SLM," Eur. Phys. J. Special Topics **199**, 159-166 (2011).
16. Z. Y. Rong, Y. J. Han, S. Z. Wang, and Cheng-Shan Guo, "Generation of arbitrary vector beams with cascaded liquid crystal spatial light modulators," Opt. Express **22**(2), 1636-1644 (2014).
17. R. Vasilyeu, A. Dudley, N. Khilo, and A. Forbes, "Generating superpositions of higher-order Bessel beams," Opt. Express **17**(26), 23389-23395 (2009).
18. A. Dudley, Y. Li, T. Mhlanga, M. Escuti, and A. Forbes, "Generating and measuring nondiffracting vector Bessel beams," Opt. Lett. **38**(17), 3429-3432 (2013).
19. A. Dudley, T. Mhlanga, M. Lavery, A. McDonald, F. S. Roux, M. J. Padgett, and A. Forbes, "Efficient sorting of Bessel beams, " Opt. Express **21**(1), 165-171 (2013).
20. A. Mourka, M. Mazilu, E. M. Wright, and K. Dholakia "Modal characterization using principal component analysis: application to Bessel, higher-order Gaussian beams and their superpositions," Scientific Reports **3**, 1422 (2013).
21. M. Mazilu, A. Mourka, T. Vettenburg, E. M. Wright, and K. Dholakia "Simultaneous determination of the constituent azimuthal and radial mode indices for light fields possessing orbital angular momentum," Appl. Phys. Lett. **100**, 231115 (2012).
22. I. Litvin, M. McLaren, and A. Forbes, "A conical wave approach to calculating Bessel-Gauss beam reconstruction after complex obstacles," Opt. Commun. **282**, 1078-1082 (2009).
23. Z. Bouchal, J.Wanger, M. Chulpl, "Self-reconstruction of a distorted nondiffracting beam," Opt. Commun. **151**, 207-211 (1998).
24. I. A. Litvin, A. Dudley, F. S. Roux, and A. Forbes, "Azimuthal decomposition with digital holograms," Opt. Express **20**(10), 10996-11004 (2012).
25. A. Janssen, S. van Haver, P. Dirksen, J. Braat,"Zernike representation and strehl ratio of optical systems with numerical aperture,"J. Mod. Opt. **55**(7), 1127-1157 (2008).
26. J. Ou, Y. Jiang, J. Zhang, H. Tang, Y. He, S. Wang, J. Liao, "Spreading of spiral spectrum of Bessel-Gaussian beam in non-Kolmogorov turbulence," Opt. Commun. **318**, 95-99 (2014).
27. W. Nelson, J. P. Palastro, C. C. Davis, and P. Sprangl, "Propagation of Bessel and Airy beams through atmospheric turbulence," J. Opt. Soc. Am. A **31**(3), 603-609 (2014).

1. Introduction

Since their discovery in 1987 by Durnin [1,2], Bessel beams have been extensively studied due to their nominally non-diffracting behaviour and their ability to self-reconstruct after encountering an obstruction [3–5] . These beams are characterized by a radial wave vector (k_r) and azimuthal index (ℓ), which results from their helical wave front structure. As a result Bessel beams carry orbital angular momentum (OAM), even down to the single photon level [6–8]. However an ideal Bessel beam requires an infinite amount of energy; this beam is practically approximated in a finite region by Bessel Gaussian (BG) Beams [9]. Such beams have been generated using annular ring-slits in the far field [2,10], axicons in the near field [11,12], as well as the digital equivalent of both [13–16]. These beams have been further explored by generating their superpositions [17], and converting them into vector BG beams [18]. An emerging area of research is optical communication with the spatial modes of light, where Bessel beams are also mooted to play a role, yet very little work has been done on the topic of two-dimensional detection of such modes [19–21].

In this paper we demonstrate the detection of Bessel beams by a simple scheme comprising only a helical axicon and a lens. We outline the concept, illustrate how it may be implemented optically and then demonstrate it with digitally encoded phase-only holograms. We apply the tool to the self-healing process of Bessel beams after an obstruction as well as to Bessel beams propagating through turbulence, and observe the changing radial and azimuthal spectrums for the first time. Our results will be relevant to future studies in optical communication with Bessel beams. Such fields are interesting for communication purposes since they carry OAM over extended distances in a nominally non-diffracting manner, and hence may be advantageous for signal delivery to distance receivers.

2. Theoretical background

2.1. Bessel-Gaussian modes

The Bessel-Gaussian (BG) modes [9] in polar coordinates, are given by

$$E_{\ell}^{BG}(r,\Phi,z) = \sqrt{\frac{2}{\pi}} J_{\ell}\left(\frac{z_R k_r r}{z_R - iz}\right) \exp(i\ell\Phi - ik_z z) \exp\left(\frac{ik_r^2 z w_0^2 - 2kr^2}{4(z_R - iz)}\right), \tag{1}$$

where ℓ is the azimuthal index (a signed integer), $\mathrm{J}_{\ell}(\cdot)$ is the Bessel function of order ℓ; k_r and k_z are the radial and longitudinal wave numbers. The initial radius of the Gaussian profile is w_0 and the Rayleigh range is $z_R = \pi w_0^2/\lambda$. The propagation constant k and the parameters k_r and k_z are related by $k^2 = k_r^2 + k_z^2$. While BG modes are nominally non-diffracting, they nevertheless have a finite propagation distance when generated in the laboratory, given by

$$z_{max} = \frac{w_0 \lambda}{2\pi k_r}. \tag{2}$$

Bessel beams also exhibit reconstruction of the amplitude and phase of the beam after encountering an obstruction [22, 23]. For such beams, there is a minimum distance behind an obstacle of radius R_{obs} before reconstruction occurs. This distance represents the shadow region which is given by

$$z_{min} = \frac{2\pi R_{obs}}{k_r \lambda}. \tag{3}$$

The BG modes form a complete orthonormal basis in terms of which an arbitrary paraxial laser beam may be expanded. In the case of Bessel beams we note that there are two indices used to describe the field: the discrete parameter, ℓ, and the continuous parameter k_r. The former determines the helicity of the wavefronts and is related to the OAM content of the field, while the latter determines the spacing of the intensity rings observed in Bessel beams.

2.2. Concept

The task is to find the modal content of the field for all values of ℓ and k_r, which we will show can be achieved with a simple optical set-up comprising a lens and a digital hologram encoded to represent an axicon. Recall that a Gaussian beam illuminating an axicon produces a BG beam as the output. From the reciprocity of light the reverse process must convert a BG beam back into a Gaussian beam. Herein lies the possibility of detecting particular BG modes, since Gaussian modes may readily be detected by single mode fibers. The concept is shown schematically in Fig. 1. Consider first a ray-based analysis following a heuristic argument: an incoming Gaussian mode is converted by the first axicon to a BG mode of radial wavevector $k_r = k(n-1)\gamma$, where n is the refractive index of the axicon and γ is the axicon cone angle. This results in conical refraction at an angle $\theta = (n-1)\gamma = k_r/k$. If this BG mode passes through an identical (reversed) axicon, then the refracted rays are collimated, or equivalently, the Gaussian mode is generated again. If, on the other hand, the cone angle of the second axicon does not match the cone angle of the incoming BG beam, then the outgoing rays will not be perfectly corrected and equivalently a pure Gaussian mode will not be formed. This detection is therefore k_r specific and is reminiscent of a conventional lens telescope but with conical axicons rather than spherical lens. With the addition of a spiral plate with transmission function $\exp(i\ell\phi)$ the detection method becomes specific to the BG order ℓ as well.

This heuristic argument made more concrete by considering the problem from a physical optics perspective and employing digital holograms for the detection. The detection hologram may be written as

$$t_{SLM} = \exp(i\tilde{k}_r r - i\ell\phi), \tag{4}$$

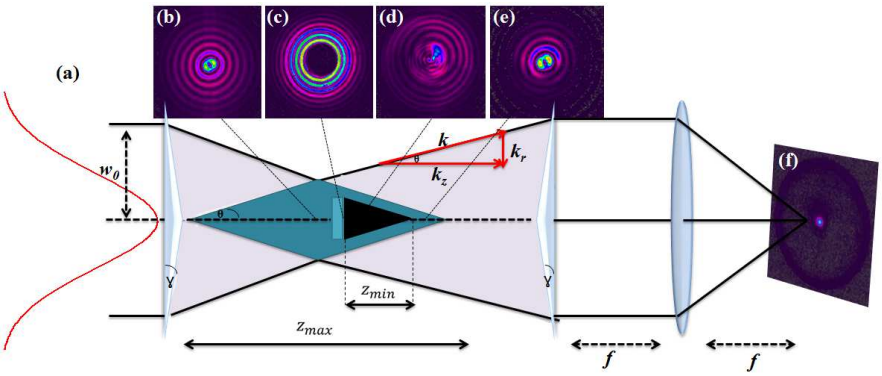

Fig. 1. A diagram illustrating the generation and the detection of Bessel-Gaussian beams. (a) The BG beam is generated using a programmed hologram of an axicon, illuminating by a Gaussian beam, and exists in a finite region, z_{max}. An obstacle placed in the center of the BG region obstructed the generated beam for a minimum distance, z_{min}, after which the BG mode reconstructs. (b-e) experimental beam images of a Bessel beam of order $\ell = 1$ at four different positions. (f) The BG beam is detected at the far field of a programmed hologram of a second axicon.

where the first term represents an axicon to detect a BG with a radial wavevector of $\tilde{k}_r$ and the second term specifies the order, ℓ. Such a hologram is shown in Fig. 2 (a) and the BG mode that it will detect in Figs. 2 (b) and (c). An inner product measurement is performed optically with the same set-up by considering the signal at the origin of the focal plane of the lens [24]. The resulting signal can be calculated numerically from

$$g_{out} = \mathscr{F}\left\{E_\ell^{BG}\right\} \otimes \mathscr{F}\left\{t_{SLM}\right\}, \tag{5}$$

where g_{out} represents the field at the output plane (focal plane of the lens), $\mathscr{F}$ is the Fourier transform, $\otimes$ denotes the convolution process and E_ℓ^{BG} is the incoming BG beam defined in (1). The angular spectrum of a BG mode and the Fourier transform of the transmission function both have the shape of an annular ring. Provided that the radii of these annular rings (which represent the k_r values of the modes) are equal, the convolution of these rings will produce a bright spot with a Gaussian profile in the center of the output plane, as shown in Fig. 2 (d). This central peak is surrounded by a ring of twice the radius. If there is a mismatch in the respective

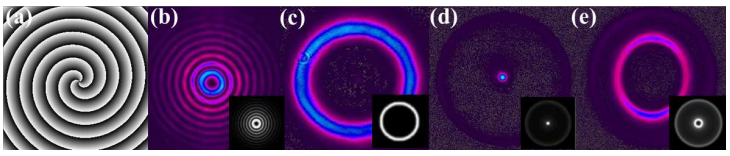

Fig. 2. Experimental images of (a) a digital hologram for the detector of a BG mode with $\ell = 3$ and (b) a BG mode profile of $\ell = 3$ and (c) its Fourier transform (annular ring). The signal at the detector is shown for the scenarios of (d) matching k_r and ℓ and (e) matching in ℓ but no matching in k_r. The black and white insets show the theoretical results.

radii (k_r values) the central spot will itself become a small ring with a low intensity in the center, which will cause a negligible signal on the detector, as shown in Fig. 2 (e). To quantify this we note that the width of the annular ring ($\mathscr{F}\left\{E_\ell^{BG}\right\}$) is governed by the radius of the

Gaussian envelope of the BG mode. On the other hand, the width of the ring due to $\mathscr{F}\{t_{SLM}\}$ is determined by the size of the SLM and is therefore much smaller than the corresponding width for the BG mode. We'll therefore assume that the ring for the axicon transmission function is vanishingly thin. The convolution of the two rings produces a function consisting of two rings with radii that are respectively equal to the sum and difference of the radii of the original rings. Thus if the original radii were equal the convolution produces a central spot. Conversely, if these original radii differ the intensity at the center of the output is given by $\exp[-(\Delta R/w_0)^2]$, where Δr is the difference between the original radii. For $\Delta R > 1.5w_0$ the intensity at the center is essentially zero and the corresponding functions are considered to be orthogonal. Likewise, if the ℓ value of the BG mode is different from that of the transmission function of the SLM, they won't canceled during the convolution process. Such a mismatch in ℓ values will cause the central peak in the convolution to have a phase singularity in the center and thus a central intensity null, which will produce a negligible signal on the detector. Hence the BG mode detection method is sensitive to both radial (k_r) and azimuthal (ℓ) indices.

3. Experimental Setup and Results

The experimental realization of the BG mode decomposition comprises of two parts: (1) the generation of a BG beam with known parameters (modal profile) and (2) the detection of this beam by modal analysis. This is accomplished by the optical system shown in Fig. 3, where the created BG beam on SLM_1 is assumed to be our "unknown" beam. A HeNe laser was expanded with a $3\times$ telescope and directed onto a spatial light modulator (SLM), denoted as SLM_1, with a beam width of $w_0 = 1$ mm. The SLM (Holoeye, PLUTO-VIS, 1920×1080 pixels, with a pixel pitch of 8μm) was calibrated for a 2π phase shift at a wavelength of 633 nm. SLM_1 was programmed with the conical phase of an axicon, plus a helical phase with an azimuthal index ℓ ranging from -10 to 10.

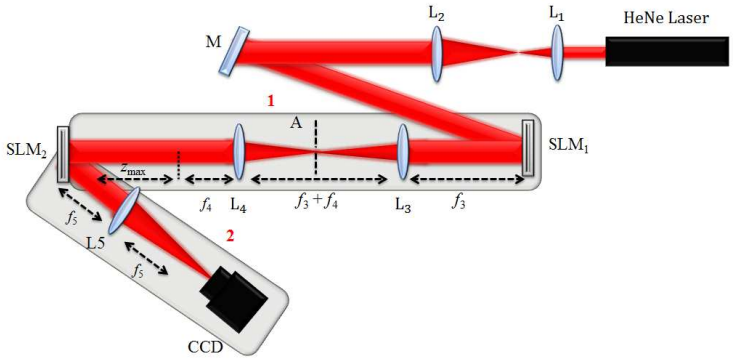

Fig. 3. A schematic of the experimental setup for accomplishing the decomposition of a Bessel field. The Lenses L_1, L_2, L_3, L_4 and L_5 have focal lengths $f_1 = 100$ mm, $f_2 = 300$ mm, $f_3 = 500$ mm, f_4 =500 mm and f_5=150 mm, respectively. A is the filtering aperture. SLM_1 and SLM_2 denote the two spatial light modulators and M represents a mirror. The detector was a CCD camera.

The resulting image was filtered through the $4f$ imaging system, and propagated a distance of $z_{max} = 340$ mm (for $k_r = 31250$ rad/m) onto the detection SLM, denoted as SLM_2, where the transmission function was scanned through the spectrum of ℓ and k_r values and the resulting signal detected by a CCD camera placed after a Fourier transforming lens (L_5).

A full modal decomposition was done in k_r and ℓ at the plane $z = z_{max}$ with the results shown

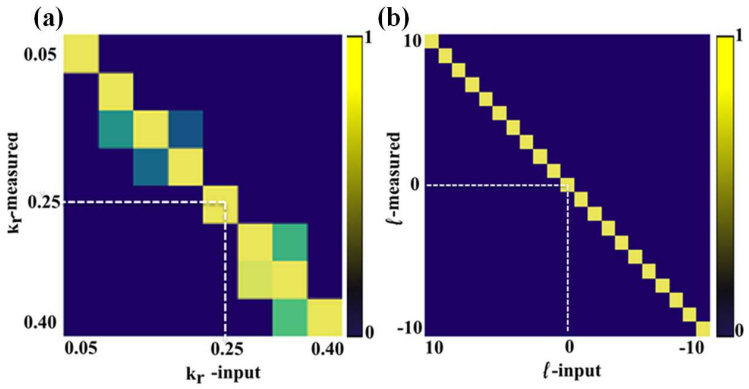

Fig. 4. (a) Bessel beam radial, k_r, decomposition for $\ell = 1$. Units of k_r are rad/pixel. (b) Bessel beam azimuthal, ℓ, decomposition for $k_r = 0.25$ rad/pixel.

in Fig. 4 (a) and Fig. 4 (b). The uncertainty in detection of the order ℓ is clearly negligible while that for the radial wavevector is approximately 5% (one std dev). It is clear that a wide range of Bessel modes can be detected quickly and accurately with this scheme. Next, we illustrate the versatility of our approach by applying it to two perturbation studies: the self-healing of Bessel beams after an obstacle and the propagation of Bessel beams through turbulence. We use our detection method to experimentally observe the change in modal spectrum during these processes.

3.1. Bessel Reconstruction

A circular opague disk, with a radius of $R_{obs} = 300\ \mu$m, was used as the obstruction. The disk was initially placed at $\frac{3}{4}z_{max}$ for a BG of $k_r = 0.25$. The detection was done at $z = \frac{3}{4}z_{max}$ while the disk was moved away from the detection plane until exceeding the self-healing distance of $z_{min} = 9.5$ cm. The radial and azimuthal spectrum was measured before the obstruction and then at various distances after the obstruction until the self-healing process completed. We observed (see Fig. 5) minimal azimuthal distortion of the mode due to the obstruction, but significant broadening of the radial modes. This broadening reduces as the beam self-heals, returning to the initial spectrum after the self-healing distance. While the self-healing of Bessel beams has been studied extensively before, this is the first time that the process has been observed using modal analysis.

3.2. Bessel propagation through turbulence

Finally, we applied our tool to the study of Bessel beams propagating through turbulence, a topic that has received much theoretical attention of late. We simulated atmospheric turbulence using a diffractive plate encoded for Kolmogorov turbulence, which for the purposes of this study we characterize by the Strehl ratio [25]. The turbulence plate was placed at $\frac{1}{2}z_{max}$ and the detector at $z = z_{max}$. Two turbulence strengths were used corresponding to Strehl ratios of SR = 0.2 and SR = 0.03, with the impact on the Bessel modes shown in Fig. 6. Without the plate the results are identical to those shown earlier: narrow k_r and ℓ spectrums with little cross-talk, as seen in Figs. 7 (a) and (b). At medium turbulence levels (SR = 0.2), the k_r spectrum broadens and so does the OAM spectrum [Figs. 7 (a) and (c)], becoming wider [Figs. 7 (a) and (d)] as the turbulence becomes very strong (SR = 0.03). These results are consistent with that predicted by theory [26, 27], and serves to illustrate the versatility of the tool.

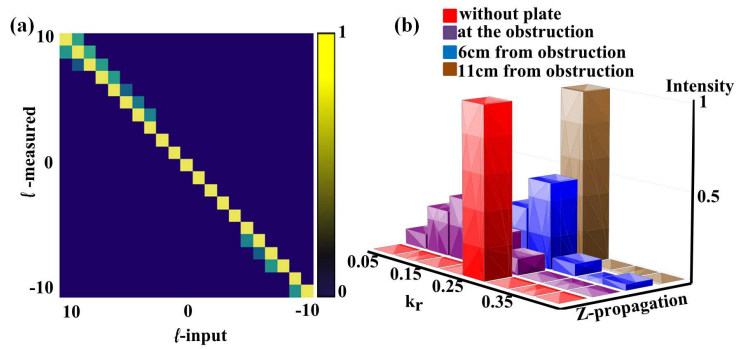

Fig. 5. (a) Azimuthal decomposition (ℓ detection) of the fully obstructed beam and (b) k_r decomposition without an obstruction and then at three planes with the obstruction.

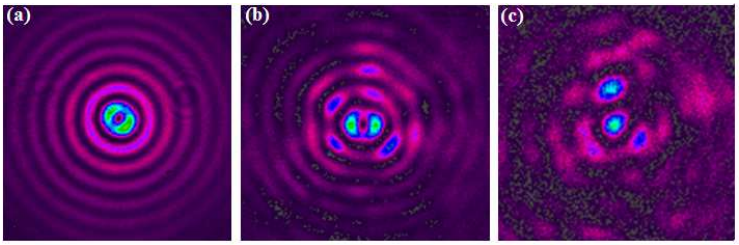

Fig. 6. Images of a Bessel-Gaussian mode profile for $\ell = 1$ (a) without turbulence, after passing a turbulence of (b) SR=0.2 and (c) SR=0.03.

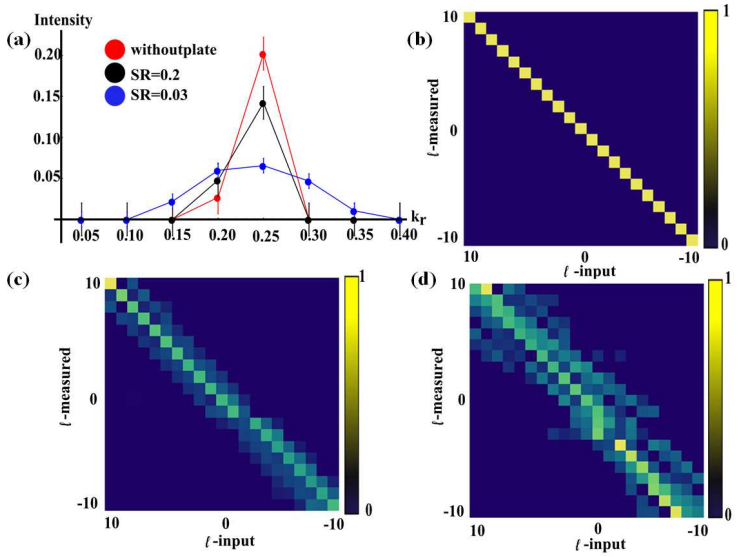

Fig. 7. (a) $k_r = 0.25$ rad/pixel decomposition for different strehl ratio's. (b) ℓ decomposition spectrum without turbulence. (c) and (d) ℓ decomposition spectrum for SR=0.2 and SR=0.03, respectively.

4. Conclusion

We have presented a versatile technique to experimentally realize the detection of Bessel beams using digital axicons programmed on a spatial light modulator. We have shown the ability to distinguish both the radial and azimuthal indices of such beams, a core requirement for optical communication protocols if the bit rate per photon is to be increased by exploiting all the degrees of freedom of spatial modes. In addition we have considered two applications of the tool and observed the modal changes to an incoming Bessel beam due to both amplitude and phase perturbations resulting from an opaque obstacle and a turbulence plate, respectively. The ability to modally resolve such fields will find uses in both quantum and classical studies.

5. Acknowledgment

This work has been supported by African Laser Centre (ALC) project “Towards spatial mode control in fibres for high bit rate optical communication”. The authors wish to thank Angela Dudley for useful advice.

nature COMMUNICATIONS

ARTICLE

Received 17 Oct 2013 | Accepted 10 Jan 2014 | Published 6 Feb 2014

DOI: 10.1038/ncomms4248

Self-healing of quantum entanglement after an obstruction

Melanie McLaren[1,2], Thandeka Mhlanga[1,3], Miles J. Padgett[4], Filippus S. Roux[1] & Andrew Forbes[1,2]

Quantum entanglement between photon pairs is fragile and can easily be masked by losses in transmission path and noise in the detection system. When observing the quantum entanglement between the spatial states of photon pairs produced by parametric down-conversion, the presence of an obstruction introduces losses that can mask the correlations associated with the entanglement. Here we show that we can overcome these losses by measuring in the Bessel basis, thus once again revealing the entanglement after propagation beyond the obstruction. We confirm that, for the entanglement of orbital angular momentum, measurement in the Bessel basis is more robust to these losses than measuring in the usually employed Laguerre–Gaussian basis. Our results show that appropriate choice of measurement basis can overcome some limitations of the transmission path, perhaps offering advantages in free-space quantum communication or quantum processing systems.

[1] CSIR National Laser Centre, P.O. Box 395, Pretoria 0001, South Africa. [2] Laser Research Institute, University of Stellenbosch, Stellenbosch 7602, South Africa. [3] University of Kwa-Zulu Natal, Private Bag X54001, Durban 4000, South Africa. [4] Department of Physics and Astronomy, SUPA, University of Glasgow, Glasgow G12 8QQ, UK. Correspondence and requests for materials should be addressed to A.F. (email: aforbes1@csir.co.za).

Quantum entanglement in the orbital angular momentum (OAM) modes of photons has been topical of late, promising to offer access to high-dimensional Hilbert spaces[1]. It was shown that beams with an azimuthal phase dependence $\exp(i\ell\phi)$ carry an OAM of $\ell\hbar$ per photon, where the azimuthal index ℓ can assume any integer value[2]. Laguerre–Gaussian (LG) modes are examples of such beams and are commonly used to exploit the OAM property of light[3,4]. As such, the LG modes were first used to demonstrate OAM entanglement[5]. However, a variety of bases may also be used to demonstrate OAM entanglement, including Ince–Gaussian[6], Bessel–Gaussian (BG)[7,8] as well as mutually unbiased bases derived from these sets[9,10]. The OAM modal basis defines an infinite-dimensional Hilbert space, allowing access to high-dimensional entanglement[11]. An increase in dimension leads to improved security in quantum key distribution as well as increased information capacity in quantum communication protocols[12,13].

Unfortunately, while photons are weakly interacting, their entanglement is nevertheless fragile to the environment[14]. There have been a number of efforts in mitigating the decoherence in quantum computers and information processes based on ion traps, nuclear magnetic resonance and hyper-entanglement[15–17]. There have also been theoretical suggestions to recover lost entanglement[18]; however, it is yet to be demonstrated experimentally. In the context of OAM modes, the decay of entanglement has been both predicted[19] and measured[20] for atmospheric turbulence as an environment, with some success in diminishing these effects[21–23].

Here we investigate the ability of OAM modes to recover the measured degree of entanglement of the quantum state after encountering an obstruction. It is well known that BG beams have the ability to self-heal after encountering an obstruction[24,25]. An obstruction placed in the path of one of the down-converted photons introduces an optical loss such that the OAM entanglement, as witnessed by the Clauser Horne Shimony Holt (CHSH) inequality, is obscured. We then show that by measuring in the BG basis the classical self-healing of the Bessel profile gives a higher signal and the OAM entanglement is once again revealed. We demonstrate a dependence of the calculated concurrence of the quantum state on the location of the obstruction within the propagation path, and find that this is in agreement with the classical self-healing distance of BG beams. We thus find that even when applied to single photons this self-healing property of the Bessel beam allows us to overcome the losses associated with the obstruction such that the spatial correlations can be measured with sufficient fidelity to reveal the quantum entanglement of the photon pairs.

Results

Bessel beams. Bessel beams represent a class of nominally propagation-invariant solutions to the Helmholtz equation[26] and have been extensively investigated to date[27]. A laboratory approximation to these fields, BG beams, has similar properties over finite distances[28], including their ability to reconstruct both in amplitude and phase after encountering an obstruction[24,25]. Although this property has been studied using classical light and single photons[29], it may also be applicable in quantum processes.

Higher-order Bessel and BG beams have helical wavefronts and carry OAM[30]. Entanglement of the OAM modes in the BG basis has been shown to offer a wider spiral spectrum as compared with the LG basis[7].

A BG beam is a superposition of plane waves with wave vectors that lie on a cone[28]. The electric field of a scalar BG mode of order ℓ is given by

$$E_\ell^{\mathrm{BG}}(r,\phi,z) = \sqrt{\frac{2}{\pi}}\, \mathrm{J}_\ell\left(\frac{z_\mathrm{R} k_r r}{z_\mathrm{R} - iz}\right) \exp(i\ell\phi - ik_z z) \times \exp\left(\frac{ik_r^2 z w_0^2 - 2kr^2}{4(z_\mathrm{R} - iz)}\right), \quad (1)$$

where ℓ is the azimuthal (mode) index (a signed integer); $\mathrm{J}_\ell(\cdot)$ is the Bessel function of the first kind; k_r and k_z are the radial and longitudinal wave vectors, respectively. The initial radius of the Gaussian profile is w_0 and the Rayleigh range is $z_\mathrm{R} = \pi w_0^2/\lambda$, where λ is the wavelength of the BG mode. A BG beam has a finite propagation distance, $z_{\max}$, over which it is said to be nominally non-diffracting[27], shown as the shaded diamond-like region in Fig. 1. In this region the incoming plane waves are refracted through an axicon (conical lens) and interfere to form the BG beam. The resulting wave vectors lie on a cone of angle $\theta = \arcsin(k_r/k)$. Using simple geometric arguments, the maximum propagation distance is defined as $z_{\max} = 2\pi w_0/\lambda k_r$, where $\sin(\theta) \approx \theta$ for small θ. If an obstruction of radius R is

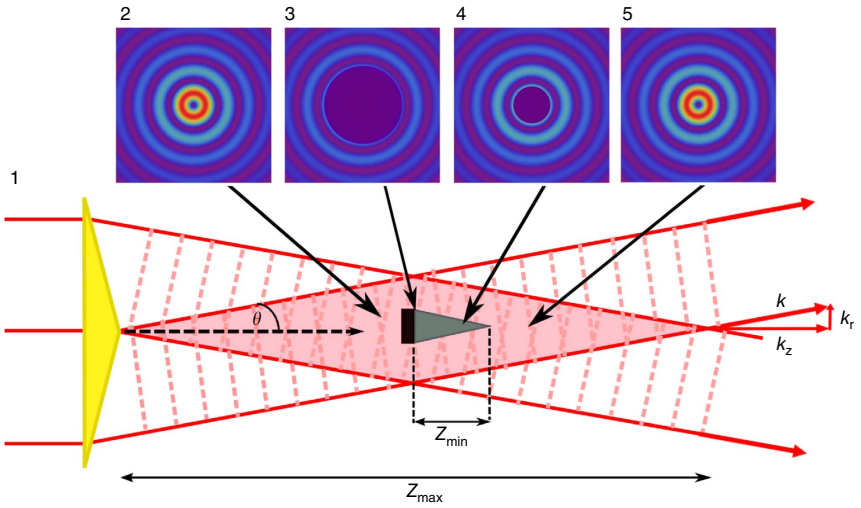

Figure 1 | Self-healing property of BG beams. The BG beam is generated using a computer-generated hologram of an axicon (yellow triangle) and exists in a finite region, $z_{\max}$ (pink diamond). An obstacle placed in the centre of the BG region (black rectangle) obstructs the beam for a minimum distance, $z_{\min}$ (grey triangle), after which the BG field reforms. The insets display the expected image of the beam at four different planes.

placed in the BG field, a shadow region is formed (see Fig. 1). However, those plane waves that bypass the obstruction will again interfere to form a BG beam[24,25]. The distance after which the field will recover is given by

$$z_{\min} \approx \frac{R}{\theta} \approx \frac{2\pi R}{k_r \lambda}, \qquad (2)$$

and is determined from purely geometric arguments[31]. The insets in Fig. 1 show the effect of an obstruction on the expected BG field at different planes.

We generate BG modes by encoding a phase-only hologram onto a spatial light modulator (SLM)[32,33]. The transmission function of this hologram is written as

$$T(r,\phi) = \mathrm{sign}\{J_\ell(k_r r)\}\exp(i\ell\phi), \qquad (3)$$

where sign$\{\cdot\}$ denotes the sign function. In the following experimental results, we generated a BG mode with $k_r = 30\ \mathrm{rad\,mm^{-1}}$.

Our experimental setup, shown in Fig. 2, consisted of a type-I crystal used to produce collinear, degenerate entangled pairs of photons via spontaneous parametric down-conversion (SPDC). A glass plate with a circular obstruction with a 200-μm radius was placed after the crystal in the path of the down-converted light and mounted on a z-axis translation stage. The plane of the crystal was imaged with a $\times 2$ magnification onto two separate SLMs, where the state into which the photon was projected is defined. Each SLM plane was then imaged with a $\times 250$ demagnification to the input of a single-mode fibre (SMF), which only allows the propagation of the fundamental mode. The SMFs were attached to avalanche photodiodes (APDs), which were in turn connected to a coincidence counter.

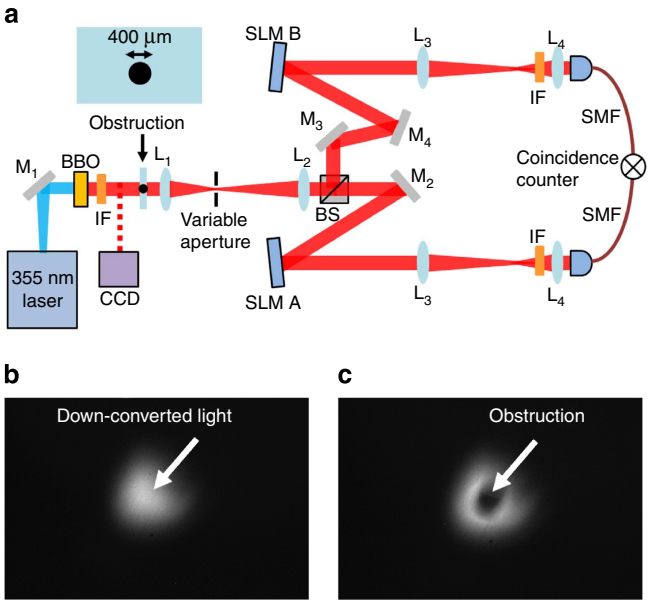

Figure 2 | Experimental setup. The setup shown was used to measure the effect of an obstruction in the path of the down-converted light. (**a**) An ultraviolet laser source pumped a type-I BBO crystal to produce pairs of entangled photons via SPDC. The crystal plane was imaged onto two separate SLMs using lenses L_1 ($f_1 = 200$ mm) and L_2 ($f_2 = 400$ mm). Each SLM plane was again imaged to the input of an SMF using lenses L_3 ($f_3 = 500$ mm) and L_4 ($f_4 = 2$ mm). (**b**) The down-converted beam at the plane of the crystal. (**c**) A circular obstruction (radius = 200 μm) was placed between the crystal and lens L_1, in the path of the down-converted light.

Setup. The experimental setup in Fig. 2 was first aligned in back-projection mode, where a classical laser source was connected to one of the SMFs to allow light to propagate through the system in reverse. Klyshko's advanced-wave representation considered the field detected in arm A as propagating in reverse back to the crystal plane, where it reflects off the crystal to propagate forward through the system to detector B[34]. This method has been shown to be useful in examining the conditional probability distribution of the coincidence count rate[8]. We implemented this concept experimentally by disconnecting fibre A from one of the APDs and reconnecting it to a continuous light source at $\lambda = 710$ nm. The classical light was directed onto SLM A and imaged to the crystal plane via lenses L_1 and L_2. Images of the obstruction were recorded by placing a mirror between the crystal and obstruction and a CCD camera at the plane of the crystal. Classical images of the self-healing property are shown in Fig. 3 for both the BG (Fig. 3a–d) and LG (Fig. 3e–h) modes, where the unobstructed BG and LG modes are shown in (a) and (e), respectively. We calculated the maximum propagation distance of the BG field as $z_{\max} = 169.6$ mm. The obstruction was first placed at the plane of the crystal, which is clearly shown in both (b) and (f). It was then moved 20 mm away from the crystal plane, shown in (c) and (g). The final images, (d) and (h), were taken 50 mm away from the crystal. It is clear that the BG mode has reformed at 50 mm, while the LG mode has not resumed its original structure. In a typical self-healing experiment[25], the obstruction is placed at a fixed position in the path of the beam and the CCD camera is moved such that the subsequent planes behind the obstruction can be imaged. However, an identical effect is seen if the CCD camera remains fixed, imaging one particular plane, and the obstruction is moved away from that plane. This is illustrated in Fig. 4, where we consider back-projected light directed from the SLM to the crystal. The obstruction is moved away from the crystal towards lens L_1. As the obstruction moves, the shadow region falling on the crystal becomes less significant until finally it no longer falls on the crystal and the recovered mode is observed as shown in Fig. 3d.

From equation (2), we calculated a minimum self-healing distance of ~ 29 mm for $R = 200$ μm and $k_r = 30\ \mathrm{rad\,mm^{-1}}$. After a distance, the obstructed BG mode demonstrated a restored structure, while the LG mode showed no self-healing. The BG field reconstructed after $z_{\min}$ as expected.

The setup was then returned to the down-conversion mode (both SMFs were connected to their respective detectors) to investigate the effects of the obstruction on two-photon quantum correlations. As OAM is conserved in SPDC[5], we chose to first project the signal and idler photons into the $|\ell = \pm 2\rangle$ basis elements, respectively. The coincidence count rate of this BG state, unobstructed, was measured to be $\sim 140\ \mathrm{s^{-1}}$. The obstruction was initially inserted 5 mm after the β-barium borate (BBO) crystal, the closest it could be placed owing to the size of the crystal housing, and moved in subsequent intervals of 5 mm away from the crystal. Slight adjustments were made to the position of the obstruction until a minimum count rate was measured, causing the coincidence levels to be reduced to background levels. At each position coincidences were recorded; a comparison of the coincidence count rates for the BG and LG modes is shown in Fig. 5. The count rate for the BG mode increased significantly after a distance of 25 mm, which is consistent with our calculation of $z_{\min} = 29$ mm. Conversely, the count rates for the LG mode showed no measurable change with distance, illustrating the unique self-healing property of BG modes. The coincidence count rate of the BG mode was not restored to the original, unobstructed rate, as there is a loss due to the obstacle. This is also consistent with the classical scenario where the self-healed BG beam has proportionally less energy after the obstacle than before.

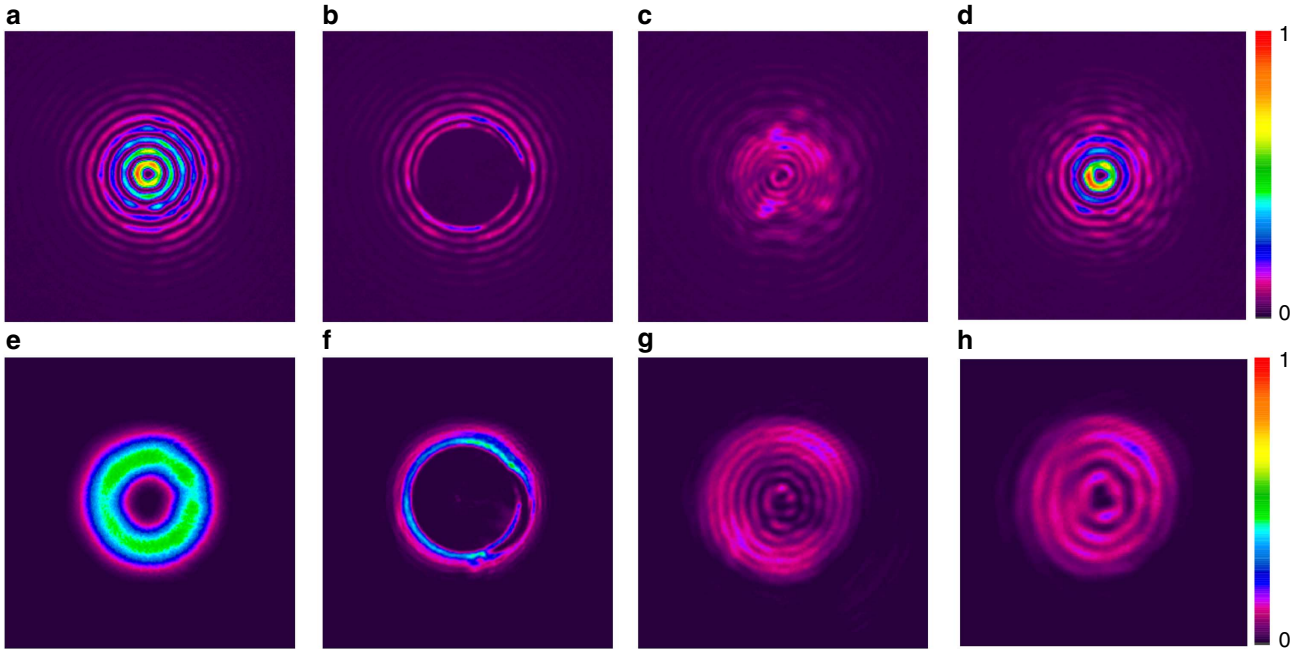

Figure 3 | CCD images of the crystal plane for different on-axis obstruction positions. Images for a BG mode (**a**–**d**) and an LG mode (**e**–**h**) with the azimuthal index $\ell = 2$. The unobstructed modes are shown in (**a**) and (**e**). The obstruction was first placed at the plane of the crystal, which is clearly shown in both (**b**) and (**f**). It was then moved 20 mm away from the crystal plane, shown in (**c**) and (**g**). The final images, (**d**) and (**h**), were taken 50 mm away from the crystal. It is clear the BG mode has reformed at 50 mm, while the LG mode has not resumed its original structure.

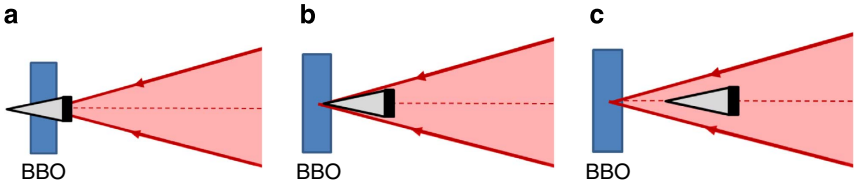

Figure 4 | Movement of the obstruction within the Bessel region. Consider the back-projected beam reflecting off the SLM onto the BBO crystal. The Bessel hologram on the SLM creates a beam with a particular cone angle. (**a**) The obstruction is at the closest position to the crystal, resulting in a clear shadow region falling on the crystal. (**b**) The obstruction is moved away from the crystal, reducing the shadow region. (**c**) The obstruction is moved further away such that the shadow region no longer falls on the crystal and a recovered BG image is seen (Fig. 3d).

Measuring the degree of entanglement. The recovery of the BG coincidence count rate does not in itself give an indication of the effects the obstruction has on the degree of entanglement of the state. To investigate the measured degree of entanglement, we first performed a Bell-type inequality experiment on the reformed state with the obstruction located 45 mm from the crystal to test for quantum correlations. The superposition of OAM states, also known as sector states, for $|\ell = \pm 2\rangle$ subspace were rotated on each SLM[35] and the corresponding coincidence count rates were recorded, shown in Fig. 6a.

From the count rates we calculated the CHSH-Bell parameter to be $S = 2.78 \pm 0.04$, which is a clear violation of the CHSH-Bell inequality[36]. This value of S can be compared with the unobstructed value of $S = 2.79 \pm 0.03$. The low coincidence count rate recorded when the obstruction was 5 mm from the crystal resulted in a low-contrast Bell curve, from which the S parameter could not be calculated. This prompted us to perform a full-state tomography experiment[37] to determine the degree of entanglement of the state. Figure 7 shows the real and imaginary parts of the reconstructed density matrices for dimensions $d = 2$ for $|\ell = \pm 2\rangle$ and $d = 4$ for $|\ell = \{-2, -1, 1, 2\}\rangle$. The unobstructed density matrices for $d = 2$ and $d = 4$ are shown in Fig. 7a,d, respectively. When the obstruction is placed near the crystal, the density matrices in both cases change significantly such that the inner dominant probabilities are reduced and the outer terms become non-zero, Fig. 7b,e. However, once the obstruction is moved beyond the $z_{\min}$ distance, both density matrices return to their original form (Fig. 7c,f).

From the density matrices, the concurrence of the state was calculated. Concurrence is a measure of entanglement, with a range from 0 (no entanglement) to 1 (maximally entangled)[38]. The concurrence can only be calculated for two-dimensional subspaces, so we considered two different OAM subspaces, $|\ell = \pm 2\rangle$ and $|\ell = \pm 4\rangle$, to demonstrate that the self-healing property holds for higher OAM modes. The unobstructed BG mode for subspace $|\ell = \pm 2\rangle$ ($|\ell = \pm 4\rangle$) generated an average quantum contrast (see Methods) of $QC = 43.2 \pm 2.0$ ($QC = 41.7 \pm 2.0$) and a concurrence of $C = 0.95 \pm 0.02$ ($C = 0.94 \pm 0.02$). When the obstruction was placed 5 mm from the crystal, the concurrence dropped to $C = 0.40 \pm 0.02$ ($C = 0.43 \pm 0.02$), but recovered to a value of $C = 0.94 \pm 0.02$ ($C = 0.91 \pm 0.02$) at 50 mm from the crystal. The results for the coincidences, quantum contrast and concurrence of the $|\ell = \pm 2\rangle$-entangled photons are shown in Fig. 8a–c, respectively. All three graphs display similar trends, where the values increase after a minimum distance represented by the

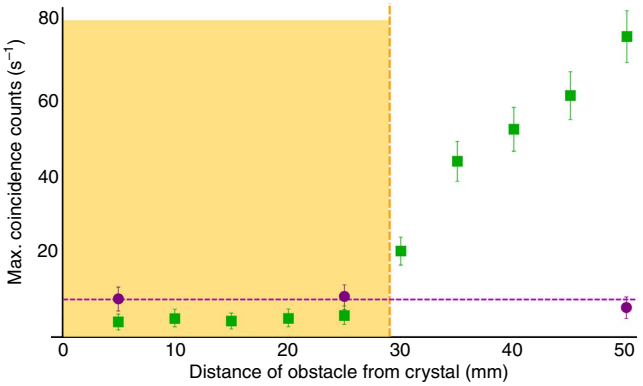

Figure 5 | Effect of an obstacle on the coincidence count rate. Measured coincidence count rates as a function of the position of the obstruction after the BBO crystal for a BG (green squares) and LG (purple circles) mode for $|\ell = \pm 2\rangle$ subspace. The BG mode with $k_r = 30\,\mathrm{rad\,mm^{-1}}$ is expected to reconstruct after an obstruction with radius, $R = 200\,\mu\mathrm{m}$, after a distance of 29 mm (yellow dashed line). The coincidence count rate remains consistently low when measured in the LG basis (purple dashed line). The count rates were averaged over a set of 10 measurements, each taken over an integration period of 5 s. Errors were estimated assuming Poisson statistics for the photon counts given as an s.d.

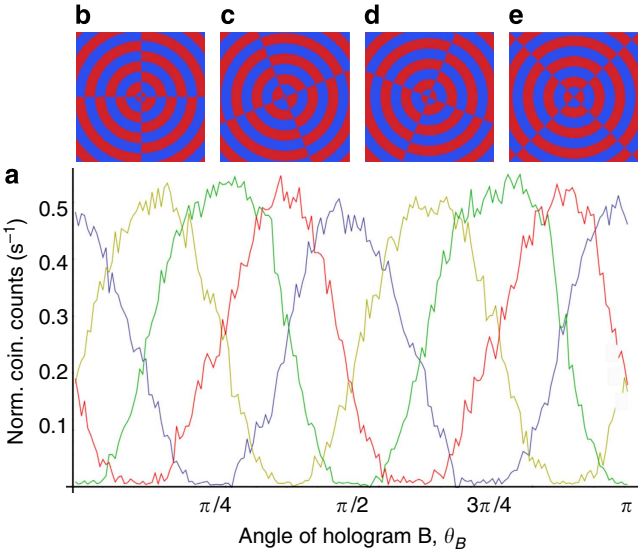

Figure 6 | CHSH-Bell measurements. (**a**) Normalized coincidence count rate as a function of the orientation of the hologram on SLM B. The hologram on SLM A was oriented at four different angles: 0 rad (blue curve), $\pi/8$ rad (yellow curve), $\pi/4$ rad (green curve) and $3\pi/8$ rad (red curve). The measured count rates were normalized by the denominator in equation (5). The typical sinusoidal Bell curve was measured with the obstruction placed in the propagation path at 45 mm from the crystal. Examples of the binary Bessel holograms ($|\ell = \pm 2\rangle$) used to perform a CHSH-inequality experiment are shown in the insets (**b**–**e**).

yellow dashed line. As in the classical case, where energy is lost in the recovered field, the coincidence counts also do not fully recover to the original unobstructed rate. Consequently, the recovered quantum contrast does not return to the unobstructed value, as the accidental count rate remains fairly constant with the insertion of the obstruction.

From the high-dimensional density matrices in Fig. 7, we calculated the fidelity of the states. Fidelity is a measure of how close the measured state is to a maximally entangled state, where a perfectly entangled state will have a fidelity of unity with the maximally entangled state. We have extended this demonstration to higher dimensions by reconstructing the density matrices for dimension $d = 4$, where $|\ell = \{-2, -1, 1, 2\}\rangle$. The reconstruction process via full-state tomography is time consuming and thus only one high-dimensional state was chosen. The density matrices for different placements of the obstruction are shown in Fig. 7d–f. Table 1 shows the fidelity measurements recorded at different positions of the obstruction from the crystal.

The measured fidelities for both dimensions recover to their relative unobstructed values. Fidelity decreases as the state dimension increases, however, the recovered fidelity for $d = 4$ lies above the threshold states, which are defined by the minimum probability for which a high-dimensional Bell inequality is violated[39].

We have therefore demonstrated that the self-healing property of Bessel beams, even when applied to single photons, can overcome the losses associated with an obstruction, allowing sufficient measurement of the spatial correlations to reveal the quantum entanglement of the photon pairs.

Discussion

Our results show that by making projective measurements in the BG basis, we were able to recover the reduction in the measured degree of entanglement resulting from the losses introduced by the obstruction. By comparison, when the LG measurement basis is chosen, the entanglement is not recovered. From the density matrices, we see that while the obstruction perturbs the system, when measured beyond the minimum self-healing distance, the density matrix reverts to the original unobstructed form. Comparing the graphs of the coincidence count rates and concurrence in both experiments, we observe a similar trend: the degree of entanglement is low for low coincidence count rates and then increases with the count rate. It appears that the off-axis obstruction does not destroy the entanglement by scattering a particular OAM state into many OAM states, as observed in turbulence-related experiments[20], but rather decreases the measured degree of entanglement by reducing the two-photon count rates to background levels. For completeness, we also measured the response of an unobstructed BG mode in the presence of attenuation. By rotating a polarizer in the path of the down-converted light the transmission of the photons could be varied from background levels (≈ 0 transmission) to normal conditions (transmission of 1). The coincidence count rate, quantum contrast and concurrence for various transmission values are shown in Fig. 8d–f, respectively. The quantum contrast (Fig. 8b) suggests that the obstacle blocks one of the entangled photons, thus diminishing the coincidence rate but maintaining a high single-photon count rate. However, the attenuated quantum contrast remains fairly constant unlike that of the obstructed beam. The attenuation reduced the count rates for both the single and coincidence counts proportionally, thereby maintaining a constant quantum-contrast ratio. The obstruction on the other hand reduced only the coincidence count rate and in turn the quantum contrast. The entanglement is therefore obscured by the noise. The correlations are recovered beyond the minimum distance after the obstacle because the mode itself recovers, thus increasing the signal at the detector because of an improved overlap between the hologram and the projected mode. Interestingly, the measurement choice is made after the photons have encountered the obstacle. By contrast, in a classical experiment, the mode is chosen or generated before interacting with the obstacle.

In conclusion, we have exploited the self-healing property of BG modes in a quantum entanglement experiment to recover the

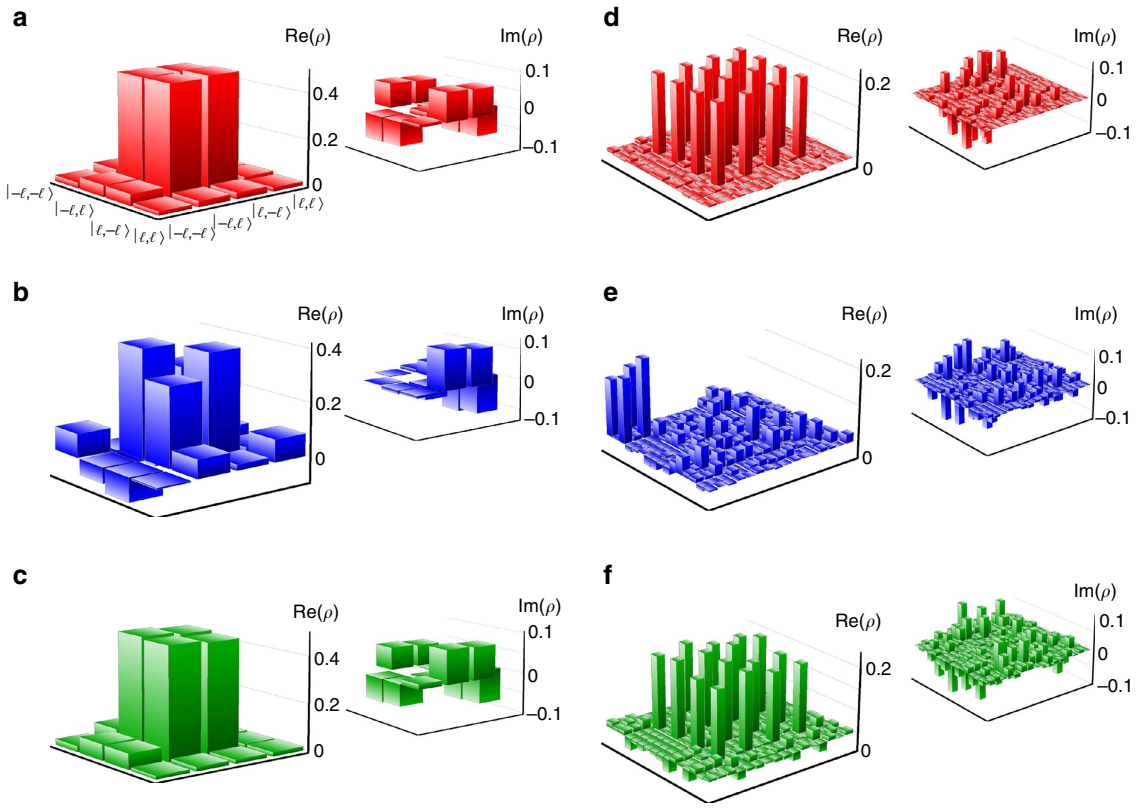

Figure 7 | Reconstructed density matrices from full-state tomography measurements. The density matrices are shown for dimensions $d = 2$ (**a**–**c**) and $d = 4$ (**d**–**f**). Real and imaginary parts of the reconstructed density matrices for (**a**) and (**d**) no obstruction, (**b**) and (**e**) obstruction placed 5 mm from the crystal, and (**c**) and (**f**) obstruction placed 45 mm from the crystal. It is clear that the density matrix recovers to the original unobstructed form for a two-dimensional state as well as higher-dimensional states. The density matrices were calculated by measuring an over-complete set of modes and applying a maximum-likelihood estimation using a least-squares fit to the measurements. This optimization technique ensures a density matrix with non-negative eigenvalues and a trace of unity.

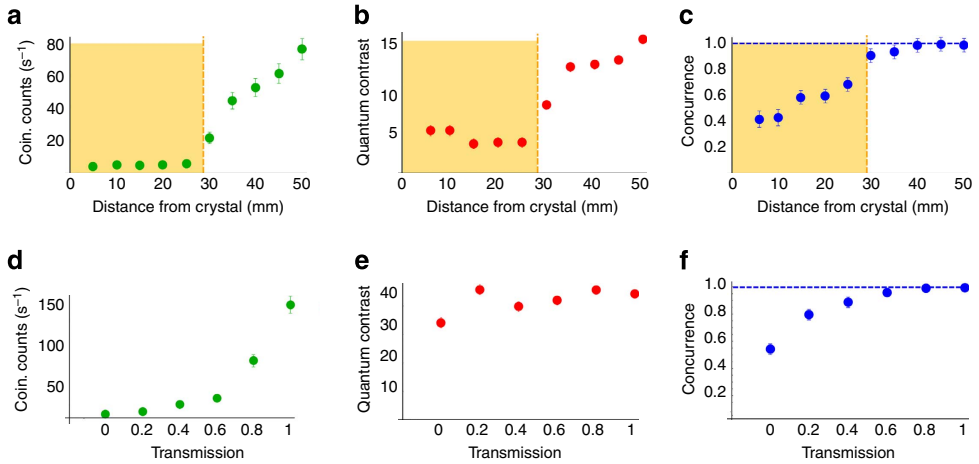

Figure 8 | Comparison between an obstructed and attenuated beam. Measurements of the coincidence count rate, quantum contrast and concurrence of obstructed (**a**–**c**) and attenuated (**d**–**f**) entangled photons for $|\ell = \pm 2\rangle$. The obstruction was moved in 5 mm intervals along the propagation axis, at which the measurements were recorded. The dashed yellow line represents z_{min}, the calculated distance at which recovery is expected (recovery is not expected within the yellow shaded region). A polarizer was rotated to attenuate the coincidence count rate and vary the degree of transmission from 0 (background levels) to 1 (unattenuated and unobstructed). The coincidence count rates and quantum contrast represent the average of 10 measurements. The average error for the concurrence is ± 0.01, which is calculated by generating additional data sets by adding $\sqrt{C_i}$ fluctuations to the measured coincidence counts C_i and then repeating the concurrence calculations described in the text. The unobstructed concurrence value is represented by the blue dashed lines.

reduction in the measured degree of entanglement. We showed that the coincidence count rate is reduced in the presence of an obstacle, but that the count rate recovers after a particular distance owing to the self-healing feature of BG modes. This trend was similarly reported for the degree of entanglement of the quantum state, where the concurrence of the obstructed mode

Table 1 | Measured fidelity at different obstacle positions from the crystal.

Dimension	5 mm	15 mm	30 mm	50 mm	Unobstructed
2 ($\|\ell = \pm 2\rangle$)	0.24	0.59	0.79	0.96	0.97
4	0.20	0.45	0.68	0.75	0.79

returned to its original, unobstructed value. These results may be useful for quantum key distribution and quantum communication systems, where preservation of entanglement over long distances and in the presence of an obstruction is crucial.

Methods

Experimental details. The laser source was a mode-locked ultraviolet laser (Vanguard 355–2500) with a modal diameter of 1 mm, producing pulses of ~10 ps at a repetition rate of 80 MHz. The BBO crystal was cut at 33° to produce collinear, frequency-degenerate down-converted photon pairs at 710 nm. The crystal was tilted to produce near-collinear down-conversion. An interference filter or bandpass filter centred at 710 nm was used to reflect the pump light and transmit the down-converted photon pairs. The variable aperture acted as a spatial filter of the higher-order diffraction modes. The projective measurements were performed by the HoloEye Pluto SLMs (1,080 × 1,920 pixels), which have a resolution of 8 μm per pixel and were calibrated for near-infrared wavelengths. Additional interference filters were placed before the SMFs to select only the photons at 710 nm. Each SMF has a modal radius of 2.3 μm. The Perkin Elmer APDs have a dark count of 200 s^{-1}, which were connected to a coincidence counter with a gating time of 12.5 ns. The back-projection experiment made use of a 705-nm diode (Laser 2000), temperature tuned to 710 nm. The images of the obstructed beams were captured on a CCD camera.

CHSH *S* parameter. The CHSH-Bell parameter, as defined in Leach *et al.*[35], is given by

$$S = E(\theta_A, \theta_B) - E(\theta_A, \theta'_B) + E(\theta'_A, \theta_B) - E(\theta'_A, \theta'_B), \quad (4)$$

where

$$E(\theta_A, \theta_B) = \frac{C(\theta_A, \theta_B) + C(\theta_A + \frac{\pi}{2\ell}, \theta_B + \frac{\pi}{2\ell}) - C(\theta_A + \frac{\pi}{2\ell}, \theta_B) - C(\theta_A, \theta_B + \frac{\pi}{2\ell})}{C(\theta_A, \theta_B) + C(\theta_A + \frac{\pi}{2\ell}, \theta_B + \frac{\pi}{2\ell}) + C(\theta_A + \frac{\pi}{2\ell}, \theta_B) + C(\theta_A, \theta_B + \frac{\pi}{2\ell})}, \quad (5)$$

with $C(\theta_A,\theta_B)$ being the coincidence count rate for the particular orientation of each hologram. By calculating the propagation of uncertainty, we were able to compute a s.d. for the *S* parameters.

Calculating quantum contrast. Quantum contrast is a ratio of the coincidence count rate with the accidental count rate. The accidental count rate is defined as $S_A S_B \Delta t$, where $S_{A,B}$ is the single-count rate in arm A(B) and Δt is the gating time of the coincidence counter. Thus we can write the quantum contrast as $QC = C/S_A S_B \Delta t$, where C is the coincidence count rate.

Calculating concurrence. The concurrence is given by $C(\rho) = \max\{0, \lambda_1 - \lambda_2 - \lambda_3 - \lambda_4\}$, where λ_i are the eigenvalues, in decreasing order, of the Hermitian matrix $\sqrt{\sqrt{\rho}\tilde{\rho}\sqrt{\rho}}$, where $\tilde{\rho}$ is the spin-flipped state of the density matrix ρ. The qubit OAM density matrices consist of 16 elements, which were calculated by performing a full-state tomography, consisting of 36 projective measurements. That is, the probability of simultaneously finding each of the photons (in the entangled pair) in one of six non-orthogonal states was measured. Although only 16 measurements are required to reconstruct the two-dimensional density matrix, the over-complete 36 measurements allow a least-squares fit to be performed.

Calculating fidelity. The fidelity is defined as

$$F = \left[\mathrm{Tr}\left\{\left(\sqrt{\rho_T}\rho_d\sqrt{\rho_T}\right)^{1/2}\right\}\right]^2, \quad (6)$$

which is a measure of how close our d-dimensional reconstructed state, ρ_d, is to the target state $\rho_T = |\psi_T\rangle\langle\psi_T|$. In our case the target state is the (pure) maximally entangled state, $|\psi_T\rangle = \sum_\ell c_\ell |\ell\rangle_s |-\ell\rangle_i$, where ℓ ranges over d different values and $c_\ell = 1/\sqrt{d}$ represents the expansion coefficients.

References

1. Yao, A. & Padgett, M. Orbital angular momentum: origins, behavior and applications. *Adv. Opt. Photon* **3,** 161–204 (2011).
2. Allen, L., Beijersbergen, M. W., Spreeuw, R. J. C. & Woerdman, J. P. Orbital angular momentum of light and the transformation of Laguerre-Gaussian laser modes. *Phys. Rev. A* **45,** 8185–8189 (1992).
3. Simpson, N., Allen, L. & Padgett, M. Optical tweezers and optical spanners with laguerre-gaussian modes. *J. Mod. Opt.* **43,** 2485–2491 (1996).
4. Sztul, H. & Alfano, R. Double-slit interference with Laguerre–Gaussian beams. *Opt. Lett.* **31,** 999–1001 (2006).
5. Mair, A., Vaziri, A., Weihs, G. & Zeilinger, A. Entanglement of the orbital angular momentum states of photons. *Nature* **412,** 313–316 (2001).
6. Krenn, M. *et al.* Entangled singularity patterns of photons in ince-gauss modes. *Phys. Rev. A* **87,** 012326 (2013).
7. McLaren, M. *et al.* Entangled Bessel-Gaussian beams. *Opt. Express* **20,** 23589–23597 (2012).
8. McLaren, M., Romero, J., Padgett, M., Roux, F. & Forbes, A. Two-photon optics of bessel-gaussian modes. *Phys. Rev. A* **88,** 033818 (2013).
9. Giovannini, D. *et al.* Characterization of high-dimensional entangled systems via mutually unbiased measurements. *Phys. Rev. Lett.* **110,** 143601 (2013).
10. Mafu, M. *et al.* Higher-dimensional orbital angular momentum based quantum key distribution with mutually unbiased bases. *Phys. Rev. A* **88,** 032305 (2013).
11. Dada, A., Leach, J., Buller, G., Padgett, M. & Andersson, E. Experimental high-dimensional two-photon entanglement and violations of the generalized Bell inequalities. *Nat. Phys.* **7,** 677–680 (2011).
12. Scarani, V. *et al.* The security of practical quantum key distribution. *Rev. Mod. Phys.* **81,** 1301–1350 (2009).
13. Nagali, E. & Sciarrino, F. Generation of hybrid polarization-orbital angular momentum entangled states. *Opt. Express* **18,** 18243–18248 (2010).
14. Yu, T. & Eberly, J. Sudden death of entanglement. *Science* **323,** 598–601 (2009).
15. Kielpinski, D. *et al.* A decoherence-free quantum memory using trapped ions. *Science* **291,** 1013–1015 (2001).
16. Viola, L. *et al.* Experimental realization of noiseless subsystems for quantum information processing. *Science* **293,** 2059–2063 (2001).
17. Giovannini, D., Nagali, E., Marrucci, L. & Sciarrino, F. Resilience of orbital-angular-momentum photonic qubits and effects on hybrid entanglement. *Phys. Rev. A* **83,** 042338 (2011).
18. Morikoshi, F. Recovery of entanglement lost in entanglement manipulation. *Phys. Rev. Lett.* **84,** 3189–3192 (2000).
19. Patterson, C. Atmospheric turbulence and orbital angular momentum of single photons for optical communication. *Phys. Rev. Lett.* **94,** 153901 (2005).
20. Ibrahim, A. H., Roux, F., McLaren, M., Konrad, T. & Forbes, A. Orbital-angular-momentum entanglement in turbulence. *Phys. Rev. A* **88,** 012312 (2013).
21. Zhao, S., Leach, J., Gong, L., Ding, J. & Zheng, B. Aberration corrections for free-space optical communications in atmosphere turbulence using orbital angular momentum states. *Opt. Express* **20,** 452–461 (2011).
22. Brünner, T. & Roux, F. Robust entangled qutrit states in atmospheric turbulence. *New J. Phys.* **15,** 063005 (2013).
23. Rodenburg, B. *et al.* Simulating thick atmospheric turbulence in the lab with application to orbital angular momentum communication. Preprint at http://arxiv.org/abs/1301.7454 (2013).
24. McGloin, D., Garcés-Chávez, V. & Dholakia, K. Interfering bessel beams for optical micromanipulation. *Opt. Lett.* **28,** 657–659 (2003).
25. Litvin, I., McLaren, M. & Forbes, A. A conical wave approach to calculating Bessel–Gauss beam reconstruction after complex obstacles. *Opt. Commun.* **282,** 1078–1082 (2009).
26. Durnin, J. Exact solutions for nondiffracting beams. i. the scalar theory. *J. Opt. Soc. Am. A* **4,** 651–654 (1987).
27. McGloin, D. & Dholokia, K. Bessel beams: diffraction in a new light. *Contemp. Phys.* **46,** 15–28 (2012).
28. Gori, F., Guattari, G. & Padovani, C. Bessel-Gauss beams. *Opt. Commun.* **64,** 491–495 (1987).
29. Cruz-Ramírez, H. *et al.* Observation of non-diffracting behavior at the single-photon level. *Opt. Express* **20,** 29761–29768 (2012).
30. Durnin, J., Miceli, Jr J. & Eberly, J. Diffraction-free beams. *Phys. Rev. Lett.* **58,** 1499–1501 (1987).
31. Bouchal, Z., Wagner, J. & Chlup, M. Self-reconstruction of a distorted nondiffracting beam. *Opt. Commun.* **151,** 207–211 (1998).
32. Turunen, J., Vasara, A. & Friber, A. Holographic generation of diffraction-free beams. *App. Opt.* **27,** 3959–3962 (1988).
33. Cottrell, D., Craven, J. & Davis, J. Nondiffracting random intensity patterns. *Opt. Lett.* **32,** 298–300 (2007).
34. Klyshko, D. A simple method of preparing pure states of an optical field, of implementing the Einstein–Podolsky–Rosen experiment, and of demonstrating the complementarity principle. *Sov. Phys. Usp.* **31,** 74–85 (1988).
35. Leach, J. *et al.* Violation of a Bell inequality in two-dimensional orbital angular momentum state-spaces. *Opt. Express* **17,** 8287–8293 (2009).

36. Clauser, J., Horne, M., Shimony, A. & Holt, R. Proposed experiment to test local hidden-variable theories. *Phys. Rev. Lett.* **23,** 880–884 (1969).
37. Jack, B., Leach, J., Ritsch, H., Barnett, S. & Padgett, M. Precise quantum tomography of photon pairs with entangled orbital angular momentum. *New J. Phys.* **811,** 103024 (2009).
38. Hill, S. & Wootters, W. Entanglement of a pair of quantum bits. *Phys. Rev. Lett.* **78,** 5022–5025 (1997).
39. Collins, D., Gisin, N., Linden, N., Massar, S. & Popescu, S. Bell inequalities for arbitrarily high-dimensional systems. *Phys. Rev. Lett.* **88,** 040404 (2002).

Acknowledgements

M.M. would like to thank A. Hamadou Ibrahim for useful discussions.

Author contributions

M.J.P. and A.F. conceived the experiment. M.M., T.M. and A.F. designed and performed the experiment. M.M., T.M., M.J.P., F.S.R. and A.F. analysed the results. All authors contributed to the writing of the manuscript.

Additional information

Competing financial interests: The authors declare no competing financial interests.

Reprints and permission information is available online at http://npg.nature.com/reprintsandpermissions/

How to cite this article: McLaren, M. *et al.* Self-healing of quantum entanglement after an obstruction. *Nat. Commun.* 5:3248 doi: 10.1038/ncomms4248 (2014).

Generating and measuring nondiffracting vector Bessel beams

Angela Dudley,[1] Yanming Li,[2] Thandeka Mhlanga,[1,3] Michael Escuti,[2] and Andrew Forbes[1,3,*]

[1]*CSIR National Laser Centre, P.O. Box 395, Pretoria 0001, South Africa*

[2]*Department of Electrical and Computer Engineering, North Carolina State University, Raleigh, North Carolina 27695, USA*

[3]*School of Physics, University of KwaZulu-Natal, Private Bag X54001, Durban 4000, South Africa*

**Corresponding author: AForbes1@csir.co.za*

Received June 26, 2013; revised August 1, 2013; accepted August 4, 2013;
posted August 7, 2013 (Doc. ID 192892); published August 29, 2013

Nondiffracting vector Bessel beams are of considerable interest due to their nondiffracting nature and unique high-numerical-aperture focusing properties. Here we demonstrate their creation by a simple procedure requiring only a spatial light modulator and an azimuthally varying birefringent plate, known as a *q*-plate. We extend our control of both the geometric and dynamic phases to perform a polarization and modal decomposition on the vector field. We study both single-charged Bessel beams as well as superpositions and find good agreement with theory. Since we are able to encode nondiffracting modes with circular polarizations possessing different orbital angular momenta, we suggest these modes will be of interest in optical trapping, microscopy, and optical communication.

OCIS codes: (140.3295) Laser beam characterization; (090.1995) Digital holography; (050.2770) Gratings; (050.4865) Optical vortices.

http://dx.doi.org/10.1364/OL.38.003429

There has been considerable interest of late in optical modes of spatially inhomogeneous polarization states, for example cylindrical symmetric polarization, commonly referred to as cylindrical vector (CV) beams [1–4] that includes radially and azimuthally polarized light, and a linear superposition of the two to form generalized cylindrical polarization. In the cross-sectional profile of these CV beams, the local polarization state is linearly polarized at different orientations, resulting in them occupying the equator on the Poincaré sphere. Recently a more general type of vector beam [full Poincaré (FP) beams] has been proposed and demonstrated [5,6] where the local polarization state spans the entire surface of the Poincaré sphere. Various generation methods of CV and FP beams have been developed from laser gain media [7,8], optical fibers [9], radial polarization converters [10,11], liquid crystal displays [12], *q*-plates [13], and interferometric methods [14]. CV beams exhibit unique properties under high numerical-aperture focusing giving rise to the realization of tighter focal spots [15–18] resulting in applications in spectroscopy, particle acceleration, microscopy, optical trapping, and interferometry [1–4]. These beams have interesting propagation characteristics: in free space due to the manifestation of the universal form of the Gouy phase of astigmatic wave fields [19] and have been shown to be more resilient to atmospheric turbulence [20].

It is also possible to generate such vector beams as vector–vortex beams. Scalar vortex fields carry orbital angular momentum (OAM) and have an azimuthal angular dependence of $\exp(i\ell\theta)$ where ℓ is the azimuthal index and θ is the azimuthal angle. One such example of propagation-invariant scalar modes which are OAM carriers are higher-order Bessel beams [21,22]. Experimental studies into the generation of diffraction-limited vector beams have remained somewhat limited with reports on the use of subwavelength gratings [23], polarization grating (PG) axicons [24], quantized Pancharatnam Berry phase elements in conjugation with an axicon [25], and interferometric techniques [26,27].

In this Letter, we present a new procedure for the generation and measurement of nondiffracting vector Bessel beams. We control both the dynamic and geometric phase, using a spatial light modulator (SLM) and *q*-plate, to convert arbitrary incoming scalar fields into nondiffracting vector fields. We simultaneously detect both the polarization and azimuthal components of our vector Bessel beam by implementing a PG in conjugation with a second SLM to perform a polarization selective azimuthal modal decomposition. Although this technique is outlined with Bessel beams as the spatial modes, it can easily be extended to other OAM-carrying modes.

We illustrate the concept for both the generation and measurement of vector Bessel beams with the aid of Fig. 1. To generate arbitrary superpositions of scalar Bessel beams an expanded HeNe laser beam ($\lambda \sim 633$ nm) was directed onto the first SLM (SLM1). These fields were generated in a similar approach to Durnin's ring-slit aperture method [21], implemented digitally [22] on SLM1 (HoloEye, PLUTO-VIS, with

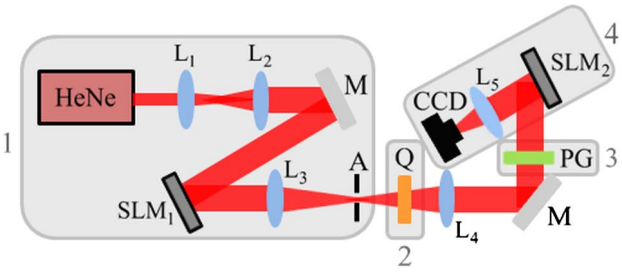

Fig. 1. Schematic of the experimental setup [division 1, scalar generation; division 2, vector generation; division 3, vector decomposition; division 4, scalar (azimuthal) decomposition]. L, lens ($f1 = 15$ mm, $f2 = 150$ mm, $f3$ and $f4 = 500$ mm, $f5 = 300$ mm); SLM, spatial light modulator; A, aperture; *Q*, *q*-plate; PG, polarization grating; CCD, camera.

1920×1080 pixels of pitch 8 μm and calibrated for a 2π phase shift at ~633 nm) with the use of complex amplitude modulation [28–30]. Mathematically we may describe such a generalized superposition of Bessel beams as

$$u(r,\phi,z=0)=\sum_{\ell}J_{\ell}(k_r r)\exp(i\ell\phi)\begin{pmatrix}1\\1\end{pmatrix}, \quad (1)$$

where $J_\ell(\cdot)$ is the Bessel function of the first kind, k_r is the transverse wave vector and the Jones vector denotes linear polarization. To convert this scalar field into a CV field, we introduce in the second step (2) an azimuthally varying birefringent plate, known as a q-plate, which couples OAM to spin angular momentum through the transformation

$$\begin{pmatrix}\cos(Q\phi)\sin(Q\phi)\\ \sin(Q\phi)-\cos(Q\phi)\end{pmatrix}\begin{pmatrix}1\\1\end{pmatrix}\exp(i\ell\phi)$$
$$\rightarrow \exp(i(\ell+Q)\phi)\begin{pmatrix}1\\-i\end{pmatrix}+\exp(i(\ell-Q)\phi)\begin{pmatrix}1\\i\end{pmatrix}, \quad (2)$$

where the first matrix corresponds to the Jones matrix for a q-plate [31] and Q is the azimuthal charge introduced by the q-plate ($Q=2q$). The two vectors correspond to right- and left-circular polarization, respectively. The action of the q-plate [given by the Jones matrix in Eq. (2)] can be represented in bra–ket notation as follows: $|\ell,L\rangle \rightarrow |\ell+Q,R\rangle$ and $|\ell,R\rangle \rightarrow |\ell-Q,L\rangle$, where R and L represent right- and left-circular polarization, respectively. The q-plate was manufactured as a polymerizable liquid crystal film on a glass substrate, whose spatial variation of the optical axis was realized by photoaligning the local director of the liquid crystalline material with UV light [32,33]. The UV light was shaped to a narrow stripe which was exposed onto the sample azimuthally with a rotating linear polarization. The concept of this coupling of angular momenta is shown in Fig. 2(a), where an experimentally generated circularly polarized Gaussian beam is converted into an oppositely handed vortex beam. The optical field after the q-plate ($Q=1$) was therefore a vector Bessel beam described by $u \propto |\ell+1,R\rangle + |\ell-1,L\rangle = \exp(i\ell\phi)[|1,R\rangle + |-1,L\rangle]$, which we note is a radial polarized state since

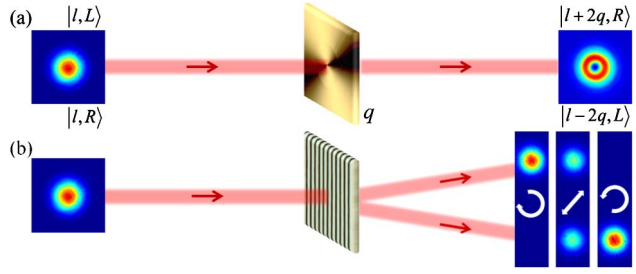

Fig. 2. (a) Transform of a q-plate with corresponding state equations. (b) The action of a PG with the incoming polarization marked in the corresponding outputs.

$$|1,R\rangle + |-1,L\rangle = \exp(i\phi)\begin{pmatrix}1\\-i\end{pmatrix}+\exp(-i\phi)\begin{pmatrix}1\\i\end{pmatrix}$$
$$=\begin{pmatrix}\cos(\phi)\\ \sin(\phi)\end{pmatrix}. \quad (3)$$

To perform a modal decomposition on the vector vortex beam we again exploit both the dynamic and geometric phases. We employ a PG with a period of 8.3 μm, which acts as a polarizing beam splitter for left- and right-circular polarization, to split the field into its two spin components (step 3 in Fig. 1), and also shown in Fig. 2(b). The process for manufacturing the PG is similar to that for the q-plate; however, a polarization holography setup was used where the sample was exposed with the interference of two plane waves each of opposite circular polarization [33,34]. With the vector beam projected into two path-dependent scalar beams, we finally perform a modal decomposition on each to reconstruct the full vector vortex beam. We consider the modal decomposition of our input field E into azimuthal modes $\exp(i\ell\phi)$ so that $E=\sum_\ell c_\ell \exp(i\ell\phi)$. The modal weighting coefficients c_ℓ may be found by the inner product of the field with an azimuthal match filter, $|\langle E|\exp(i\ell\phi)\rangle| = c_\ell$. The inner product was executed experimentally by directing the modes onto the match filter, encoded on SLM2 and viewing the Fourier transform, with the use of lens L3, on the CCD (Spiricon BeamGage, SP620U). SLM2 is also only responsive to horizontally polarized modes. However, since the horizontal component is present in both left- and right-circular polarizations, we need not introduce additional polarization optics. The PG was aligned appropriately so that the port containing the left-circular polarization modes were incident on SLM2 so as to extract their azimuthal modes. Later, the PG was adjusted to direct the right-circular polarization modes onto SLM2 for the execution of their azimuthal decomposition. We point out that this could be done in a single step by directing both components to adjacent sectors of SLM2.

Scalar Bessel beams as well as superpositions thereof were created with SLM1, with near- and far-field images shown in the top row of Fig. 3. Figure 3(a) shows a

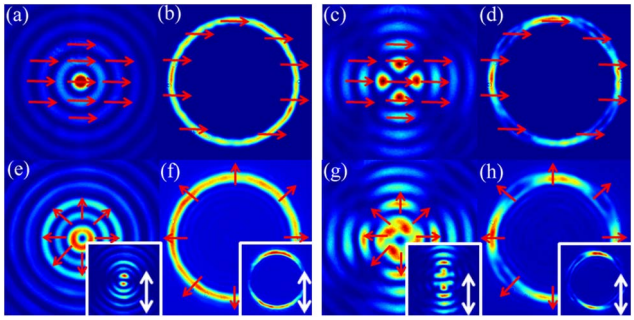

Fig. 3. Experimentally recorded near- and far-field intensity profiles of (a) and (b) the scalar single-charged Bessel beam of azimuthal index $\ell=0$; (c) and (d) superposition of azimuthal indices $\ell=-2$ and $+2$. (e)–(h) Experimental near-field [(e) and (g)] and far-field [(f) and (h)] intensity profiles of the corresponding vector Bessel fields recorded after the q-plate. Insets denote the corresponding vector beams recorded with a polarizer in front of the CCD. Red (white) arrows denote the polarization direction (polarizer orientation).

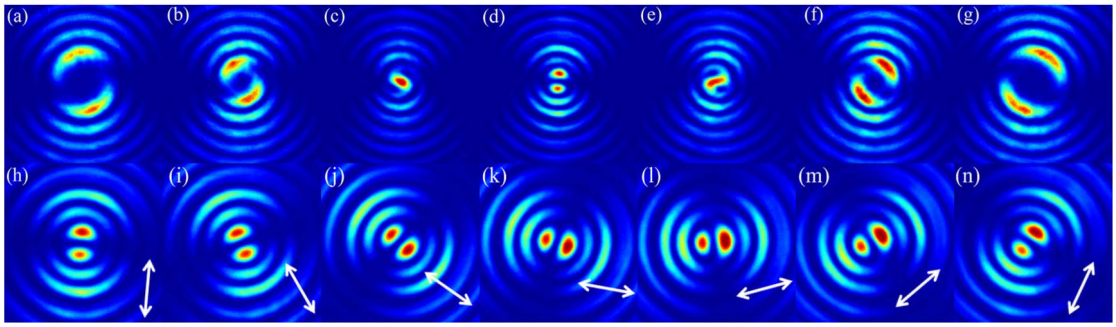

Fig. 4. (a)–(g) Experimentally recorded near-field intensity profiles of vector Bessel fields recorded after the q-plate with a polarizer in front of the CCD for initial scalar Bessel beams of $\ell = -5, -3, -1, 0, +1, +3$, and $+5$, respectively. (h)–(n) Intensity profiles for an $\ell = 0$ vector Bessel beam recorded with a rotating polarizer. The full data (video) can be viewed in Media 1. White arrows mark the corresponding polarizer setting.

zero-order Bessel beam recorded at the aperture (A) in Fig. 1 and its corresponding far-field depicted in Fig. 3(b), and similarly in Figs. 3(c) and 3(d) for a superposition of Bessel beams of azimuthal indices $\ell = -2$ and $+2$. In the case of the superposition, the azimuthal indices are of equal magnitude but opposite handedness resulting in the predicted petal structure, where the number of petals is denoted by $2|\ell|$ [22]. The fields entering the q-plate are linearly polarized (an equal weighting of left- and right-circular polarization) and so the transformation of Eq. (2) takes place: the left-circular component is converted to the right-circular component, while decreasing the azimuthal component by unit charge of OAM while the reserve procedure takes place on the right-circular component, converting it to left while simultaneously increasing the azimuthal component by unit charge of OAM ($|\ell, L\rangle \rightarrow |\ell + Q, R\rangle$ and $|\ell, R\rangle \rightarrow |\ell - Q, L\rangle$). The resulting field after the q-plate, is shown in Figs. 3(e) and 3(g). These are nondiffracting vector Bessel beams with radial polarization, as described by Eq. (3). In the case of the zero-order Bessel beam, the OAM associated with the left-circular component increases by unit charge of OAM (while the right-circular component decreases by unit charge of OAM), thus producing a superposition of two Bessel beams of azimuthal indices $\ell = -1$ and $+1$, resulting in an intensity structure with two petals ($2|\ell|$) as seen through a polarizer and shown in the insert in Fig. 3(e). Similarly, the superimposed Bessel beams of azimuthal indices $\ell = -2$ and $+2$ becomes a superimposition of Bessel beams of azimuthal indices $\ell = -3, -1, +1$, and $+3$ after the q-plate, as illustrated in Fig. 3(g). The corresponding far fields of Figs. 3(e) and 3(g) are given in Figs. 3(f) and 3(h). Here the number of line singularities in the far field is denoted by $2|\ell|$ (the same as the number of petals), as illustrated in the inserts in Figs. 3(f) and 3(h). While the aforementioned examples illustrate the technique, there is of course a myriad of choices for which vector Bessel beams to create. We show in Figs. 4(a)–4(g) additional experimental near-field images of vector Bessel fields (with a polarizer) for initial scalar beams of azimuthal indices ranging from $\ell = -5$ to $\ell = +5$. A polarizer (positioned after the q-plate) was rotated to illustrate that the intensity profile of the vector Bessel field rotates. Snapshots of the intensity profiles for a CV Bessel beam (for an initial single scalar Bessel beam of $\ell = 0$) is presented in Figs. 4(h)–4(n), illustrating the rotation of the field as the polarizer is rotated.

An azimuthal decomposition [35,36] was performed digitally on each polarization component of the generated fields and the results are depicted in Fig. 5(a) for the left- (orange) and right-circular (pink) components, respectively. The measurement of the azimuthal indices, presented in Fig. 5(a) (orange) [Fig. 5(a) (pink)], illustrates that the scalar single-charged Bessel beams incur an increase (decrease) in their OAM when passing through the q-plate, as expected from the transformation in Eq. (2). This is evident by the two rows of off-diagonal peaks, displaced from the original by ± 1. Figures 5(b) and 5(c) denote the left- and right-circular components (of azimuthal indices $\ell = +1$ and $\ell = -1$, respectively), which make up the vector vortex beam presented in Fig. 3(e).

In conclusion, we have shown an experimental realization of nondiffracting vector Bessel beams through control of both the dynamic and geometric phase. We make use of digital holograms to create custom vortex beams and exploit q-plates for the conversion into CV vortex fields. We detected the polarization of the generated field

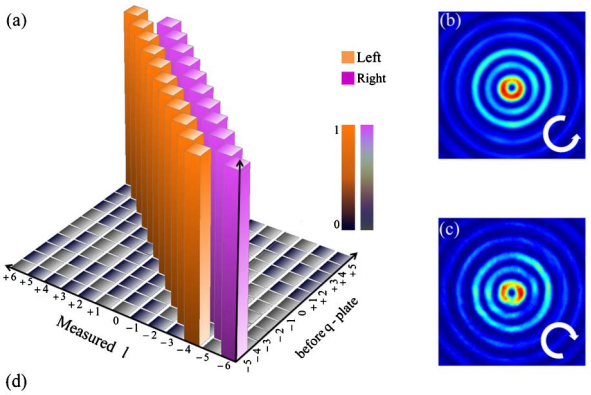

(d)

Input l:	-5	-4	-3	-2	-1	0	+1	+2	+3	+4	+5
Output l; R:	-6	-5	-4	-3	-2	-1	0	+1	+2	+3	+4
Output l; L:	-4	-3	-2	-1	0	+1	+2	+3	+4	+5	+6

Fig. 5. (a) Correlation signals for the azimuthal decomposition for both the left- (orange) and right-circular (pink) polarization components. (b) $\ell = +1$ and (c) $\ell = -1$ Bessel beams after the q-plate associated with left- and right-circular polarization components, respectively. (d) A table summarizing the transformation of the input ℓ values after the q-plate.

with the use of a PG, as well as their vortex nature by performing an azimuthal modal decomposition. In addition to their known classical applications, having the ability to simultaneously control the polarization and OAM degrees of freedom is useful in hyper-entanglement systems.

The authors acknowledge support from the U.S. National Science Foundation (NSF and ECCS-0955127) and the National Research Foundation.

References

1. Q. Zhan, Adv. Opt. Photon. **1**, 1 (2009).
2. T. G. Brown and Q. Zhan, Opt. Express **18**, 10775 (2010).
3. E. Hasman, G. Biener, A. Niv, and V. Kleiner, *Space-Variant Polarization Manipulation* (Elsevier, 2005), Vol. **47**, pp. 215–289.
4. T. G. Brown, *Unconventional Polarization States: Beam Propagation, Focusing and Imaging* (Elsevier, 2011), Vol. **56**, pp. 81–129.
5. A. M. Beckley, T. G. Brown, and M. A. Alonso, Opt. Express **18**, 10777 (2010).
6. G. Milione, H. I. Sztul, D. A. Nolan, and R. R. Alfano, Phys. Rev. Lett. **107**, 053601 (2011).
7. D. Pohl, Appl. Phys. Lett. **20**, 266 (1972).
8. Y. Mushiake, K. Matzumurra, and N. Nakajima, Proc. IEEE **60**, 1107 (1972).
9. T. Grosjean, D. Courjon, and M. Spajer, Opt. Commun **203**, 1 (2002).
10. M. Stalder and M. Schadt, Opt. Lett. **21**, 1948 (1996).
11. L. Marrucci, C. Manzo, and D. Paparo, Appl. Phys. Lett. **88**, 221102 (2006).
12. W. Han, W. Cheng, and Q. Zhan, Opt. Lett. **36**, 1605 (2011).
13. F. Cardano, E. Karimi, S. Slussarenko, L. Marrucci, C. de Lisio, and E. Santamato, Appl. Opt. **51**, C1 (2012).
14. C. Maurer, A. Jesacher, S. Fürhapter, S. Bernet, and M. Ritsch-Marte, New J. Phys. **9**, 78 (2007).
15. S. Quabis, R. Dorn, M. Eberler, O. Glöckl, and G. Leuchs, Opt. Commun. **179**, 1 (2000).
16. R. Dorn, S. Quabis, and G. Leuchs, Phys. Rev. Lett. **91**, 233901 (2003).
17. B. Jia, X. Gan, and M. Gu, Opt. Express **13**, 6821 (2005).
18. B. Hao and J. Leger, Opt. Express **15**, 3550 (2007).
19. G. M. Philip, V. Kumar, G. Milione, and N. K. Viswanathan, Opt. Lett. **37**, 2667 (2012).
20. W. Cheng, J. W. Haus, and Q. Zhan, Opt. Express **17**, 17829 (2009).
21. J. Durnin, J. J. Miceli, Jr., and J. H. Eberly, Phys. Rev. Lett. **58**, 1499 (1987).
22. R. Vasilyeu, A. Dudley, N. Khilo, and A. Forbes, Opt. Express **17**, 23389 (2009).
23. Z. Bomzon, A. Niv, G. Biener, V. Kleiner, and E. Hasman, Appl. Phys. Lett. **80**, 3685 (2002).
24. J. Tervo and J. Turunen, Opt. Commun. **192**, 13 (2001).
25. A. Niv, G. Biener, V. Kleiner, and E. Hasman, Opt. Lett. **29**, 238 (2004).
26. G. Milione, S. Evans, D. A. Nolan, and R. R. Alfano, Phys. Rev. Lett. **108**, 190401 (2012).
27. A. Flores-Pérez, J. Hernández-Hernández, R. Jáuregui, and K. Volke-Sepúlveda, Opt. Lett. **31**, 1732 (2006).
28. D. W. K. Wong and G. Chen, Appl. Opt. **47**, 602 (2008).
29. C. Lopez-Mariscal and K. Helmerson, Opt. Lett. **35**, 1215 (2010).
30. A. Dudley, R. Vasilyeu, V. Belyi, N. Khilo, P. Ropot, and A. Forbes, Opt. Commun. **285**, 5 (2012).
31. L. Marrucci, C. Manzo, and D. Paparo, Phys. Rev. Lett. **96**, 163905 (2006).
32. S. C. McEldowney, D. M. Shemo, R. A. Chipman, and P. K. Smith, Opt. Lett. **33**, 134 (2008).
33. Y. Li, J. Kim, and M. J. Escuti, Appl. Opt. **51**, 8236 (2012).
34. G. P. Crawford, J. N. Eakin, M. D. Radcliffe, A. Callan-Jones, and R. A. Pelcovits, J. Appl. Phys. **98**, 123102 (2005).
35. I. A. Litvin, A. Dudley, F. S. Roux, and A. Forbes, Opt. Express **20**, 10996 (2012).
36. D. Flamm, D. Naidoo, C. Schulze, A. Forbes, and M. Duparré, Opt. Lett. **37**, 2478 (2012).

Efficient sorting of Bessel beams

Angela Dudley,[1,*] Thandeka Mhlanga,[1] Martin Lavery,[2] Andre McDonald,[1] Filippus S. Roux,[1] Miles Padgett,[2] and Andrew Forbes[1]

[1]*CSIR National Laser Centre, PO Box 395, Pretoria 0001, South Africa*
[2]*Department of Physics & Astronomy, University of Glasgow, Glasgow, UK*
**adudley@csir.co.za*

Abstract: We demonstrate the efficient sorter of Bessel beams separating both the azimuthal and radial components. This is based upon the recently reported transformation of angular to transverse momentum states. We separately identify over forty azimuthal and radial components, with a radial spacing of 1588 m^{-1}, and outline how the device could be used to identify the two spatial dimensions simultaneously.

OCIS codes: (090.1995) Digital holography; (070.6120) Spatial light modulators; (070.3185) Invariant optical fields; (050.4865) Optical vortices.

References and links

1. M. W. Beijersbergen, L. Allen, H. E. L. O. Van der Veen, and J. P. Woerdman, "Astigmatic laser mode converters and the transferof orbital angular momentum," Opt. Commun. **96**(1-3), 123–132 (1993).
2. J. Arlt and K. Dholakia, "Generation of high-order Bessel beams by use of an axicon," Opt. Commun. **177**(1-6), 297–301 (2000).
3. L. Allen, M. W. Beijersbergen, R. J. C. Spreeuw, and J. P. Woerdman, "Orbital angular momentum of light and the transformation of Laguerre-Gaussian laser modes," Phys. Rev. A **45**(11), 8185–8189 (1992).
4. H. He, M. E. J. Friese, N. R. Heckenberg, and H. Rubinsztein-Dunlop, "Direct observation of transfer of angular momentum to absorptive particles from a laser beam with a phase singularity," Phys. Rev. Lett. **75**(5), 826–829 (1995).
5. A. Mair, A. Vaziri, G. Weihs, and A. Zeilinger, "Entanglement of the orbital angular momentum states of photons," Nature **412**(6844), 313–316 (2001).
6. G. Molina-Terriza, J. P. Torres, and L. Torner, "Management of the angular momentum of light: preparation of photons in multidimensional vector states of angular momentum," Phys. Rev. Lett. **88**(1), 013601 (2002).
7. A. Vaziri, G. Weihs, and A. Zeilinger, "Experimental two-photon, three-dimensional entanglement for quantum communication," Phys. Rev. Lett. **89**(24), 240401 (2002).
8. J. T. Barreiro, T. C. Wei, and P. G. Kwiat, "Beating the channel capacity limit for linear photonic superdense coding," Nat. Phys. **4**(4), 282–286 (2008).
9. J. Leach, B. Jack, J. Romero, A. K. Jha, A. M. Yao, S. Franke-Arnold, D. G. Ireland, R. W. Boyd, S. M. Barnett, and M. J. Padgett, "Quantum correlations in optical angle-orbital angular momentum variables," Science **329**(5992), 662–665 (2010).
10. Z. Bouchal and R. Celechovský, "Mixed vortex states of light as information carriers," New J. Phys. **6**, 131 (2004).
11. R. Celechovský and Z. Bouchal, "Optical implementation of the vortex information channel," New J. Phys. **9**(9), 328 (2007).
12. J. Durnin, J. J. Miceli, Jr., and J. H. Eberly, "Diffraction-free beams," Phys. Rev. Lett. **58**(15), 1499–1501 (1987).
13. J. Turunen, A. Vasara, and A. T. Friberg, "Holographic generation of diffraction-free beams," Appl. Opt. **27**(19), 3959–3962 (1988).
14. A. Vasara, J. Turunen, and A. T. Friberg, "Realization of general nondiffracting beams with computer-generated holograms," J. Opt. Soc. Am. A **6**(11), 1748–1754 (1989).
15. G. Indebetouw, "Nondiffracting optical fields: some remarks on their analysis and synthesis," J. Opt. Soc. Am. A **6**(1), 150–152 (1989).
16. R. P. MacDonald, S. A. Boothroyd, T. Okamoto, J. Chrostowski, and B. A. Syrett, "Interboard optical data distribution by Bessel beam shadowing," Opt. Commun. **122**(4-6), 169–177 (1996).
17. Z. Bouchal, J. Wagner, and M. Chlup, "Self-reconstruction of a distorted nondiffracting beam," Opt. Commun. **151**(4-6), 207–211 (1998).
18. I. Litvin, M. McLaren, and A. Forbes, "A conical wave approach to calculating Bessel-Gauss beam reconstruction after complex obstacles," Opt. Commun. **282**(6), 1078–1082 (2009).
19. M. McLaren, M. Agnew, J. Leach, F. S. Roux, M. J. Padgett, R. W. Boyd, and A. Forbes, "Entangled Bessel-Gaussian beams," Opt. Express **20**(21), 23589–23597 (2012).

#179893 - $15.00 USD Received 13 Nov 2012; revised 13 Dec 2012; accepted 14 Dec 2012; published 2 Jan 2013

20. G. Gibson, J. Courtial, M. J. Padgett, M. Vasnetsov, V. Pas'ko, S. M. Barnett, and S. Franke-Arnold, "Free-space information transfer using light beams carrying orbital angular momentum," Opt. Express **12**(22), 5448–5456 (2004).
21. S. N. Khonina, V. V. Kotlyar, R. V. Skidanov, V. A. Soifer, P. Laakkonen, and J. Turunen, "Gauss–Laguerre modes with different indices in prescribed diffraction orders of a diffractive phase element," Opt. Commun. **175**(4-6), 301–308 (2000).
22. J. Leach, M. J. Padgett, S. M. Barnett, S. Franke-Arnold, and J. Courtial, "Measuring the orbital angular momentum of a single photon," Phys. Rev. Lett. **88**(25), 257901 (2002).
23. M. Lavery, A. Dudley, A. Forbes, J. Courtial, and M. Padgett, "Robust interferometer for the routing of light beams carrying orbital angular momentum," New J. Phys. **13**(9), 093014 (2011).
24. A. F. Abouraddy, T. M. Yarnall, and B. E. A. Saleh, "Angular and radial mode analyzer for optical beams," Opt. Lett. **36**(23), 4683–4685 (2011).
25. I. A. Litvin, A. Dudley, F. S. Roux, and A. Forbes, "Azimuthal decomposition with digital holograms," Opt. Express **20**(10), 10996–11004 (2012).
26. G. C. G. Berkhout, M. P. J. Lavery, J. Courtial, M. W. Beijersbergen, and M. J. Padgett, "Efficient sorting of orbital angular momentum states of light," Phys. Rev. Lett. **105**(15), 153601 (2010).
27. M. P. J. Lavery, G. C. G. Berkhout, J. Courtial, and M. J. Padgett, "Measurement of the light orbital angular momentum spectrum using an optical geometric transformation," J. Opt. **13**(6), 064006 (2011).
28. G. C. G. Berkhout, M. P. J. Lavery, M. J. Padgett, and M. W. Beijersbergen, "Measuring orbital angular momentum superpositions of light by mode transformation," Opt. Lett. **36**(10), 1863–1865 (2011).
29. M. P. J. Lavery, D. J. Robertson, G. C. G. Berkhout, G. D. Love, M. J. Padgett, and J. Courtial, "Refractive elements for the measurement of the orbital angular momentum of a single photon," Opt. Express **20**(3), 2110–2115 (2012).
30. C. López-Mariscal, K. Helmerson; "Shaped nondiffracting beams," Opt. Lett. **35**(8), 1215–1217 (2010).
31. R. Rop, A. Dudley, C. Lopez-Mariscal, and A. Forbes, "Measuring the rotation rates of superpositions of higher-order Bessel beams," J. Mod. Opt. **59**(3), 259–267 (2012).
32. M. P. J. Lavery, D. J. Robertson, A. Sponselli, J. Courtial, N. K. Steinhoff, G. A. Tyler, A. Wilner, and M. J. Padgett, "Efficient measurement of orbital angular momentum over 50 states," New J. Phys. in press.

1. Introduction

Numerous studies have been dedicated to optical fields that carry orbital angular momentum (OAM), where each field has an azimuthal angular dependence of $\exp(il\theta)$ [1–4] where l is the azimuthal index and θ is the azimuthal angle. The fact that these fields offer an unbounded state space has made them advantageous for increasing the amount of information that can be encoded onto a single-photon [5–11]. In particular, higher-order Bessel beams are interesting as OAM-carriers as these fields propagate while maintaining their cross-sectional form over a finite distance [12–15] and reconstruct after encountering an obstacle [16–18]. Recently, entanglement in the Bessel basis has been measured, showing an increased spiral bandwidth [19]. Exploiting these properties of Bessel beams may make them useful in the field of long-range, broad-bandwidth communication systems. However, in order for these fields to be a success in the area of optical communication, efficient techniques for extracting the information they carry need to be demonstrated.

A diffraction grating containing a fork discontinuity can be used to couple light of a particular OAM state into a single-mode fibre [5], but this measurement approach requires that one must test for the chosen range of states sequentially. Attempts to develop more complicated holograms that test multiple states have been made [20, 21], however their efficiency is inversely proportional to the number of states being sampled. An alternative setup that does not alter the OAM state during the measurement procedure is a Mach-Zehnder interferometer with a Dove prism in each arm [22, 23], but to measure 2^n states requires 2^n–1 interferometers. A modified Mach-Zehnder interferometer can also be described to determine both the angular and radial mode content of scalar optical fields [24] but such systems are known to be sensitive to alignment [24]. Digital holograms are also used to extract the azimuthal modal content of optical fields for the reconstruction of its amplitude, phase and OAM density [25]. Recently it has been demonstrated that two spatial light modulators in conjunction with a lens can be used to convert the OAM state of light to a specified lateral position [26–28] so that the azimuthal information may be extracted, while leaving the radial component undefined. The approach has been made more efficient by replacing the spatial light modulators with freeform refractive optical components [29].

#179893 - $15.00 USD Received 13 Nov 2012; revised 13 Dec 2012; accepted 14 Dec 2012; published 2 Jan 2013

In this paper we extend the aforementioned concept to extract the information in both the azimuthal and radial components of Bessel beams. We show that we can identify forty-one OAM states and forty-one radial components of our higher-order Bessel beams, and show the applicability of the approach to measure super-positions of Bessel beams.

2. Concept and experimental setup

In this work we make use of Bessel beams as our OAM-carrying bases functions, which are characterized by an azimuthal mode index, l, and a radial component, k_r, as

$$u(r,\theta,z=0) = J_l(k_r r)\exp(il\theta). \tag{1}$$

Here k_r is the transverse wave number and is defined as $k_r = k\sin\alpha$, where $k = 2\pi/\lambda$ and α is the opening angle of the cone on which the waves propagate. The Fourier transform of the Bessel field is described by an annular ring of radius R,

$$\Im[u(r,\theta)] = \begin{cases} \exp(il\theta) & R \approx r \\ 0 & elsewhere \end{cases}. \tag{2}$$

The radial wavevector is related to the radius of the annular ring as $k_r = kR/f$, where f is the focal length of the Fourier transforming lens. It is these OAM-carrying fields, of differing radial components, whose OAM (l) and radial information (k_r) we wish to measure experimentally.

The technique that is employed for the measurement of the OAM spectrum and the radial components of the Bessel beams consists of two freeform optical elements [29] that map a position in an input plane (x,y) to a position in the output plane (v,u) by a conformal mapping [27–29]

$$v = \frac{d}{2\pi}\arctan\left(\frac{y}{x}\right), \tag{3}$$

$$u = -\frac{d}{2\pi}\ln\left(\frac{\sqrt{x^2+y^2}}{b}\right) = -\frac{d}{2\pi}\ln\left(\frac{k_r f}{kb}\right), \tag{4}$$

where the parameter b controls the scaling of the radial component and d is the aperture size of both freeform optics. An initial radial spacing of Δk_r will result in a vertical spread in the signal plane, Δu, given by

$$\Delta u = \frac{d}{2\pi}\frac{\Delta k_r}{k_r}, \tag{5}$$

and thus the minimum resolvable feature, δ, constrains the resolvable wavevectors to

$$\Delta k_r \geq \frac{2\pi}{d} k_r \delta. \tag{6}$$

This implies that while $\Delta k_r \geq \Delta$ [from Eq. (5)] where Δ is the width of the resulting annular ring, the system is further constrained by δ which is the smallest resolvable feature in the detector plane [from Eq. (6)]. The range of wavevectors that can be detected is also limited by the aperture size of the second freeform optic, $k_r \geq \exp(-\pi)kb/f$.

In this first step an annular ring of light (Fourier transform of the Bessel beam) is mapped to a horizontal line of fixed width, thus any azimuthal phase variation in the ring transforms into a linear phase variation along the line - a tilt of the phase front. If this inclined phase front is passed through a Fourier transforming lens of focal length f, then a focused spot is produced at an l-dependent horizontal position given by

#179893 - $15.00 USD Received 13 Nov 2012; revised 13 Dec 2012; accepted 14 Dec 2012; published 2 Jan 2013

$$\Delta_H = \frac{\lambda f l}{d}. \tag{7}$$

We note that imaging of the output will return the radial information of the field, which is stored in the vertical off-set of the horizontal line of light:

$$\Delta_V = \frac{d}{2\pi} \ln\left(\frac{k_\mu f}{kb}\right). \tag{8}$$

Thus an optical set-up which images in the vertical axis and Fourier transforms in the horizontal axis will allow the simultaneous measurement of Δ_H and Δ_V and thus the azimuthal and radial information of the field. Such an optical system may be implemented with three cylindrical lenses; a schematic of the concept is given in Fig. 1 with the experimental set-up shown in Fig. 2. A HeNe laser was expanded through a telescope (lenses L1 and L2) to illuminate the liquid crystal display of a spatial light modulator (SLM) where the Bessel beams were encoded in the far-field [Fig. 2(b)] using complex amplitude modulation [30, 31].

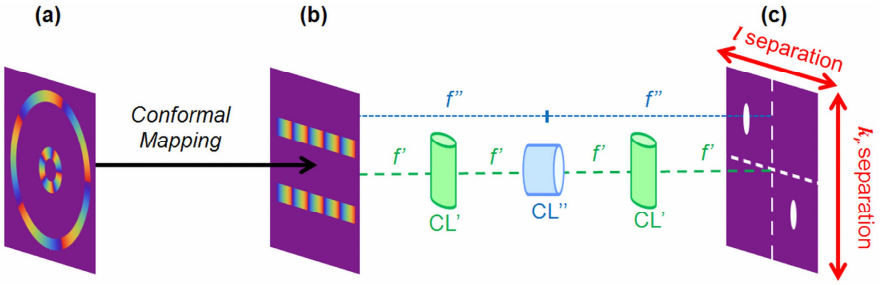

Fig. 1. (a): The annular rings of two Bessel beams are mapped to transverse momentum modes in (b). Cylindrical lenses (CL) arranged in a 4-*f* configuration map the transverse momentum modes to unique *x*- and *y*-coordinates in column (c).

The resulting annular rings were propagated through the mode sorter (denoted by optical elements, R1 and R2), where R1 performed a log-polar mapping thus transforming the azimuthal modes to transverse momentum states, while also mapping the radial component.

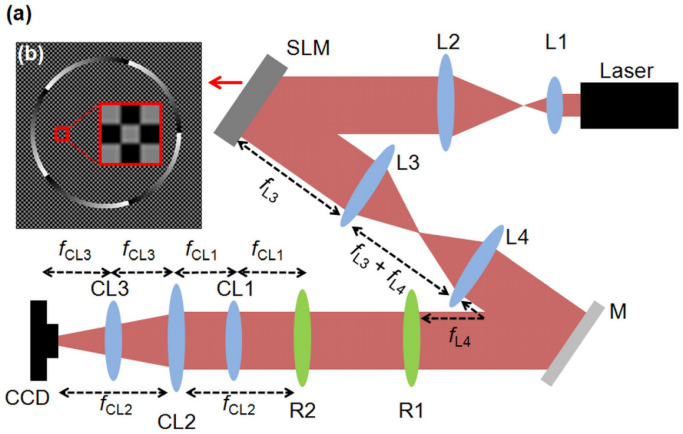

Fig. 2. (a) Schematic of the experimental setup for identifying the azimuthal and radial components of Bessel beams. L, lens (f_{L1} = 15 mm, f_{L2} = 125 mm, f_{L3} = 500 mm, f_{L4} = 500 mm); SLM, spatial light modulator; M, mirror; R, aspheric optical element; CL, cylindrical lens (f_{CL1} = 50 mm,(orientated to focus the *y*-axis), f_{CL2} = 100 mm (orientated to focus the *x*-axis), f_{CL3} = 50 mm (orientated to focus the *y*-axis)); CCD, CCD camera. (b) The phase profile of the annular ring with a zoomed-in insert of the alternating phase values.

#179893 - $15.00 USD Received 13 Nov 2012; revised 13 Dec 2012; accepted 14 Dec 2012; published 2 Jan 2013

The freeform optics were fabricated from PMMA (Poly methyl methacrylate) to an aperture size of d = 16 mm and a focal length of f = 300 mm, with a scaling parameter b = 0.00477. As an illustration, the conformal mapping of the ring into a line is shown as a video clip (Media 1), which contains experimental images of an annular ring ($k_r = 2.62 \times 10^4$ m^{-1}, l = + 1) propagating between the two freeform optical elements.

3. Experimental results and discussion

Bessel beams with $k_r = 2.62 \times 10^4$ m^{-1}, having azimuthal orders ranging from l = –20 to + 20 were generated and directed through the mode sorter. An example of one of the Bessel beams possessing an azimuthal order of l = –5 is given in Fig. 3(a). The unraveled transverse momentum mode at the plane of R2 was focused by a spherical lens having a focal length of f = 250 mm, producing an elongated lateral spot shown in Fig. 3(b). The position of the spots produced by incoming azimuthal modes ranging for l = –20 to + 20 were measured and are given in Fig. 4(a). There is very good agreement between the experimentally measured positions (red circles) and the theoretical expected positions (black curve), calculated from Eq. (7).

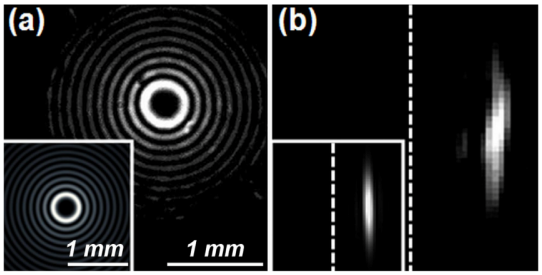

Fig. 3. (a) The Bessel beam and (b) lateral spot for $k_r = 2.62 \times 10^4$ m^{-1} and l = –5. Theoretical results are given as inserts.

The measurement selectivity corresponds to cross-talk between neighboring modes, given by the off-diagonal elements in Fig. 4(b). Our results illustrate that OAM states of higher-order Bessel modes can be measured with a similar selectivity as that obtained for LG modes [26].

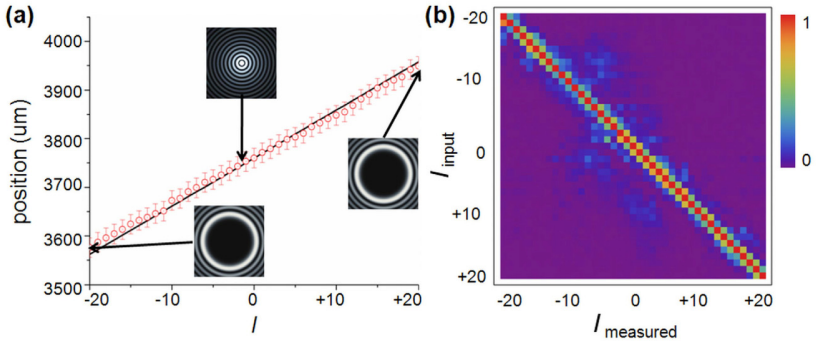

Fig. 4. (a) The position of the spot produced at the plane of the CCD as a function of l. Accompanying theoretical Bessel beams are given as inserts. (b) Relative fractions of the intensity at each detector position for l = –20 to + 20 ($k_r = 2.62 \times 10^4$ m^{-1}). The strong diagonal and weak off-diagonal terms imply a highly accurate and precise mode sorter.

The radial component of the Bessel beam was varied from values of $k_r = 0.23 \times 10^4$ m^{-1} to 6.43×10^4 m^{-1} ($\Delta k_r = 0.16 \times 10^4$ m^{-1}) and an example of one of the Bessel beams is given in Fig. 5(a). In order to simultaneously resolve a range of radial components, the larger of the

#179893 - $15.00 USD Received 13 Nov 2012; revised 13 Dec 2012; accepted 14 Dec 2012; published 2 Jan 2013

two limits [resulting from Eqs. (5) and (6)] needs to be satisfied. For the parameters used in this paper, the radial spacing for two extreme cases (k_r^{max} and k_r^{min}) is constrained by the width of the annular ring ($\Delta k_r \geq 0.32 \times 10^4$ m^{-1}), as well as the smallest resolvable feature in the detector plane ($\delta = 44$ μm): $\Delta k_r \geq 0.11 \times 10^4$ m^{-1}(for $k_r^{max} = 6.43 \times 10^4$ m^{-1}) and $\Delta k_r \geq 0.004 \times 10^4$ m^{-1}(for $k_r^{min} = 0.23 \times 10^4$ m^{-1}). The transformed annular ring was imaged onto the CCD, with the use of two spherical lenses and is depicted in Fig. 5(b). The position of the transformed line shifts vertically as the radius of the annular ring changes and is illustrated in Fig. 6(a), where the measured position of the transformed annular ring is plotted as a function of k_r. Again there is good agreement between the experimentally measured positions (red circles) and the theoretical expected positions (black curve), calculated with the use of Eq. (8). The error bars decrease as the radial component increases because the width of the transformed line in the detector plane becomes narrower.

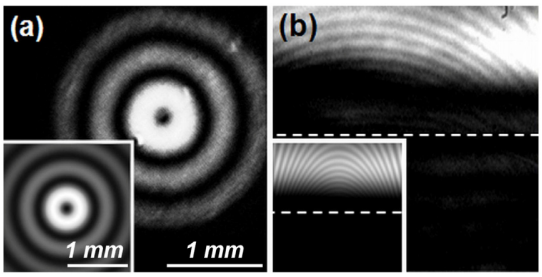

Fig. 5. (a) The Bessel beam and (b) unraveled transverse momentum mode for $l = +1$ and $k_r = 0.72 \times 10^4$ m^{-1}. Theoretical results are given as inserts.

Similarly in detecting the radial components, apertures in the detector plane were centered on the expected line positions and relative fractions of the radial spectrum for various input modes were determined and are presented in Fig. 6(b). Likewise, there is a slight overlap of the transformed lines between neighboring radial coordinates. It is evident from Fig. 6(b) that if this spacing is doubled, the cross-talk between neighboring radial modes will be drastically diminished. Nevertheless, the results of Fig. 4(b) and Fig. 6(b) clearly show that one can extract information stored in both dimensions.

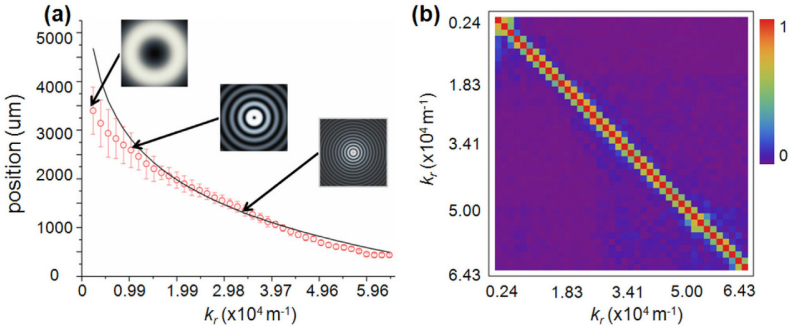

Fig. 6. (a) The position of the transformed line produced at the plane of the CCD as a function of R. Accompanying theoretical Bessel beams are given as inserts. (b) Relative fractions of the intensity at each detector position for $k_r = 0.23 \times 10^4$ m^{-1} to 6.43×10^4 m^{-1} ($l = +1$).

Multiple Bessel beams were also directed through the mode sorter and an example of the superposition Bessel beams is presented in Fig. 7(a). The separation of the two azimuthal and two radial components, when using cylindrical lenses CL1, CL2 and CL3, is depicted in Fig. 7(b) accompanied with the theoretical prediction, illustrating that the mode sorter is capable of distinguishing super-imposed azimuthal and radial modes. Although there is good

#179893 - $15.00 USD Received 13 Nov 2012; revised 13 Dec 2012; accepted 14 Dec 2012; published 2 Jan 2013

agreement between the experimental and theoretical locations of the lateral spots, the shape of the measured lateral spots shows some distortion which could be due to the alignment sensitivity of the cylindrical lenses.

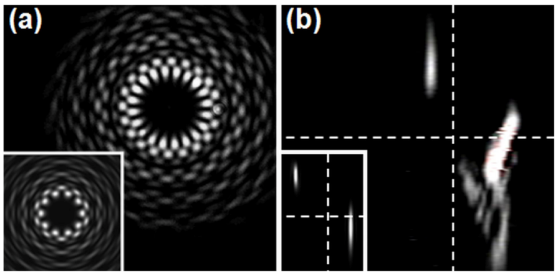

Fig. 7. (a) Super-imposed Bessel beams and (b) the lateral spots produced at the plane of the CCD. Theoretical results are given as inserts.

The number of azimuthal and radial modes that can be identified can be increased by increasing the aperture size of the freeform optical elements. We tested two different aperture sizes (d = 8 mm and 16 mm) and noted that by doubling the aperture diameter, the azimuthal bandwidth that can be identified increased by a factor of 2. Our results could further be improved by first separating the OAM modes into odd and even ports [22, 23] to decrease cross-talk in the measured spectrum.

4. Conclusion

We have illustrated the separation of higher-order Bessel beams in both their azimuthal and radial indices. This technique is not only limited to Bessel beams, but it can also be implemented with other optical fields [32]. The ability to extract encoded information across two higher-dimensional state spaces will prove useful in quantum communication and information systems.

#179893 - $15.00 USD Received 13 Nov 2012; revised 13 Dec 2012; accepted 14 Dec 2012; published 2 Jan 2013

Digital bi-photon spiral imaging

Thandeka Mhlanga[a, b], Melanie McLaren [a], Alpha Ibrahim [a], Thomas Konrad[b] and Andrew Forbes[a, b]

[a]CSIR National Laser Centre, P.O. Box 395, Pretoria 0001, South Africa
[b]School of Physics, University of KwaZulu-Natal, Private Bag X54001, Durban 4000, South Africa.

ABSTRACT

Quantum ghost imaging using entangled photon pairs has become an interesting field of investigation as it illustrates the quantum correlation between the photon pairs. We introduce a new technique using spatial light modulators encoded with appropriate digital holograms to recover not only the amplitude, but also the phase of the digital object. Down-converted photon pairs are entangled in the orbital angular momentum basis, which are typically measured using a spiral phase hologram. Thus by encoding a spiral annular slit hologram into the idler arm, and varying it radially we can simultaneously recover the phase and amplitude of the field in question. We show that there is a good correlation between the encoded field function and the reconstructed images.

Keywords: ghost imaging, spiral ring-slit, orbital angular momentum

1. INTRODUCTION

The technique used to illustrate quantum correlations between entangled photon pairs is referred to as ghost imaging, which was first observed more than 10 years ago by Pittman *et al.*[1] This technique produces an amplitude image of the object by combining information from two photon detectors; a single pixel (bucket) scanning detector with no spatial resolution, that collects photons that have interacted with the object and a multi-pixel detector collecting photons that had not interact with the object[1,2] as seen in Fig. 1. There are

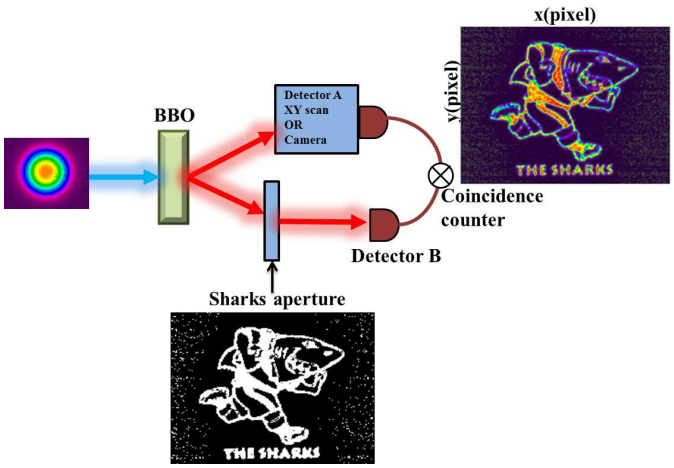

Figure 1. The ghost imaging setup using the sharks aperture in the signal arm, and a scanning detector in the idler arm resulting in coincidence counts that give the sharks image.

uncertainties of whether ghost imaging is solely a quantum phenomenon,[3,4] but this is not our interest of study. Orbital angular momentum (OAM) entanglement has shown to be promising in achieving high dimensional entangled states that can be useful in quantum key distribution[5] and quantum communication.[6] Also it has been shown that the OAM quantum correlations can be used for edge enhancement of the object image within

Further author information: (Send correspondence to A. Forbes.)
A. Forbes: E-mail: aforbes1@csir.co.za

Laser Beam Shaping XV, edited by Andrew Forbes, Todd E. Lizotte, Proc. of SPIE Vol. 9194, 91940A © 2014 SPIE · CCC code: 0277-786X/14/$18 · doi: 10.1117/12.2066371

a ghost imaging setup,[7] where spatial light modulators (SLMs) were encoded with phase modulating holograms along the edge of the object; one as a phase object and the other as a phase filter in the signal and idler arms respectively. Not only can we modulate the phase of light using an SLM, but also the checker board pattern which is simply an array of alternating set of pixels out of phase by π can be used to modulate the amplitude of light. Taking this into consideration, we took the method of Jack *et. al*[7] further by encoding the signal arm with a phase object and the idler arm with a phase and amplitude filter to recover the phase and amplitude of the object by correlating the detected signals on the coincidence counter.

2. CONCEPT

The task was to find a tool that can be used not only to give the amplitude of the object in arm A, but also to recover the phase of the object by correlating the detected signals from both arms. We know that for an arbitrary field $u(r,\theta)$ that forms a complete basis (orthogonal, complete) set, such as the angular harmonics $\exp(i\ell\theta)$, we can describe its full field distribution[8] as:

$$u(r,\theta) = \sum a_\ell(r)\exp(i\ell\theta), \tag{1}$$

where $a_\ell(r)$ is the r dependent coefficient, ℓ is the azimuthal index. Equation (1) can be implemented by an azimuthally varying ring of a particular thickness $\triangle$ as in Fig. 2 (b). Just as a Gaussian beam can be modulated into a vortex mode with the correct hologram, this process works in reverse such that a vortex mode can be converted into a Gaussian beam. The ring selects the OAM state of light acting as a phase filter and while the checker board as an amplitude filter.

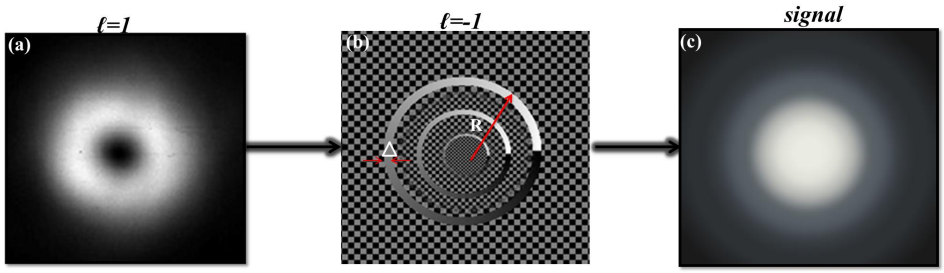

Figure 2. (a) LG of ℓ=1 passing through (b) a varying spiral ring-slit of azimuthal index ℓ=-1 giving a (c) signal on the detector recovering the phase of the field. Since the ring varies radially (R) it also gives the amplitude of the field.

3. EXPERIMENTAL REALISATION

The experimental setup consists of two highlighted sections as shown in Fig. 3. The first highlighted section shows a mode locked ultraviolet (355 nm wavelength) laser of average power of 350 mW which was used to pump a type I BBO crystal that produces collinear entangled photon pairs through the process of spontaneous parametric down-conversion (SPDC). To reflect the pump beam and transmit the down-converted light, a band pass filter was placed after the crystal. The front plane of the crystal was imaged and magnified by L1 (f=200 mm) and L2 (f=400 mm) onto the second highlighted section of two separate spatial light modulators (SLMs). SLM A was encoded with the object hologram and SLM B was encoded with the spiral ring-slit of thickness $\triangle$=0.08 mm scanning through the photons in the radial and azimuthal directions. Each SLM plane was then imaged by a $\times$250 demagnification telescope using L3 (f=500 mm) and L4 (f=2 mm), to be coupled into single mode fibres (SMFs), which only support the fundamental Gaussian mode, of mode field diameter of 4.6 μm. Each SLF was attached to an avalanche photo-diode (APD), connected to coincidence counter.

3.1 Back-projection results

This setup in Fig. 3 was first set in back-projection mode for alignment purposes, where the BBO crystal was replaced by a mirror, and a 710 nm diode laser was connected to the SMF in arm A allowing light to propagate through the system in reverse. The images of the generated object from SLM A, were recorded by placing a

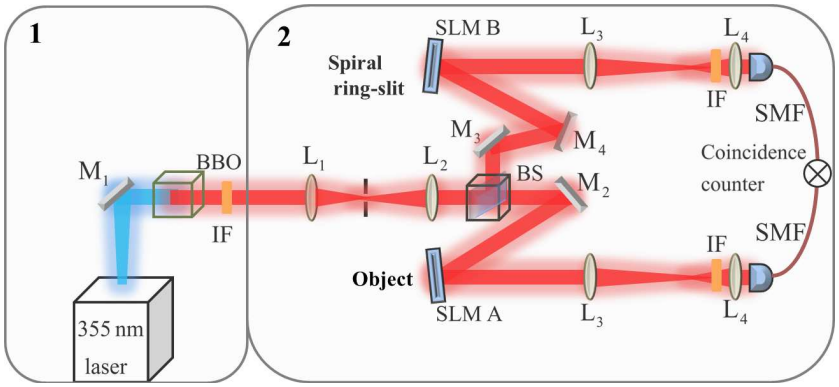

Figure 3. The schematic diagram of the experimental setup highlighted into two sections, 1. to generate entangled photon pairs, 2. to perform the spiral imaging technique recovering the phase and amplitude of the object.

mirror before SLM B and a CCD camera at the plane of SLM B. In this back-projection mode, SLM A was addressed with an azimuthal index of ℓ=+1 fork hologram generating a Laguarre-Gauss (LG) mode shown as an insert in Fig. 4(a) with its corresponding cross-sectional intensity profile. On SLM B we encoded a spiral ring-slit of ℓ=-1 and varied it radially and recorded the single count rates at detector B as a function of the radial position. Fig. 4(b) shows this recorded count rate and it is clear that we recover the profile of an LG mode. We then performed a similar experiment, but this time changed the object hologram on SLM A, by encoding a hologram with four different azimuthal indices each at different radii. The resulting radial counts profiles of Fig. 5 (a) ℓ=0 mode, was encoded with an inner radius of 0 mm and an outer radius of 0.08 mm, while Fig. 5 (b) ℓ=5, was encoded with an inner radius of 0.08 mm and outer radius of 0.16 mm. Similarly Fig. 5 (c) ℓ=3 mode existed between r_{in}=0.16 mm to r_{out}=0.24 mm, and Fig. 5 (d) ℓ=1 existed between r_{in}=0.24 mm to r_{out}=0.32 mm. These profiles were obtained by varying the azimuthal and radial components of the spiral ring-slit on SLM B.

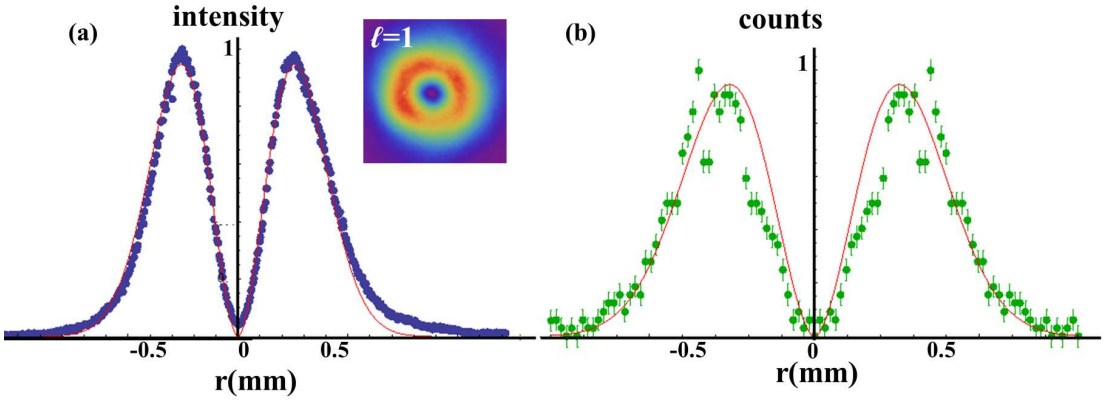

Figure 4. LG of ℓ=1 (a) intensity profile generated from SLM A, obtained from the cross-section of CCD image in insert, with (b) the corresponding back-projected coincidence counts profile.

3.2 Down-converted results

The setup in Fig. 3. was set to down converted mode generating entangled photon pairs that were projected into first the LG basis[9] and then the Bessel-Gauss (BG) basis,[10,11] which has shown to provide a wider OAM entanglement spectrum and the ability to reconstruct entanglement after encountering an obstruction.[12] This was achieved by encoding SLM A with appropriate holograms, the fork hologram and binary axicon respectively. The measured coincidence counts successfully recovered the phase and amplitude of these angular harmonics as illustrated in Fig. 6. Since these modes form a complete basis set we can generate their superposition by simply summing their transmission functions together, this can be implemented through digital holography.[13,14] We

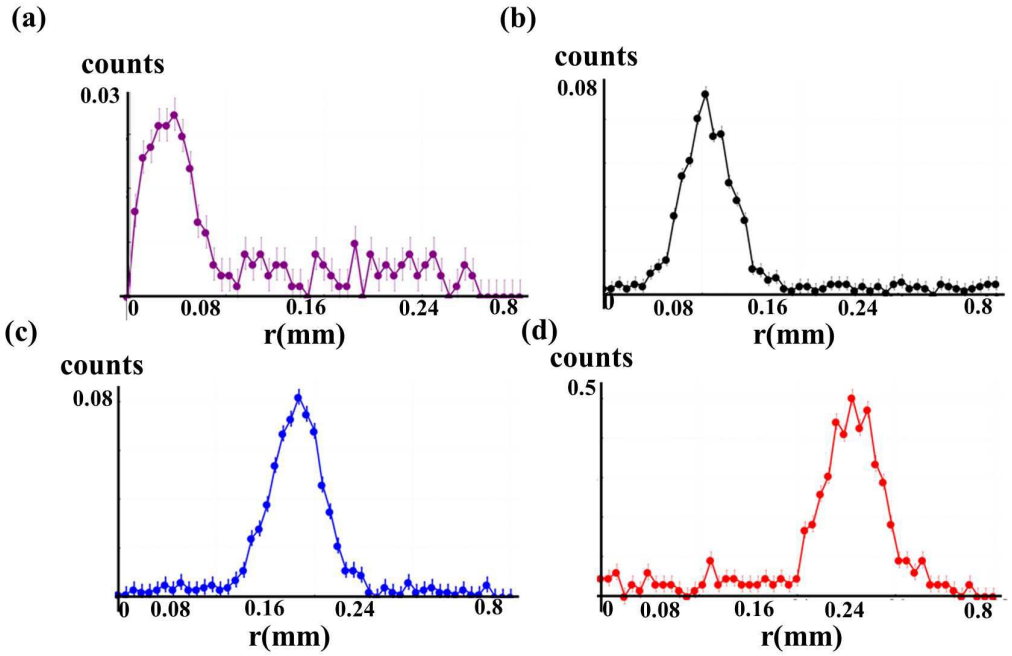

Figure 5. Radial profile counts of (a) ℓ=0, (b) ℓ=5, (c) ℓ=3, and (d) ℓ=1.

generated a superposition of LG modes Fig. 7 (a) on SLM A, and by varying the spiral ring-slit, we detected the down-converted counts as a function of the radial position, thereby simultaneously recovering the phase and amplitude of these fields Fig. 7 (b,c). The mode which was not encoded was not detected as shown in Fig. 7 (d), even though it is the neighbouring mode of the encoded ones, which shows the efficiency of our imaging tool.

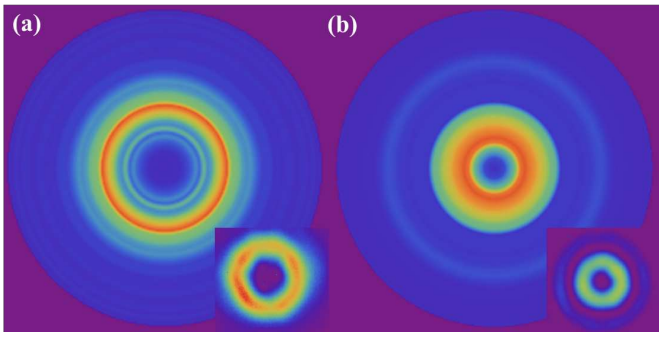

Figure 6. Reconstructed fields (a) LG of ℓ=2, (b) BG of ℓ=2 from down-converted counts with their CCD images on the inserts.

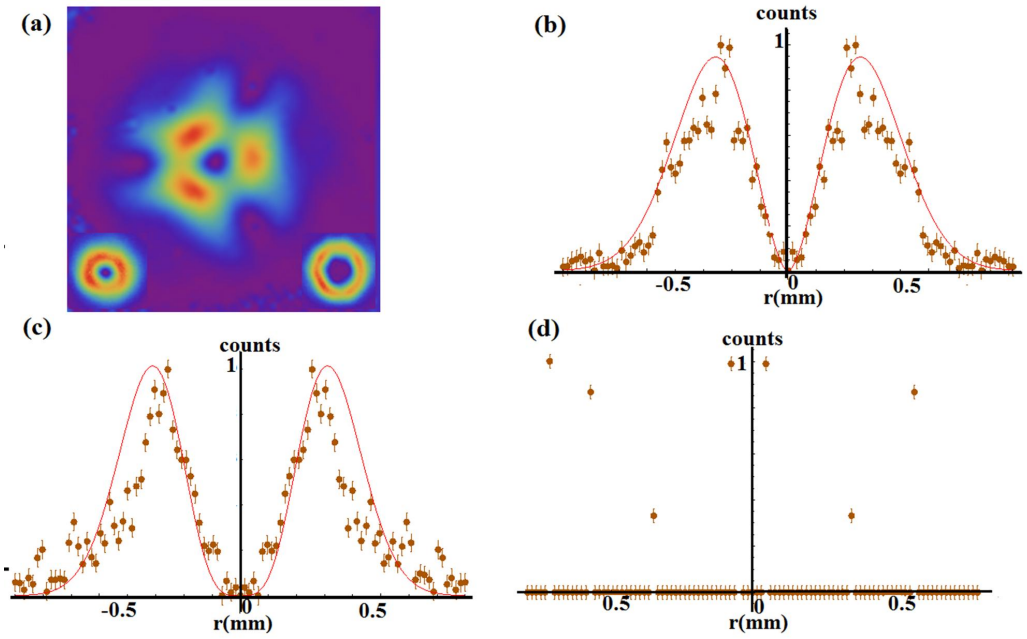

Figure 7. (a)CCD petal image of the superposition of LG of ℓ=-1 and ℓ =2 shown on the inserts. Reconstructed radial profiles of (b) LG of ℓ=-1, (b) ℓ =2 from down-converted counts. (e) LG of ℓ =3, which was not encoded on the superposition, hence there are no counts to recover its profile.

4. CONCLUSION

We have successfully shown that we can simultaneously recover the phase and amplitude of any arbitrary field that forms a complete basis set, in a ghost imaging setup using a digital spiral ring-slit. This is a unique technique as it differs from the traditional ghost imaging that requires a scanning detector to only recover the amplitude of the field.

REFERENCES

1. Pittman, T., Shih, Y., Strekalov, D., and Sergienko, A., "Optical imaging by means of two-photon quantum entanglement," *Phys. Rev. A* **52**(5), R3429–R3432 (1995).
2. Strekalov, D., Sergienko, A., Klyshko, D., and Shih, Y., "Observation of two-photon ghost interference and diffraction," *Physical Review Letters* **74**(18), 3600 (1995).
3. Bennink, R. S., Bentley, S. J., and Boyd, R. W., "two-photon coincidence imaging with a classical source," *Physical Review Letters* **89**(11), 113601 (2002).
4. Gatti, A., Brambilla, E., Bache, M., and Lugiato, L. A., "Ghost imaging with thermal light: comparing entanglement and classicalcorrelation," *Physical Review Letters* **93**(9), 093602 (2004).
5. Mafu, M., Dudley, A., Goyal, S., Giovannini, D., McLaren, M., Padgett, M., Konrad, T., Petruccione, F., Lütkenhaus, H., and Forbes, A., "Higher-dimensional orbital angular momentum based quantum key distribution with mutually unbiased bases," *Phys. Rev. A* **46**(3), 15–28 (2013).
6. Vaziri, A., Pan, J., Jennewein, T., Weihs, G., and Zeilinger, A., "Concentration of higher-dimensional entanglement: Qutrits of photon orbital angular momentum," *Phys. Rev. Lett.* **91**(22), 227902 (2003).
7. Jack, B., Leach, J., Romero, J., Franke-Arnold, S., Ritsch-Marte, M., Barnett, S., and Padgett, M., "Holographic ghost imaging and the violation of a bell inequality," *Physical Review Letters* **103**(8) (2009).
8. Litvin, I. A., Dudley, A., Roux, F. S., and Forbes, A., "Azimuthal decomposition with digital holograms," *Optics Express* **20**(10), 10996–11004 (2012).
9. Mair, A., Vaziri, A., Weihs, G., and Zeilinger, A., "Entanglement of the orbital angular momentum states of photons," *Nature* **412**(6844), 313–316 (2001).

10. McLaren, M., Agnew, M., Leach, J., Roux, F., Padgett, M., Boyd, R., and Forbes, A., "Entangled bessel-gaussian beams," *Opt. Express* **20**(21), 23589–23597 (2012).
11. McLaren, M., Romero, J., Padgett, M., Roux, F., and Forbes, A., "Two-photon optics of bessel-gaussian modes," *Phys. Rev. A* **88**(3), 033818 (2013).
12. McLaren, M., Mhlanga, T., Padgett, M. J., Roux, F. S., and Forbes, A., "Self-healing of quantum entanglement after an obstruction," *Nature Communications* **5**(3248) (2014).
13. Vasilyeu, R., Dudley, A., Khilo, N., and Forbes, A., "Generating superpositions of higher–order bessel beams," *Optics Express* **17**(26), 23389–23395 (2009).
14. Gibson, G., Courtial, J., Padgett, M., Vasnetsov, M., Pas' ko, V., Barnett, S., and Franke-Arnold, S., "Free-space information transfer using light beams carrying orbital angular momentum," *Optics Express* **12**(22), 5448–5456 (2004).

Digital holograms for laser mode multiplexing

Thandeka Mhlanga[a, b], Abderrahmen Trichili[c], Angela Dudley[a], Darryl Naidoo[a, b], Mourad Zghal[c] and Andrew Forbes[a, b]

[a]CSIR National Laser Centre, P.O. Box 395, Pretoria 0001, South Africa
[b]School of Physics, University of KwaZulu-Natal, Private Bag X54001, Durban 4000, South Africa
[c]University of Carthage, Engineering School of Communication of Tunis (Sup'Com), GreS'Com Laboratory, Ghazala Technopark, 2083, Ariana, Tunisia.

ABSTRACT

High-capacity data transmission has been implemented using single channel optical systems. This technique is limited and soon it will be unable to fulfill the growing needs for higher bit rate data transmission. Hence multi-mode transmission has been recently given attention as a potential solution to the current problems. In this context, we demonstrate a method of multiplexing laser modes using spatial light modulators (SLMs). In our proposed technique, we use Laguerre Gaussian (LG) modes, which form a complete basis set; hence multi-mode masks can be created by taking a linear combination of the LG modes. Since LG modes are characterised by two degrees of freedom, the azimuthal index ℓ and radial index ρ, this allows for multi-dimensional states. There are however some experimental challenges which include the sensitivity of the setup to misalignment, that leads to mode-coupling. It is also important that the injected modes ha a uniform power spectrum so that are weighted equally. The size of the multi-modes is highly dependent on the resolution of the SLM.

Keywords: spatial modes, multiplex, mode coupling

1. INTRODUCTION

Optical networks form a foundation of modern communications networks since the replacement of copper wires with optical fibres in the 1980's. This fibre technology has been based on single mode fibres (SMF), and due to the increasing demand in data transmission by a factor of approximately 10 every four years[1] as a result of the digital world we live in, the available capacity of the SMF will be limited in the near future. This limit in capacity is based on the Shannon capacity for non-linear fibre channels,[1] where the SMF cannot carry more than 100 Tbits s^{-1} of data. Optical transmission through SMF has been achieved through other optical properties of light, the dimension that has not yet been explored to transmit data is space. Spatial modes such as the Laguerre-Gauss (LG) modes,[2] have been studied as potential solutions to increase the bandwidth for optical communication through the process of mode division multiplexing (MDM),[3–5] which is based on using the LG modes as independent information carriers through SMFs, as they carry orbital angular momentum (OAM)[6] which is an unbounded degree of freedom. This OAM property of light has shown to be useful in various applications from manipulation of micro-particles[2] to successful classical and quantum free-space communication experiments.[6] There are certain limitations in using these modes for optical communication, such as mode coupling, which we look into, to improve the signal detection. It has been show that aberrated wave fronts result in a distorted modal spectrum.[7] We illustrate that by taking this into account, we can successful multiplex and demultiplexed the LG modes of two degrees of freedom in free-space, with minimized mode coupling.

Further author information: (Send correspondence to A. Forbes)
A. Forbes: E-mail:aforbes1@csir.co.za

Laser Beam Shaping XV, edited by Andrew Forbes, Todd E. Lizotte, Proc. of SPIE Vol. 9194, 91941B © 2014 SPIE · CCC code: 0277-786X/14/$18 · doi: 10.1117/12.2062999

2. THEORY

The Laguerre-Gauss beams[2] form a complete basis set as a solution to the Helmholtz wave equation in cylindrical co-ordinates with a field function given by:

$$\begin{aligned} u_{\ell,\rho}(r,\theta,z) &= \frac{1}{\omega(z)}\sqrt{\frac{2\rho}{\pi(|\ell|+\rho)}}\left(\frac{\sqrt{2}r}{\omega(z)}\right)^{|\ell|}\exp\left(\frac{-r^2}{\omega(z)}\right)L_\rho^{|\ell|}\left[\frac{2r^2}{\omega^2(z)}\right] \\ &\times \exp\left[i\frac{kr^2}{2R(z)}\right]\exp(i\ell\theta)\exp(i\Phi(\rho,\ell,z)). \end{aligned} \tag{1}$$

These LG modes are characterized by two indices ℓ and ρ corresponding to the azimuthal and radial indices respectively. When ℓ=ρ=0, the mode simplifies to a Gaussian mode having a flat wave front. The wave front of these modes spirals around the beam axis creating a phase singularity,known as an optical vortex, where no energy nor momentum exist around that point. The simplest generation of these modes is through digital holography,[2] where the phase of the incoming Gaussian field is diffracted by a ℓ-fork diffraction grating into a LG mode of order ℓ, where ℓ corresponds to the number of fork dislocations which indicates the amount of OAM carried by these modes as shown in Fig. 1.

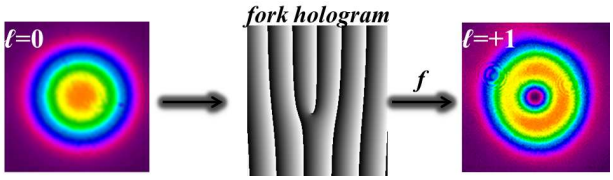

Figure 1. Generation of the LG mode of ℓ=+1 using a fork hologram.

These are not the only spatial modes that carry OAM, Bessel-Gauss (BG) beams also form part of the family of helical modes and they are similar to the LG modes in that they also carry OAM. They do however differ in their ability to reconstruct themselves after encountering an obstacle,[8] and they remain diffraction-free upon propagation for a finite distance.[9] The Bessel-Gaussian (BG) function in polar coordinates, is given by

$$E_\ell^{BG}(r,\Phi,z) = \sqrt{\frac{2}{\pi}}J_\ell\left(\frac{z_R k_r r}{z_R - iz}\right)\exp(i\ell\Phi - ik_z z)\exp\left(\frac{ik_r^2 z w_0^2 - 2kr^2}{4(z_R - iz)}\right), \tag{2}$$

where ℓ is the azimuthal index (a signed integer), $J_\ell(\cdot)$ is the Bessel function of order ℓ; k_r and k_z are the radial and longitudinal wave numbers. The initial radius of the Gaussian profile is w_0 and the Rayleigh range is $z_R = \pi w_0^2/\lambda$. The propagation constant k and the parameters k_r and k_z are related by $k^2 = k_r^2 + k_z^2$. These modes can be generated using a Durnin's ring-slit,[10] which can be implemented digitally[11] by modulating the input beam Fig. 2 (a) with a ring-slit surrounded by a checker board pattern in Fig. 2(b), which is simply an array of alternating sets of pixels that are out of phase by π allowing us to modulate the amplitude and phase of the incident beam to produce the desired mode in Fig. 2 (c).

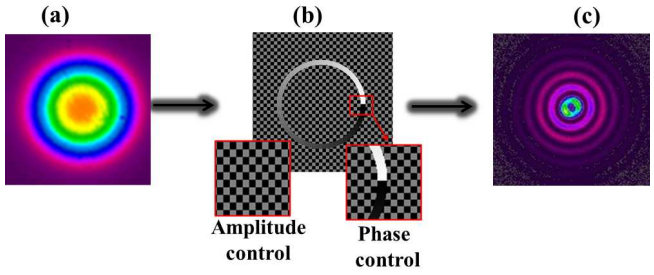

Figure 2. (a) Gaussian beam incident on (b) spiral hologram with inserts of the checker board and the ring-slice of azimuthal variation used to modulate the amplitude and phase of light respectively, generating (c) a BG mode of ℓ=1 at the far-field.

3. EXPERIMENTAL REALISATION

Using the experimental setup in Fig. 3 where a Gaussian beam Fig. 3 (a) was expanded and collimated using lenses L1 (f=35 mm) and L2 (f=750 mm) to approximate a plane wave front in Fig. 3 (b) onto SLM1. At SLM1 LG modes of radial index ρ and azimuthal index ℓ were generated and filtered through the $4f$ imaging system using an aperture and imaged onto SLM2, which we encode with varying azimuthal and radial indices. These indices were detected from the signal obtained at the focal plane of lens L3 (f=250 mm) on the CCD camera. Using the Arrizon *et. al* technique,[12] we generated holograms that modulate the phase and amplitude of the incident Gaussian beam with a flat wave front such that we could generate the superposition of the LG modes in Fig. 4 (a, b, c).

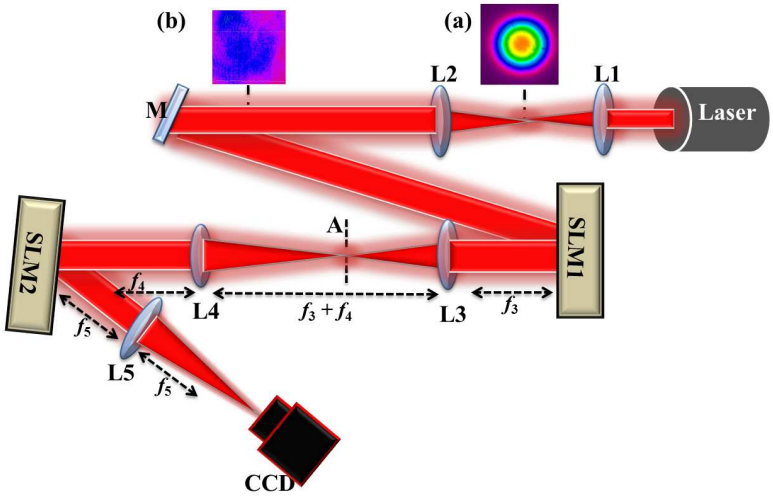

Figure 3. Schematic of the experimental setup where(a) is the Gaussian mode from the laser was expanded by a telescope to approximating a plane wave (b), where L-lens, M-mirror, SLM-spatial light modulator, CCD-camera.

Bessel-Gauss (BG) beams have shown to be useful in manipulation of micro-particles,[8] and in single photon experiments for high-dimensional entangled state,[13] and for reconstruction of quantum entanglement.[14] However the multiplexing of BG modes for optical communication purposes has not been investigated. Holograms encoded with multiple azimuthal phase components at varying radial distances generate superpositions of BG modes and can be implemented in the same experimental setup as in Fig. 3, where SLM1 was encoded with the annular ring holograms with the corresponding petal structures in Fig. 4 (d,e,f).

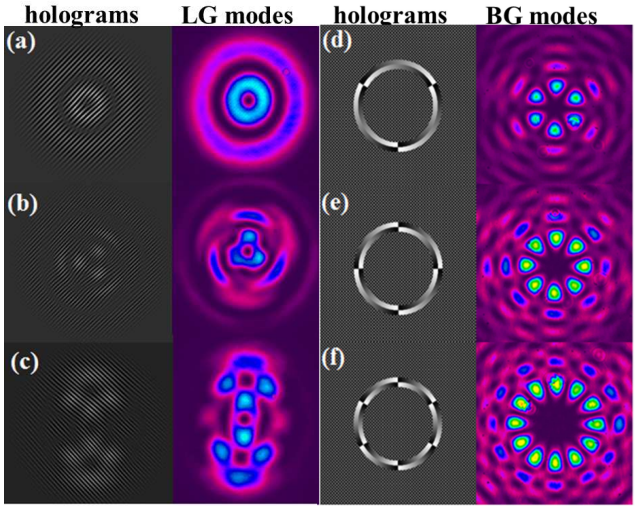

Figure 4. Holograms of ρ, ℓ modes of (a) ρ, ℓ=(1, 1), (b) the superposition of ρ, ℓ=(3, 4) and ρ, ℓ=(1, 1) modes as well as (c) the superposition of ρ, ℓ= (1, 1), (1, 3), (1, 5), (1, 7). BG holograms of (d) the superposition of ℓ=± 3 resulting into 6 petal structures, (e) ℓ= ± 4 resulting into 8 petal, and (f) ℓ=± 6 resulting into 12 petals.

3.1 Detection of the helical modes

Different detection tools have been introduced to extract the azimuthal and radial components of these modes, from the use of dove prisms separating the odd and even azimuthal indices,[2] to the use of refractive optical elements that transforms the azimuthal varying beam into a linear phase variation resulting in spots of light at ℓ dependent positions.[15,16] Similarly to the generation of LG modes using the fork hologram in Fig. 1, when a LG mode of order ℓ is pass through a fork diffraction grating of order $-\ell$, the output mode results in a Gaussian signal in the Fourier plane of a lens as seen in Fig. 5, referred to as the azimuthal decomposition technique.[17] This technique can be used to detect any arbitrary field $u(r, \theta)$ by expanding the field into the angular harmonics, $\exp(i\ell\theta)$:

$$u(r, \theta) = \sum c_\ell(r) \exp(i\ell\theta), \tag{3}$$

where c_ℓ is the r dependent coefficient and ℓ is the azimuthal index. We implemented this detection tool in our experimental setup in Fig. 3, where we generated an ℓ varying beam in Fig. 5(a) on SLM1 and encoded SLM2 with a $-\ell$ hologram Fig. 5(b), to observe a Guassian signal Fig. 5(c) on the CCD camera.

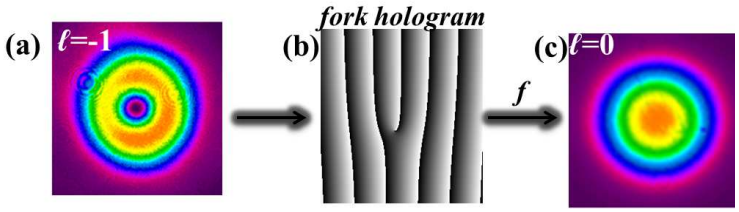

Figure 5. (a)LG mode of ℓ=-1 passing through (b) the azimuthal filter fork hologram with charge of ℓ=+1, (c) resulting in a Gaussian signal of charge ℓ=0.

There are detection limitations associated with these modes such as mode coupling. The contributing factor to this mode coupling is the spherical aberration of the Gaussian envelope which was corrected for, by generating a collimated flat wave front. The uneven power distribution of these modes since their sizes increase by a factor of ℓ, contributes to the uneven modal spectrum. To correct for the uneven power distribution we measured the power spectrum of these modes and normalised the power to the minimum modal power. The normalised

coefficients were incorporated in the encoded holograms which modulated the intensity of the modes to be equal as shown in Fig. 6.

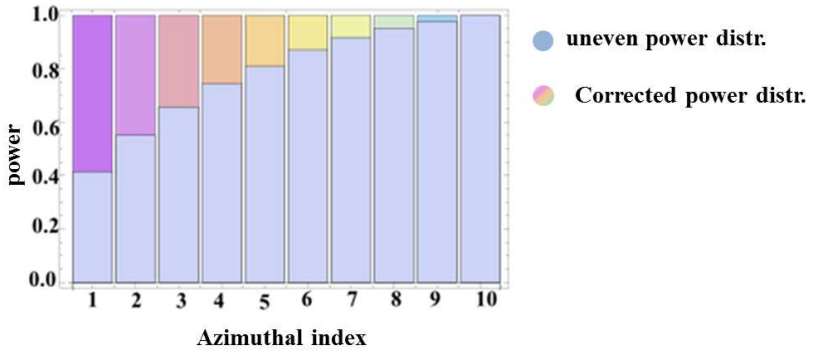

Figure 6. The uneven and corrected power spectrums.

Taking these factors into consideration we show that we can improve the mode coupling between the neighbouring ℓ modes in Fig. 7(a), to a pure spectrum of ℓ, ρ modes in Fig. 7(b), so that they become more efficient for optical communication.

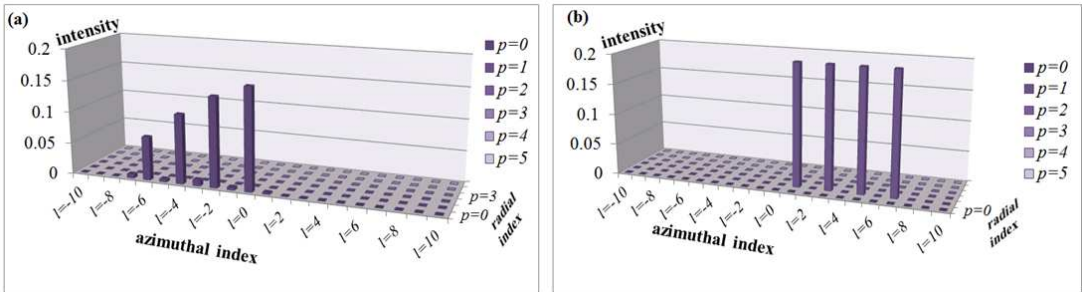

Figure 7. Azimuthal and radial spectrums of the multiplexed modes of (a)ρ=0, ℓ=1,3,5,7 without the power and wave front corrections and (b) ρ=1, ℓ=1,3,5,7 with the power and wave front corrections.

4. CONCLUSION

We have successfully multiplexed spatial modes of two degrees of freedom in free-space and have shown that by correcting the wave front and the uneven power distribution of the modes we can improve the mode coupling of multiplexed modes in free space. The next step will be to propagate these modes through a single mode fibre and incorporate different detection tools to improve our signal processing for optical communication applications.

REFERENCES

1. Richardson, D., Fini, J., and Nelson, L., "Space-division multiplexing in optical fibres," *Nature Photonics* **7**(5), 354–362 (2013).
2. Padgett, M. and Allen, L., "Light with a twist in its tail," *Contemporary Physics* **41**(5), 275–285 (2000).
3. Bouchal, Z. and Celechovskỳ, R., "Mixed vortex states of light as information carriers," *New Journal of Physics* **6**(1), 131 (2004).
4. Gibson, G., Courtial, J., Padgett, M., Vasnetsov, M., Pas' ko, V., Barnett, S., and Franke-Arnold, S., "Free-space information transfer using light beams carrying orbital angular momentum," *Optics Express* **12**(22), 5448–5456 (2004).

5. Bozinovic, N., Yue, Y., Ren, Y., Tur, M., Kristensen, P., Huang, H., Willner, A. E., and Ramachandran, S., "Terabit-scale orbital angular momentum mode division multiplexing in fibers," *Science* **340**(6140), 1545–1548 (2013).
6. Yao, A. M. and Padgett, M. J., "Orbital angular momentum: origins, behavior and applications," *Advances in Optics and Photonics* **3**(2), 161–204 (2011).
7. Schulze, C., Dudley, A., Flamm, D., Duparré, M., and Forbes, A., "Reconstruction of laser beam wavefronts based on mode analysis," *Applied Optics* **52**(21), 5312–5317 (2013).
8. McGloin, D. and Dholakia, K., "Bessel beams: diffraction in a new light," *Contemporary Physics* **46**(1), 15–28 (2005).
9. Gori, F., Guattari, G., and Padovani, C., "Bessel-gauss beams," *Optics Communications* **64**(6), 491–495 (1987).
10. Durnin, J., Miceli Jr, J., and Eberly, J., "Diffraction-free beams," *Physical Review Letters* **58**(15), 1499 (1987).
11. Vasilyeu, R., Dudley, A., Khilo, N., and Forbes, A., "Generating superpositions of higher–order bessel beams," *Optics Express* **17**(26), 23389–23395 (2009).
12. Arrizón, V., Ruiz, U., Carrada, R., and González, L. A., "Pixelated phase computer holograms for the accurate encoding of scalar complex fields," *JOSA A* **24**(11), 3500–3507 (2007).
13. McLaren, M., Agnew, M., Leach, J., Roux, F. S., Padgett, M. J., Boyd, R. W., and Forbes, A., "Entangled bessel-gaussian beams," *Optics Express* **20**(21), 23589–23597 (2012).
14. McLaren, M., Mhlanga, T., Padgett, M. J., Roux, F. S., and Forbes, A., "Self-healing of quantum entanglement after an obstruction," *Nature Communications* **5**(3248) (2014).
15. Lavery, M. P., Robertson, D. J., Berkhout, G. C., Love, G. D., Padgett, M. J., and Courtial, J., "Refractive elements for the measurement of the orbital angular momentum of a single photon," *Optics Express* **20**(3), 2110–2115 (2012).
16. Dudley, A., Lavery, M., Padgett, M., and Forbes, A., "Unraveling bessel beams," *Optics and Photonics News* **24**(6), 22–29 (2013).
17. Litvin, I. A., Dudley, A., Roux, F. S., and Forbes, A., "Azimuthal decomposition with digital holograms," *Optics Express* **20**(10), 10996–11004 (2012).